# Controls on the Flow Regime and Thermal Structure of the Subduction Zone Mantle Wedge: A Systematic 2-D and 3-D Investigation

**Ph.D. Thesis**

*by*

**Giuseppe Le Voci**
**CID: 00612509**

*supervised by*

**Dr. Rhodri Davies**
**Dr. Saskia Goes**
**Dr. Matthew Piggott**

Applied Modelling and Computation Group (AMCG)
Department of Earth Science and Engineering
Imperial College, London
October 2013

# Chapter 1

# Abstract

**Arc volcanism at subduction zones is likely regulated by the mantle wedge's flow regime and thermal structure and, hence, numerous studies have attempted to quantify the principal controls on mantle wedge conditions. In this thesis, we build on these previous studies by undertaking the first systematic 2-D and 3-D numerical investigations, across a wide parameter-space, into how hydration, thermal buoyancy and toroidal flow around the slab edge influence the wedge's flow regime and associated thermal structure. We find that small-scale convection (SSC), resulting from Rayleigh-Taylor instabilities, or drips, off the base of the overriding lithosphere, is a typical occurrence, if: (i) viscosities are $< 5 \times 10^{18}$ Pa s; and (ii) hydrous weakening of wedge rheology extends at least 100-150 km from the forearc corner. In 2-D models, instabilities generally take the form of 'drips'. In 3-D, two separate, but interacting, longitudinal Richter roll systems form (with their axes aligned perpendicular to the trench), the first below the arc region and the second below the back-arc region. These instabilities result in transient and spatial temperature fluctuations of 100-150K, which are sufficient to influence melting, the stability of hydrous minerals and the dehydration of crustal material. Furthermore, they are efficient at eroding the overriding lithosphere, particularly in 3-D and, thus, provide a means to explain observations of high heat flow and thin back-arc lithosphere at many subduction zones. A preliminary study into the effects of a finite-width slab on the wedge's flow regime, which allows for toroidal flow around the slab edge, highlights that the toroidal cell can locally increase or decrease temperatures sufficiently to either enhance or shut down wet melting, while a hydrated wedge corner may channel trench-parallel flow. The dynamic complexities of wedge flow revealed by our models may help explain the diversity in geophysical and geochemical subduction signatures.**

## COPYRIGHT DECLARATION

## STATEMENT OF ORIGINALITY

*I hereby certify that the work presented in this thesis is only and exclusively my own, or else appropriately referenced.*

# Contents

# Chapter 2

# Introduction

## 2.1 Motivation

Subduction zones are Earth's dominant tectonic features. They form the location of major underthrusting earthquakes, explosive arc volcanism and are the only sites of deep earthquakes within Earth's mantle (see Fig. 2.1). The role of subduction zones within Earth's plate tectonic framework is reasonably well understood [Davies, 1999]. Whilst mid-ocean ridges are generally considered passive features, generated via the pull-apart of surrounding oceanic lithosphere, subduction zones form the main driving force for plate tectonics, through the sinking of old and dense lithosphere [e.g. Forsyth and Uyeda, 1975]. The deformation is accommodated by bending of the oceanic lithosphere and by large underthrusting earthquakes in the seismogenic zone. From a long-term geological perspective, the earthquakes efficiently decouple the motion of the subducting slab from the overriding plate. Down-dip from the seismogenic zone, the slab is coupled to the overlying mantle and the viscous drag draws down the mantle along with the subducting slab. This flow, in turn, draws in mantle from below the overriding lithosphere. This zone of viscous deformation between the descending slab and the overriding plate defines the mantle wedge (see Fig. 2.2).

In addition to their dynamic and tectonic importance, subduction zones play a crucial role in Earth's chemical evolution. Upon subduction, the oceanic lithosphere encounters higher temperatures and pressures, causing dehydration of sediments, oceanic crust and the hydrated portions of the oceanic mantle, through a variety of metamorphic reactions. The flux of water into the overlying hot mantle wedge causes melting by lowering the solidus (melting temperature) of peridotite. Partial melting of subducted sediments and oceanic crust and pressure-

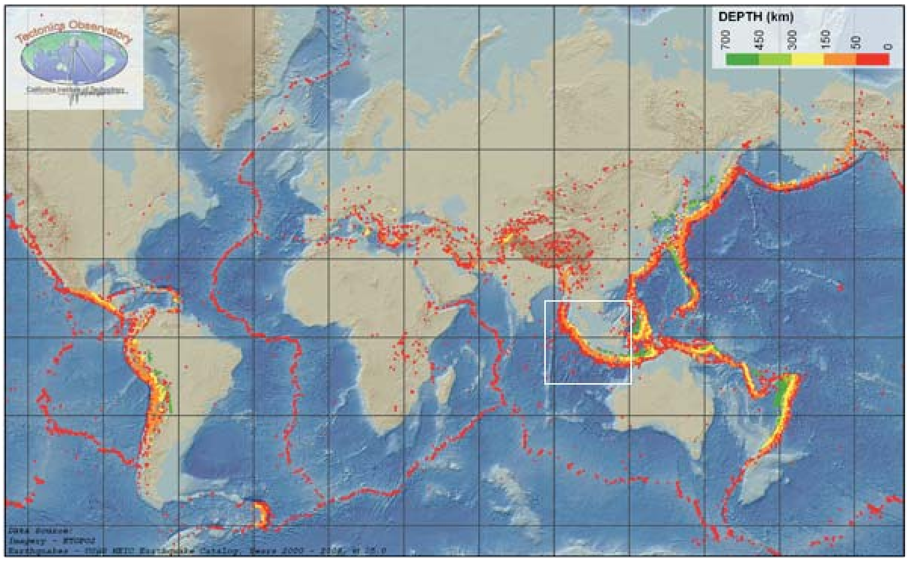

***Figure 2.1:*** *Global earthquake map. The colours indicate earthquake depth, with the deepest earthquakes delineating subduction zones, where one tectonic plate sinks below another into Earth's mantle, for example, the Java Trench, which is outlined by the white box (source: tectonics observatory at Caltech).*

release melting of the overlying mantle also contribute to magmatism, which is responsible for arc volcanism and for the modification and formation of continental crust.

Studies of the subduction zone mantle wedge require input from multiple disciplines, with complementary approaches required to constrain the likely flow regime and thermal structure. For example, the chemistry of arc magmas and the records of metamorphic events help constrain pressure-temperature-time paths. Observed seismic velocities, anisotropy and attenuation are linked to temperature and flow conditions in the slab and mantle wedge. Computational models, based on conservation principles, allow one to predict the temperature distribution under given assumptions about subduction geometry and physical conditions. The latter approach is utilised throughout this thesis, to gain both a qualitative and quantitative understanding of the dominant controls on the wedge's flow regime and thermal structure.

## 2.2 Previous Work

Numerical simulations of mantle wedge dynamics have predominantly explored 2-D systems, where wedge flow is driven by kinematic subduction of the down-going plate, under a dry rheology, and neglecting the effect of buoyancy. Under these conditions, a corner-flow regime dominates, where viscous drag from the subducting plate pulls hot mantle material deep into the wedge corner, subsequently carrying it to depth sub-parallel to its surface [e.g. Davies and Stevenson, 1992, Peacock, 1996, Peacock and Wang, 1999, van Keken et al., 2002, Kelemen et al.,

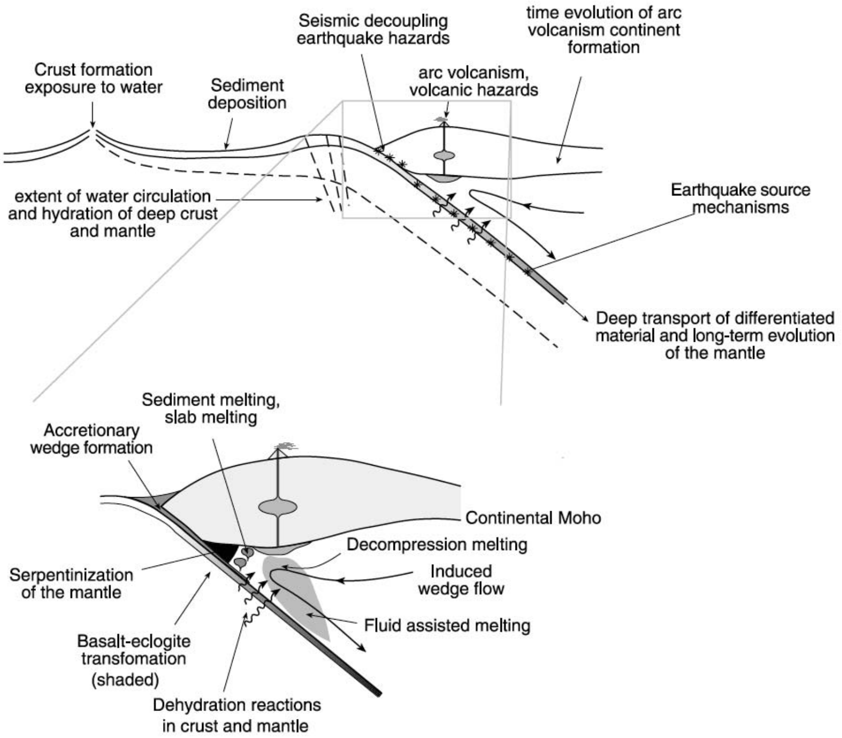

***Figure 2.2:*** *Illustration of the importance of the mantle wedge environment in the structure and dynamics of subduction zones. Water released from the subducting slab by metamorphic reactions aids in the generation of arc volcanism and earthquakes. The release and transport of water and melt to the volcanic front is sensitive to the thermal structure of the slab and wedge environment [from van Keken, 2003].*

2003]. Recent models which incorporate realistic non-Newtonian mantle rheologies that are simultaneously dependent on stress and temperature, are able to match numerous wedge observations, such as: (i) the downgoing plate thermal structure predicted by arc geochemistry [Plank et al., 2009]; (ii) surface topography [Hebert and Gurnis, 2010]; (iii) distributions of intermediate-depth Benioff seismicity [Abers et al., 2006]; and (iv) correlations between the locations of volcanic arcs and subduction parameters such as downgoing plate age and dip [e.g. England et al., 2004, England and Wilkins, 2004, Syracuse et al., 2010, Grove et al., 2012]. However, they are unable to explain others observations, such as temporal variability in arc volcanism [Honda and Yoshida, 2005], thin back-arc lithospheres [Currie and Hyndman, 2006], and corresponding local heat flow measurements [Schurr et al., 2003].

The flow field of previous plate-driven models is usually realized by prescribing relatively high viscosities (consistent with a dry mantle) and neglecting the effects of buoyancy (only kinematic effects of subducting plate buoyancy are applied), whilst they are often aided by the choice of boundary conditions. However, at least part of the wedge is likely damp (as is background mantle sampled below mid-ocean-ridges - Hirth and Kohlstedt [1996]), or wet (due to the introduction of fluids released from the downgoing plate). If the upper mantle rheology is damp or wet, upper mantle viscosities are likely to be low [e.g. Karato and Wu, 1993, Hirth and Kohlstedt, 1996] and, accordingly, buoyancy will become important in controlling wedge dynamics [e.g. Davies and Stevenson, 1992]. Indeed, regional studies indicate that wedge viscosities may be an order of magnitude lower than background mantle [Billen and Gurnis, 2001, Jadamec and Billen, 2010].

Models that have previously considered these effects produce small-scale convection (SSC), driven by Rayleigh-Taylor instabilities from the base of the overriding plate [e.g. Honda and Saito, 2003, Arcay et al., 2005, Currie et al., 2008, Wirth and Korenaga, 2012]. Such instabilities help to explain finger-like seismic velocity patterns below Japan [Tamura et al., 2002] and the aforementioned observations of thin lithospheric back-arcs with a high heat-flow [Currie et al., 2008]. They also lead to a transient thermal structure, which has been proposed to explain temporal variations in volcanic activity [Honda et al., 2010]. Considered together, these studies [and others, e.g. Gerya et al., 2006, Zhu et al., 2009] demonstrate that SSC could have a significant effect on wedge thermal structure and, hence, slab dehydration and melt conditions [e.g. Arcay et al., 2005, 2006, 2008]. However, thus far, a systematic study into the factors controlling SSC and its implications for the mantle wedge's flow regime and thermal structure has not been undertaken.

Our aims for this thesis are: (i) to perform a systematic investigation into the different possible modes of mantle wedge flow, under a range of subduction configurations and rheological parameters; and (ii) to determine their implications for mantle wedge thermal structure. We intentionally keep our set-up simple, with subducting plate motion and the coupling between downgoing and overriding plates prescribed kinematically. We also focus on end-member cases of uniform wedge hydration. Initially, we conduct 2-D analyses, with fully 3-D wedge flow (in models that exclude and include flow around slab edges) subsequently examined.

## 2.3 Thesis Outline

We use 2-D and 3-D numerical models, where a kinematically prescribed subducting slab drives dynamic flow in the surrounding mantle domain, to explore how hydration, buoyancy and toroidal flow (i.e. flow around the slab edge) influence the wedge's flow regime and associated thermal structure. Our models are generated using Fluidity, a state-of-the-art computational framework that was recently developed by the Applied Modelling and Computation

Group (AMCG), at Imperial College London. Although originally an ocean model [e.g. Piggott et al., 2008], Fluidity was extended and validated extensively for geodynamical applications by Davies et al. [2011] and Kramer et al. [2012]. The results presented in this thesis represent the first in depth application of Fluidity to geodynamical problems.

The structure of the thesis is as follows:

- In Chapter 3 we present an overview of Fluidity's underlying numerical methodologies. In addition, we further validate the code for kinematically driven subduction zone simulations like those presented herein, via comparisons with the well-established benchmark of van Keken et al. [2008].
- In Chapter 4, we present results from a systematic 2-D parameter space study, to establish the likely significance of hydration, buoyancy and upper plate instability for the wedge's flow regime and thermal structure. 2-D simulations, such as those presented, allow for a rapid understanding of parameter-space sensitivity, thus aiding with the configuration and interpretation of more complex 3-D models.
- In Chapter 5, results are presented from 3-D models, where the slab extends throughout the third-dimension of our computational domain. Although 3-D wedge flow models have been examined previously [e.g. Honda and Saito, 2003], a systematic study into the influence of hydration, buoyancy and subduction parameters (e.g. subduction velocity, upper plate age), has not yet been undertaken. We show that the third-dimension plays a critical role in dictating the wedge's flow regime and associated thermal structure.
- It is likely that the finite lateral extent of slabs plays a crucial role in the mantle wedge's flow regime and thermal structure. A number of seismic and geochemical observations are consistent with flow from the subslab region into the mantle wedge around slab edges [Pearce et al., 2001, Wendt et al., 1997, Trua et al., 2003, Smith et al., 2001, Civello and Margheriti, 2004], which likely produces trench-parallel relative temperature variations. In Chapter 6, we present *preliminary* results from 3-D simulations, into the morphology of wedge flow resulting from subduction of a finite-width slab. Our results imply that this component of flow, which has been neglected from previous models of the mantle wedge, plays an important role in wedge dynamics.

We note that each of our chapters contains a stand-alone introductory section, in addition to chapter specific conclusions. In addition, our major conclusions are summarised in Chapter 7, where we also provide potential directions for future research.

***Research contributions:*** All models were set up, run and analysed by Le Voci, with guidance from Davies, Goes and Piggott. Additional assistance on Fluidity development, where necessary, was provided by Stephan Kramer and Cian Wilson. Interpretations were a joint effort by Le Voci, Davies and Goes.

# Chapter 3

# Validating Fluidity against Benchmark Studies

## 3.1 Summary

**In this chapter we present our computational methods and evaluate how to optimise model resolution for the problem of wedge flow. The accuracy of Fluidity for simulations of mantle dynamics has previously been demonstrated via comparisons with a range of analytical and benchmark solutions [Davies et al., 2011, Kramer et al., 2012]. However, in this chapter, we validate Fluidity specifically for kinematically driven simulations of mantle wedge flow, under a range of rheological regimes, via comparisons with the well-established benchmark of van Keken et al. [2008]. The characteristics of the models we will be using in this thesis are very similar to those of this benchmark, making this a particularly powerful test.**

## 3.2 Benchmark Setup and Diagnostics

The benchmark geometry is the same for all cases: the domain is chosen to be 660-km wide and 600-km deep. It is filled with an incompressible Stokes fluid and split into three regions: (i) a $45°$-dipping slab, descending at 5cm/yr; (ii) a 50-km thick rigid (zero velocity) overriding plate; and (iii) the mantle wedge, where corner-flow is induced through viscous coupling with the slab (buoyancy forces are neglected).

The inflow boundaries and top of the model have prescribed temperature boundary conditions of 1573K and 273K, respectively. A linear temperature gradient is prescribed to the side of the overriding plate, whilst an error-function solution for half-space cooling is prescribed to the incoming plate, as follows:

$$T(x=0,y) = T_s + (T_0 - T_s)erf(\frac{y}{2\sqrt{\kappa t_{50}}}). \tag{3.1}$$

Here, the slab age $t_{50}$ is 50Myr, and $\kappa$ is thermal diffusivity. Mechanical boundary conditions for the wedge are no-slip below the overriding plate and constant velocity along the slab surface, with stress-free conditions at the wedge boundary.

We examine simulations at resolutions ranging from 500-metres to 5-km and calculate the same steady-state diagnostics as van Keken et al. [2008]. Let us define $T_{ij}$ as the matrix containing temperatures at points in the $i^{th}$ row and $j^{th}$ column of a rectangular grid with 6km spacing, superimposed on the mesh such that $T_{1,1}$ and $T_{111,101}$ are respectively at the top left and bottom right corners of the domain. Taking the analytical solution for 2D basally-driven corner-flow in Batchelor [1967] as initial or boundary condition for Stokes equations, the steady-state thermal fields obtained are analyzed and compared via three measures, as follows:

1. Temperature at a single, fixed point at the slab-wedge interface, at $(60, 60)$km.
2. Discrete $L2$ norm of temperature for $36$ points along the slab-wedge interface, in the $0-210$km depth range:
$$||T_{slab}|| = \sqrt{\frac{\sum_{i=1}^{36} T_{ii}^2}{36}}. \tag{3.2}$$
3. Discrete $L2$ norm of temperature for $78$ points in the wedge corner, placed on a triangular portion of the grid in the $54-120$km depth range:
$$||T_{wedge}|| = \sqrt{\frac{\sum_{i=10}^{21} \sum_{j=10}^{i} T_{ij}^2}{78}}. \tag{3.3}$$

The various other codes contributing to the benchmark study, while solving for the same diagnostics and using an identical set-up, employ distinct solution methods, and solve over domains with different mesh resolutions. Throughout this chapter, we predominantly compare against finite-element codes identified in the benchmark study with the acronyms: UM (Peter Van Keken's), PGC (Currie, He and Wang's) and VT (Scott King's). Results with UM are obtained for a grid with variable resolution, highest at boundary layers (100 m), down to a maximum element size of 10 km. The maximum element size for PGC is 20km. The PGC group encountered difficulties with the element aspect ratio at the wedge tip and built very small elements ($10^{-8}$ to 70 m) in a 1 km region close to the tip. VT used quadrilateral elements with 1 km minimum spacing near the tip. In order to compare against all these methods, we chose to use uniform element sizes, as mentioned above.

## 3.3 Test Case Descriptions

Following the numbering convention of van Keken et al. [2008], the test cases are split into two groups with varying model rheology: (i) isoviscous; (ii) creep. This section briefly describes the boundary conditions and rheological laws applied in each case.

### 3.3.1 Test Case 1(a) - Analytical Cornerflow Model

Velocities are prescribed via the analytical solution for corner-flow [Batchelor, 1967]. As such, this case tests our solution strategy for the energy equation.

### 3.3.2 Test Case 1(b) - Dynamical Flow in an Isoviscous Wedge: Dirichlet

Here, velocity and pressure are prognostic variables. However, Batchelor's solution is prescribed as Dirichlet boundary conditions at the wedge boundaries. Flow in the isoviscous wedge is therefore dynamically induced by the prescribed kinematic movement of the slab. The heat equation is solved throughout the domain.

### 3.3.3 Test Case 1(c) - Dynamical Flow in an Isoviscous Wedge: Neumann

This case is identical to 1(b), but stress-free (Neumann) boundary conditions are imposed at wedge inflow and outflow boundaries. Minimal differences are thus expected between Cases 1b and 1c.

### 3.3.4 Test Cases 2(a) and 2(b) - Dynamical Flow with Diffusion and Dislocation Creep

The final test cases are similar to 1(c), except that the mantle is no longer isoviscous. Cases 2(a) and 2(b) utilise Newtonian temperature dependent diffusion creep and non-Newtonian strain-rate dependent dislocation creep rheologies, respectively (thus most closely approximating the models presented herein). Olivine is assumed to be the dominant constituent of the upper mantle, so that the following simplified laws can be used to approximate diffusion creep:

$$\eta_{\text{diff}}(T) = A_{\text{diff}} \exp\Big(\frac{E_{\text{diff}}}{RT}\Big), \tag{3.4}$$

and dislocation creep:

$$\eta_{\text{disl}}(T, \bar{\bar{\dot{\varepsilon}}}) = A_{\text{disl}} \exp\Big(\frac{E_{\text{disl}}}{nRT}\Big)\bar{\bar{\dot{\varepsilon}}}^{\frac{(1-n)}{n}}, \tag{3.5}$$

where subscripts ‘diff’ and ‘disl’ indicate diffusion and dislocation creep, respectively [e.g. Karato and Wu, 1993]. $A_{\text{diff}}$ and $A_{\text{disl}}$ are pre-exponential constants, $E_{\text{diff}}$ and $E_{\text{disl}}$ are the activation energies needed to enter the respective regimes (see Table 3.1 for values used herein). The exponent $n$ in the power-law relationship between viscosity $\eta_{\text{disl}}$ and the second invariant of the strain rate tensor $\bar{\bar{\dot{\varepsilon}}}$ accounts for the effects of stress-dependence under dislocation creep.

To avoid obtaining high stresses analogous to creep regimes other than diffusion and dislocation (such as Peierls creep), modified viscosity laws are also introduced to truncate viscosity at a fixed maximum $\eta_{\text{max}}$ of $10^{26}$Pa, yielding effective diffusion and dislocation viscosities $\eta_{\text{diff,eff.}}$ and $\eta_{\text{disl,eff.}}$ as follows:

$$\eta_{\text{diff,eff.}} = \Big(\frac{1}{\eta_{\text{diff}}} + \frac{1}{\eta_{\text{max}}}\Big)^{-1}, \tag{3.6a}$$

$$\eta_{\text{disl,eff.}} = \Big(\frac{1}{\eta_{\text{disl}}} + \frac{1}{\eta_{\text{max}}}\Big)^{-1}. \tag{3.6b}$$

## 3.4 Solution Strategy

We solve the Stokes and energy equations, assuming an incompressible, Bousinessq formulation [McKenzie et al., 1974]. The solution strategy employed throughout this thesis is identical to that presented in Davies et al. [2011]. Nonetheless, for completeness, a brief summary is

| Quantity | Symbol | Reference value |
|---|---|---|
| Dynamic Viscosity | $\eta$ | $\eta_0 = 10^{21}$ Pa |
| Reference Density | $\rho$ | 3300 kg $\cdot$ m$^{-3}$ |
| Temperature | $T$ | $T_0 = 1573$ K= 1300 °C |
| Thermal conductivity | $k$ | 3 W$\cdot$ m$^{-1}\cdot$K$^{-1}$ |
| Heat capacity | $c_p$ | 1250 J$\cdot$ kg$^{-1}\cdot$K$^{-1}$ |
| Thermal diffusivity | $\overline{\overline{\kappa}}$ | $0.7272 \cdot 10^{-6}$ m$^2$s$^{-1}$ |
| Activation energy (diffusion creep) | $E_{diff}$ | 335 kJ$\cdot$ mol$^{-1}$ |
| Activation energy (dislocation creep) | $E_{disl}$ | 540 kJ$\cdot$mol$^{-1}$ |
| Power-law exponent (disl. creep) | $n$ | 3.5 |
| Pre-exponential constant (diff. creep) | $A_{diff}$ | $1.32043 \cdot 10^9$ Pa$\cdot$s |
| Pre-exponential constant (disl. creep) | $A_{disl}$ | $28968.6 \cdot 10^9$ Pa$\cdot$s$^{1/n}$ |
| Maximum viscosity | $\varepsilon_{max}$ | $10^{26}$ Pa$\cdot$ s |
| Universal gas constant | $R$ | 8.3145 J$\cdot$mol$^{-1}\cdot$K$^{-1}$ |

***Table 3.1:*** *Nomenclature and reference values for the benchmark models examined herein.*

prevented here.

### 3.4.1 Governing Equations

Fluidity solves the dimensional forms of *Stokes equations*:

$$\mu u_{i,jj} - p_{,i} + \Delta\rho g = 0, \tag{3.7a}$$

$$u_{i,i} = 0. \tag{3.7b}$$

where $\mu$ is dynamic viscosity, the $(\Delta\rho g)$ term is a "body force" which depends on density $\rho$ and gravitational acceleration $g$, and $u$ is velocity. Characteristic scales can then be defined for our problem, if the following non-dimensional relations are defined:

$$x_i = dx'_i, \tag{3.8}$$

$$u_i = \frac{\kappa}{d}u'_i, \tag{3.9}$$

$$T = \Delta T T' + T_0, \tag{3.10}$$

$$t = \frac{d^2}{\kappa}t', \tag{3.11}$$

$$P = \frac{\mu_0 \kappa}{d^2} P', \tag{3.12}$$

$$\mu = \mu_0 \mu', \tag{3.13}$$

where $d$ is domain length, $t$ is time, $\mu_0$ is a reference dynamic viscosity, $\kappa$ is thermal diffusivity and $\Delta T$ is the temperature difference across the domain when $T_0$ is taken as reference temperature. These expressions allow a formulation of the non-dimensional momentum and continuity equations in the form:

$$\sum_j \partial'_j \sigma'_{ij} + \mathrm{Ra}_0 T' \hat{k}_i = 0, \tag{3.14}$$

$$\sum_j \partial'_j u'_j = 0, \tag{3.15}$$

where $u_i$, $\sigma_{ij}$ and $T$ are respectively velocity, stress and temperature and $\hat{k}_i$ is the unit vector in the direction opposite to gravity. The dimensionless Rayleigh number $\mathrm{Ra}_0$ represents the vigor of convection:

$$\mathrm{Ra}_0 = \frac{\rho_0 \alpha \Delta T g d^3}{\mu_0 \kappa}, \tag{3.16}$$

where $\rho_0$ denotes reference density and $\alpha$ is the thermal expansion coefficient.

A consitutive relation relates the deviatoric stress tensor, $\tau_{ij}$ and the strain rate tensor, $\dot{\varepsilon}_{ij}$:

$$\tau_{ij} = 2\mu \dot{\varepsilon}_{ij} = \mu(\partial_j u_i + \partial_i u_j). \tag{3.17}$$

This allows us to use the decomposition of the full stress tensor, $\sigma_{ij}$, into deviatoric and volumetric components:

$$\sigma_{ij} = \tau_{ij} - p\delta_{ij}, \tag{3.18}$$

where $\tau_{ij}$ is the deviatoric stress tensor, $p$ is dynamic pressure and $\delta_{ij}$ is the Kronecker delta function, and substitute it, non-dimensionalised, into (3.14) to yield:

$$\sum_j \partial'_j \left[\mu'(\partial'_j u_i + \partial'_i u'_j)\right] - \partial'_i p' + \mathrm{Ra}_0 T' \hat{k}_i = 0. \tag{3.19}$$

The evolution of the thermal field is simulated via the following advection-diffusion equation (in dimensional form):

$$\frac{\partial T}{\partial t} + \sum_i u_i \partial_i T = \sum_i \partial_i (\kappa \partial_i T). \tag{3.20}$$

We solve for the unknowns pressure, $p$, and velocity, $u_i$, via (3.19), and temperature, $T$, via (3.20), given suitable initial and boundary conditions.

### 3.4.2 Discretized Momentum Equation

Solutions to (3.15) and (3.19) are obtained within Fluidity as approximations on unstructured meshes, via Galerkin finite-element discretization methods. Starting from the weak form of the equations, the continuity and momentum equations are tested with application of the following requirement:

$$\int \sum_{i,j} \left[(\partial_j N_i)\, \mu\, (\partial_j u_i + \partial_i u_j) + N_i \partial_i p\right] = \int \sum_i N_i \mathrm{Ra}_0 T \hat{k}_i, \tag{3.21}$$

$$\int \sum_j (\partial_j M)\, u_j = 0, \tag{3.22}$$

for imposed test functions $M$ and vector valued functions $N_i$. Note that we have integrated by parts the viscosity term in the momentum equation and the divergence term in the continuity equation, but left out the boundary terms:

$$\int_{\partial\Omega} \sum_{i,j} N_i \mu\, (\partial_j u_i + \partial_i u_j)\, n_j \tag{3.23}$$

$$\text{and} \quad \int_{\partial\Omega} \sum_j M u_j n_j, \tag{3.24}$$

respectively, dealt with in combination with the boundary conditions. Here, $n_j$ is the outward pointing normal to the boundary $\partial\Omega$. For no-slip boundary conditions all velocity components, $u_i$, are strongly enforced to be zero, which eliminates both (3.23) and (3.24). For combined free-slip and no-normal flow conditions, only (3.24) disappears, but the tangential velocity components are left free in both test and trial space, and the integral disappears following substitution of the no-normal stress condition, $\sum_j n_j \sigma_{ij} = 0$, in (3.23).

The solution fields, $u_i$ and $p$, are subsequently restricted to a finite-dimensional trial space featuring polynomial functions within each element, constructed via mesh generation and subdivision into a set of polygonal elements. In this study we utilize a P2-P1 discretization with piecewise quadratic functions (P2) for velocity and piecewise linear functions (P1) for pressure. Let the P1 basis $M_a$, where $a$ is the index of the associated vertex, and the P2 basis $N_b$, where $b$ ranges over all quadratic nodes in an element. Discrete solutions to $u_i$ and $p$ are then respectively given by the following linear combinations of $N_b$ and $M_a$:

$$u_i = \sum_b u_{b_i} N_b \quad \text{and} \quad p = \sum_a p_a M_a, \tag{3.25}$$

where $u_{b_i}$ and $p_a$ represent values of these functions at the associated nodes. Using $N_b$ and $M_a$ as test functions, and $u_{b_i}$ and $p_a$ as trial functions, (3.21) and (3.22) become a linear system where $\underline{u}$ and $\underline{p}$ are vectors of the coefficients $u_{b_i}$ and $p_a$:

$$\begin{pmatrix} \mathrm{K} & \mathrm{G} \\ \mathrm{G}^T & 0 \end{pmatrix} \begin{pmatrix} \underline{u} \\ \underline{p} \end{pmatrix} = \begin{pmatrix} \underline{f} \\ 0 \end{pmatrix}, \tag{3.26}$$

The matrices K and G and right hand side vector $\underline{f}$ are given by:

$$\begin{aligned} \mathrm{K}_{b_i c_j} &= \int (\partial_j N_b)\, \mu\, (\partial_i N_c) + \sum_k (\partial_k N_b)\, \mu\, (\partial_k N_c)\, \delta_{ij}, \\ \mathrm{G}_{a b_j} &= \int (\partial_j M_a)\, N_b, \\ \underline{f}_{b_i} &= \int N_b \mathrm{Ra}_0 T \hat{k}_i. \end{aligned}$$

Fluidity solves this indefinite system of equations using a full-projection/pressure-correction approach, equivalent to the Schur Complement Method in May and Moresi [2008]. Under the assumption that we know the state of all variables at the $nth$ timestep and that we wish to calculate their value at the $(n+1)th$ step, the algorithm reads:

1. Given an initial pressure field $p_0$ (we use the pressure from the previous timestep or iteration), solve for a preliminary velocity $\underline{\boldsymbol{u}}_*$ in:

$$\mathrm{K}\underline{\boldsymbol{u}}_* + G\underline{p}_0 = \underline{f}. \tag{3.27}$$

2. The pressure correction $\underline{\tilde{p}}^{n+1} = \underline{p}_0 + \Delta\underline{p}$, which projects back the resulting velocity to a divergence free solution, is then obtained from:

$$\mathrm{G}^T\mathrm{K}^{-1}\mathrm{G}\Delta\underline{p} = \mathrm{G}^T\underline{\boldsymbol{u}}_*. \tag{3.28}$$

3. Velocity correction is then performed:

$$\underline{\tilde{\boldsymbol{u}}}^{n+1} = \underline{\boldsymbol{u}}_* - \mathrm{K}^{-1}\mathrm{G}\Delta\underline{p}. \tag{3.29}$$

The resulting $\underline{\tilde{\boldsymbol{u}}}^{n+1}$ and $\underline{\tilde{p}}^{n+1}$ are then solutions of (3.26). In Fluidity, these equations are solved via preconditioned Krylov subspace (non-stationary) iterative methods ([e.g. Elman et al., 2005, May and Moresi, 2008]), utilizing the Portable Extensible Toolkit for Scientific Computation (PETSc) library [Balay et al., 1997]. (3.27) and (3.29) are evaluated within a linear system with symmetric positive definite matrix $\mathrm{K}$, using the Conjugate Gradient (CG) method with an algebraic multigrid (AMG) preconditioner [Vanek et al., 1996]. Fluidity implements its own version of this algorithm, as detailed in Kramer et al. [2010].

The pressure correction equation (3.28) is solved using the FGMRES Krylov method [Saad, 1993], preconditioned with a pressure mass matrix, scaled by the local inverse of viscosity [Verfurth, 1984, Benzi et al., 2005, May and Moresi, 2008]. In solving (3.28), we adopt a matrix-free representation of $\mathrm{G}^T\mathrm{K}^{-1}\mathrm{G}$, as an explicit construction of this *Schur-complement* matrix would be expensive due to the presence of $\mathrm{K}^{-1}$. This requires one additional *inner solve* of $\mathrm{K}$, for every iteration of the FGMRES method, for which we again use CG preconditioned with AMG.

### 3.4.3 Discretized Advection-Diffusion Equation

The Galerkin-discretized advection-diffusion equation (3.20) is a matrix equation:

$$\mathrm{M}\frac{\mathrm{d}\underline{T}}{\mathrm{d}t} + \mathrm{A}(u_i)\underline{T} + \mathrm{D}\underline{T} = 0, \tag{3.30}$$

where $\mathrm{M}$, $\mathrm{A}$ and $\mathrm{D}$ are the mass, advection and diffusion matrices, respectively, given by:

$$\mathrm{M}_{ab} = \int N_a N_b, \tag{3.31}$$

$$\mathrm{A}(u_i)_{ab} = \int \sum_i N_a u_i \partial_i N_b, \tag{3.32}$$

$$\mathrm{D}_{ab} = \int \sum_i \left(\partial_i N_a\right) \kappa \left(\partial_i N_b\right), \tag{3.33}$$

$\underline{T}$ is a vector of coefficients $T_a$, such that $T = \sum_a T_a N_a$. A control-volume method detailed in Wilson [2009] is used to solve this system. Strong and weak imposition of Dirichlet and Neumann ($\sum_j n_j \partial_j T = 0$) boundary conditions, respectively, justify the absence of additional boundary terms in $\mathrm{A}$ and $\mathrm{D}$.

Temporal discretization is achieved via a classic $\theta$ scheme:

$$\mathrm{M}\frac{\underline{\tilde{c}}^{n+1} - \underline{c}^{n}}{\Delta t} + \mathrm{A}(\boldsymbol{u}_i^{n+\theta_{\mathrm{nl}}})\underline{T}^{n+\theta_c} + \mathrm{D}\underline{T}^{n+\theta_c} = 0, \tag{3.34}$$

where:

$$\underline{T}^{n+\theta_c} = \theta_c \underline{\tilde{c}}^{n+1} + (1-\theta_c)\underline{c}^{n}, \quad 0 \leqslant \theta_c \leqslant 1. \tag{3.35}$$

Equation (3.34) depends on the solution of (3.26) for the advective velocity, whilst the resulting temperature feeds back into (3.26) via the buoyancy term and sometimes viscosity. A Picard iteration deals with the non-linear coupling between these equations, using in turn the latest available values for the non-linear terms. Let $\tilde{u}_i^{n+1}$ the velocity field obtained in the previous solution of (3.26). The advective velocity solution of (3.34) is then given by:

$$\boldsymbol{u}_i^{n+\theta_{\mathrm{nl}}} = \theta_{\mathrm{nl}} \tilde{u}_i^{n+1} + (1-\theta_{\mathrm{nl}}) u_i^{n}, \quad 0 \leqslant \theta_{nl} \leqslant 1. \tag{3.36}$$

Using equation (3.35), (3.34) can be rearranged into a single matrix equation:

$$\left[M + \theta_c \Delta t \left(\mathrm{A}(\boldsymbol{u}_i^{n+\theta_{\mathrm{nl}}}) + \mathrm{D}\right)\right] \underline{\tilde{c}}^{n+1} = \left[M - (1-\theta_c)\Delta t \left(\mathrm{A}(\boldsymbol{u}_i^{n+\theta_{\mathrm{nl}}}) + \mathrm{D}\right)\right] \underline{c}^{n}, \tag{3.37}$$

where the unknown vector is now $\underline{\tilde{c}}^{n+1}$. A Generalized-Minimum-Residual (GMRES) Krylov subspace method is used to solve this system [Saad, 1993], with Successive-Over-Relaxation (SOR) preconditioning. A Crank-Nicholson scheme is used in the timestepping algorithm, (i.e., $\theta_{\mathrm{nl}} = \theta_c = 0.5$).

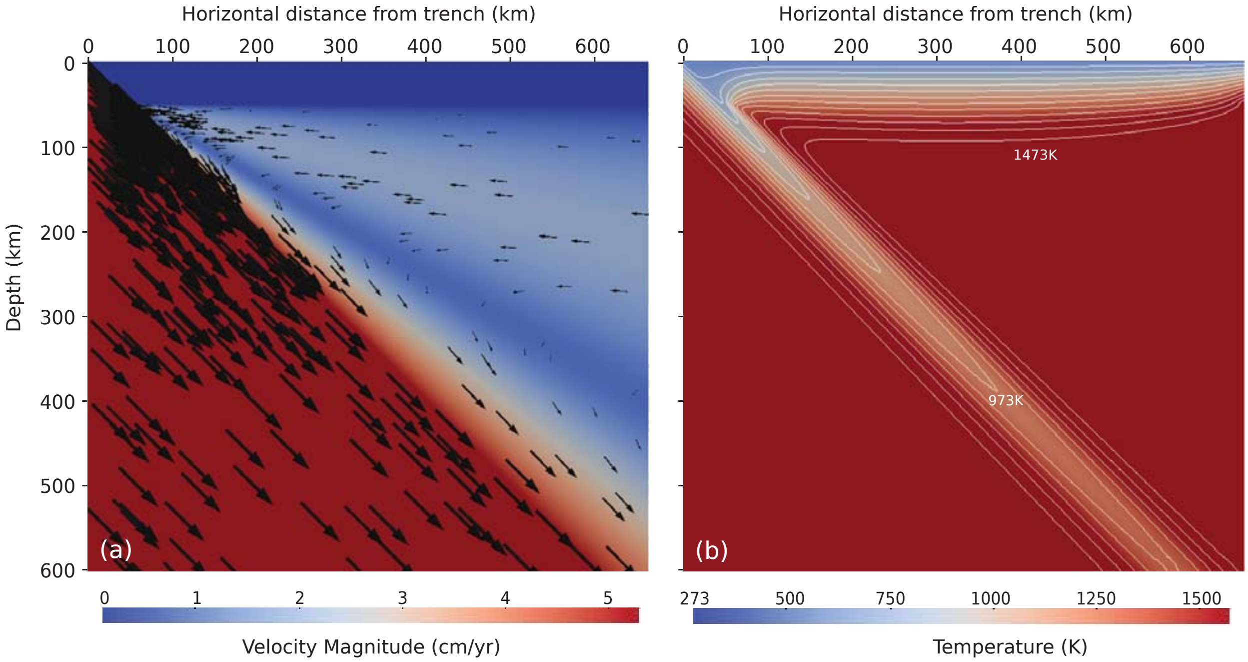

***Figure 3.1:*** *Analytically prescribed cornerflow velocity* $(a)$ *and prognostic temperature contours* $(b)$ *for the isoviscous benchmark case* $1(a)$*. The velocity vectors point in the direction of flow and scale in length with velocity. Temperature contours spacing is 100K.*

## 3.5 Benchmark Results

### 3.5.1 Test Cases 1(a), 1(b) and 1(c): Velocity and Temperature

Isoviscous models predict a velocity field solution that closely approximates the Batchelor solution in the wedge, as expected (Fig. 3.1). The thermal field obtained has contours that lie sub-parallel to overriding and downgoing plates, with relatively smooth temperature gradients in comparison to the solutions obtained under diffusion and dislocation creep regimes (following section) .

Steady-state temperatures closely approximate the benchmark solutions (Table 3.2). Fig. 3.2 shows convergence towards the benchmark values for all isoviscous cases.

| Case | Code | $T_{60,60}$ | $\|\|T_{slab}\|\|$ | $\|\|T_{wedge}\|\|$ |
|---|---|---|---|---|
| 1(a) | ***Fluidity*** | **390.26** | **504.91** | **854.82** |
| | Brown | 393.51 | 520.14 | 866.52 |
| | LDEO | 396.63 | 506.43 | 855.58 |
| | NTU | 388.87 | 507.43 | 852.99 |
| | *PGC* | 388.21 | 503.69 | 854.34 |
| | *UM* | 388.24 | 503.77 | 852.89 |
| | *VT* | 379.87 | 502.26 | 852.05 |
| | *WHOI* | 388.26 | 503.75 | 854.37 |
| 1(b) | ***Fluidity*** | **385.10** | **502.50** | **853.42** |
| | Brown | 391.83 | 493.76 | 842.01 |
| | LDEO | 387.15 | 500.86 | 852.80 |
| | NTU | 391.42 | 511.27 | 853.16 |
| | *PGC* | 388.21 | 503.69 | 854.34 |
| | *UM* | 388.22 | 503.65 | 854.12 |
| | *VT* | 389.82 | 504.63 | 853.04 |
| | *WHOI* | 389.08 | 504.50 | 856.08 |
| 1(c) | ***Fluidity*** | **384.61** | **501.23** | **850.47** |
| | LDEO | 397.55 | 505.70 | 850.50 |
| | NTU | 391.57 | 511.09 | 852.43 |
| | *PGC* | 387.78 | 503.10 | 852.97 |
| | *UM* | 387.84 | 503.13 | 852.92 |
| | *VT* | 389.39 | 503.04 | 851.68 |
| | *WHOI* | 388.73 | 504.03 | 854.99 |

***Table 3.2:*** *Selected steady-state thermal quantities (in °C) for the highest resolution isoviscous simulations. Fluidity results for a mesh with* $500m$ *minimum element size at the wedge corner, and* $10km$ *lowest background resolution are in bold. Italic entries indicate finite element codes; please refer to van Keken et al. [2008] for a detailed explanation of the solution methods applied in these models.*

### 3.5.2 Test Case 1(b) : Pressure

The sharp transition from subduction velocity prescribed in the slab, to null velocity in the stationary overriding plate, causes a well known pressure singularity at the tip of the wedge corner, which creates numerical difficulties in the solution of the Stokes system. The consequent oscillations in the pressure solution dissipate quickly across a few elements when resolution at the wedge corner is high [e.g. Currie et al., 2004, Davies et al., 2008]. To test pressure predictions, absolute values and gradients of pressure are calculated for two distinct points close to the wedge corner ($P_1$) and in the center of the wedge ($P_2$) and compared to the analytical corner-flow solution formulated by Batchelor [1967]. The location of the reference node where an absolute value for pressure is defined, was not defined in the benchmark pressure. It was here arbitrarily set to zero at the bottom-right corner of the domain, yielding Fluidity's best-match to the analytical solution for pressure. Pressure gradients are extremely accurate throughout the mantle wedge (Table 3.3).

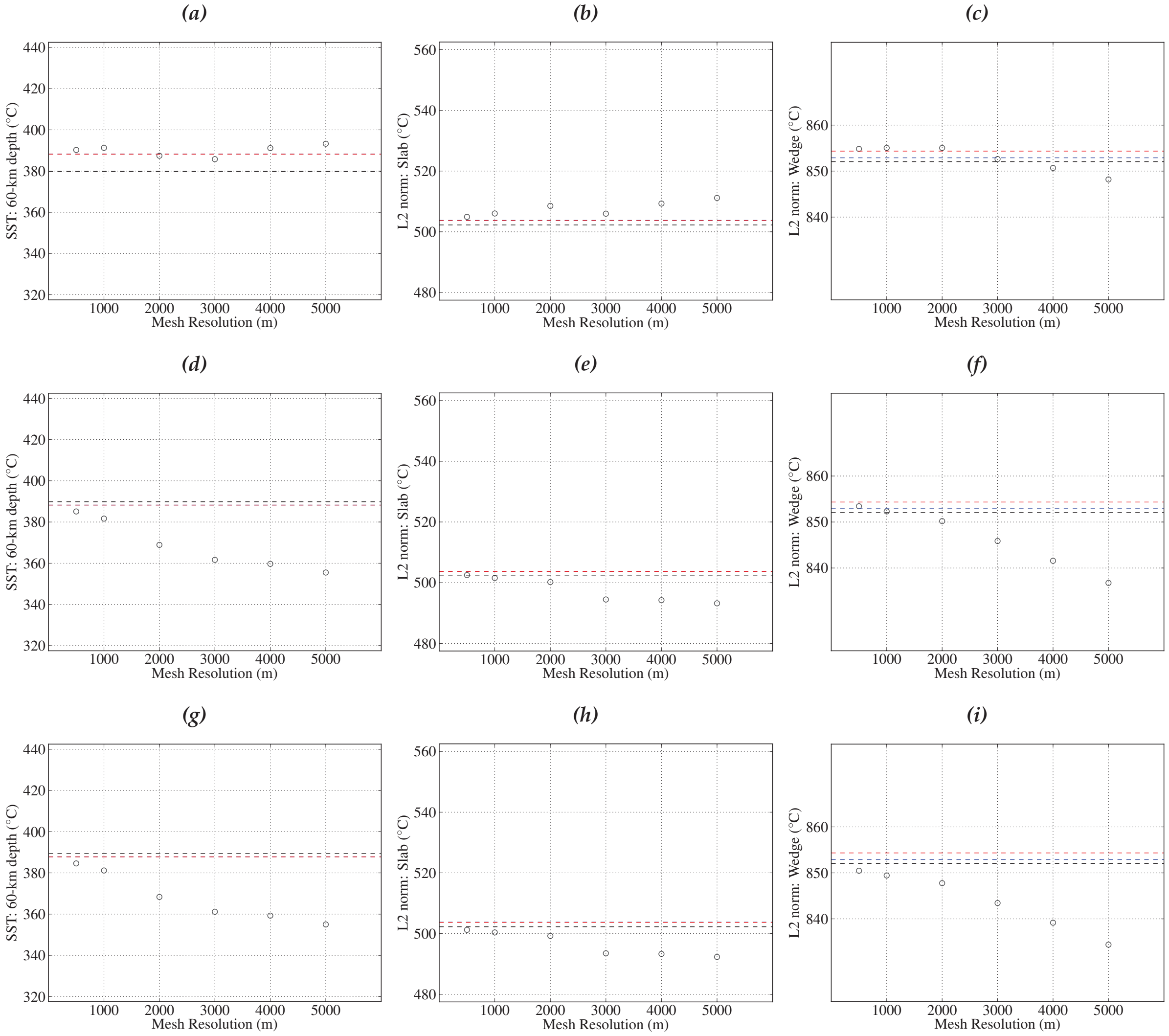

***Figure 3.2:*** *Fluidity's predictions (black circles) of various diagnostics from the benchmark study of van Keken et al. [2008]. Dashed horizontal lines denote the highest resolution predictions of three representative codes from the benchmark study: (i) UM (blue); (ii) VT (black); and (iii) PGC (red). Fluidity's results are presented for models where Batchelor's analytical corner-flow solution for mantle wedge velocity is (a–c) prescribed everywhere, (d–f) prognostic following Dirichlet boundary conditions and (g–i) prognostic following stress-free (Neumann) boundary conditions, at a range of minimum element sizes (denoted by the horizontal scale). Mantle rheology is here isoviscous.*

| **Code** | $P_1$ | $P_2$ | $P_{x,1}$ | $P_{y,1}$ | $P_{x,2}$ | $P_{y,2}$ |
|---|---|---|---|---|---|---|
| Analytical | -929.46 | -7.34 | 55.97 | 12.71 | 0.02935 | 0.02748 |
| ***Fluidity*** | **-929.715** | **-7.3506** | **56.150** | **12.493** | **0.02955** | **0.02745** |
| ***Relative Error*** | **-**$0.0274\%$ | **-**$0.1444\%$ | **-**$0.3216\%$ | **+**$1.7073\%$ | **+**$0.6814\%$ | **+**$0.1092\%$ |
| LDEO | -916 | -7.3 | 54.5 | 11.9 | 0.0293 | 0.0275 |
| NTU | -911.9 | 2.2 | 55.63 | 16.02 | 0.02935 | 0.02751 |
| *PGC* | -929.53 | -7.35 | 51.16 | 11.45 | 0.03047 | 0.02758 |
| *UM* | -930.51 | -7.70 | 56.24 | 12.51 | 0.0294 | 0.0275 |
| *VT* | -927.8 | -7.11 | - | - | - | - |
| *WHOI* | -930 | -7.35 | 56.86 | 14.45 | 0.0293 | 0.0277 |

***Table 3.3:*** *For case $1(b)$, pressure (in MPa) and pressure gradients (in MPa/km) for points $P_1$ and $P_2$ at coordinates $(66, 54)$km and $(594, 354)$km are listed for each code; Fluidity results for a mesh with $100$m minimum element size in the corner and $10$km lowest background resolution are in bold; italic indicates finite element codes.*

### 3.5.3 Test Cases 2(a) and 2(b)

Fluidity's results, once again, are in excellent agreement with the benchmark solutions, for simulations under diffusion and dislocation creep regimes (Table 3.4). The positive feedback between temperature and creep viscosity focusses the corner-flow towards the tip of the wedge, curving downwards the wedge isotherms directly under the overriding plate. This strengthens the thermal gradients at the slab-wedge interface. Under dislocation creep, comparable thinning of the thermal boundary layers is achieved, but temperatures reached at the wedge corner are marginally lower (Figs. 3.3 and 3.4).

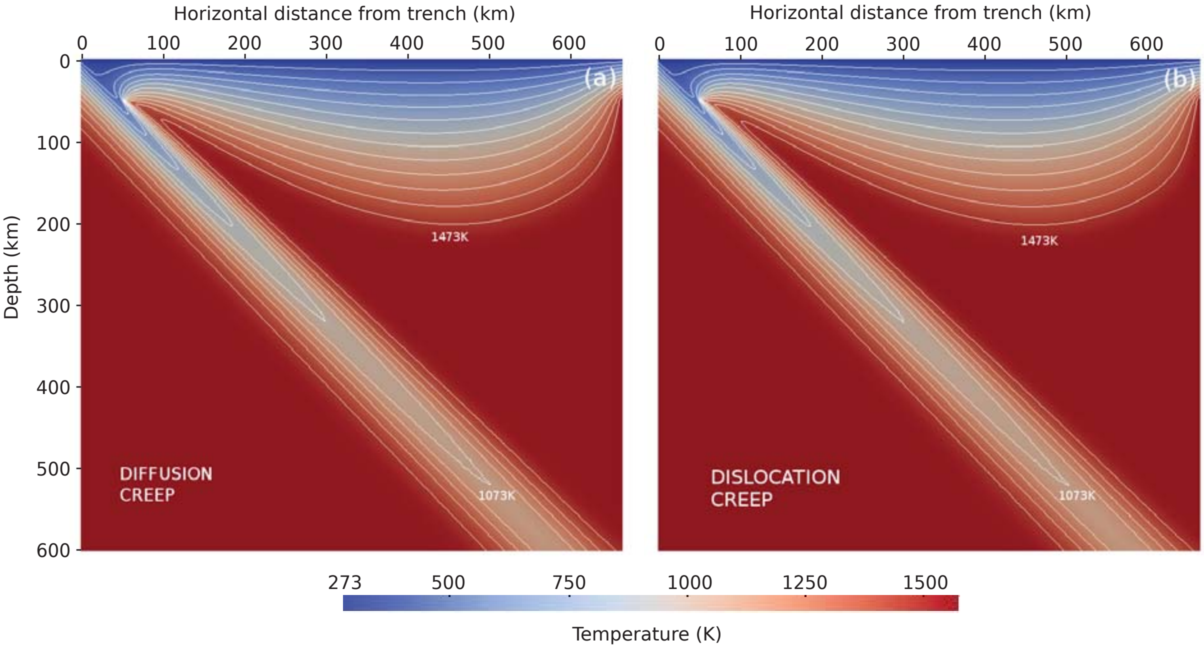

***Figure 3.3:*** *Steady-state temperature (white contours every 100K) for the simulations with diffusion and dislocation creep rheologies in the wedge. Dislocation creep yields slightly higher temperatures close to the wedge corner.*

| Case | Code | $T_{60,60}$ | $\|\|T_{slab}\|\|$ | $\|\|T_{wedge}\|\|$ |
|---|---|---|---|---|
| 2(a) | ***Fluidity*** | **576.68** | **605.81** | **1002.66** |
| | NTU | 570.30 | 614.09 | 1007.31 |
| | *PGC* | 580.52 | 606.94 | 1002.85 |
| | *UM* | 580.66 | 607.11 | 1003.20 |
| | *VT* | 577.59 | 607.52 | 1002.15 |
| | *WHOI* | 581.30 | 607.26 | 1003.35 |
| 2(b) | ***Fluidity*** | **580.67** | **603.86** | **998.68** |
| | LDEO | 550.17 | 593.48 | 994.11 |
| | NTU | 551.60 | 608.85 | 984.08 |
| | *PGC* | 582.65 | 604.51 | 998.71 |
| | *UM* | 583.36 | 605.11 | 1000.01 |
| | *VT* | 574.84 | 603.80 | 995.24 |
| | *WHOI* | 583.11 | 604.96 | 1000.05 |

***Table 3.4:*** *Selected steady-state thermal quantities (in °C) for the highest resolution variable viscosity simulations. Fluidity results for a mesh with* $100m$ *minimum element size at the trench and wedge corner, and* $10km$ *lowest background resolution, are shown in bold. Italic entries indicate finite element codes.*

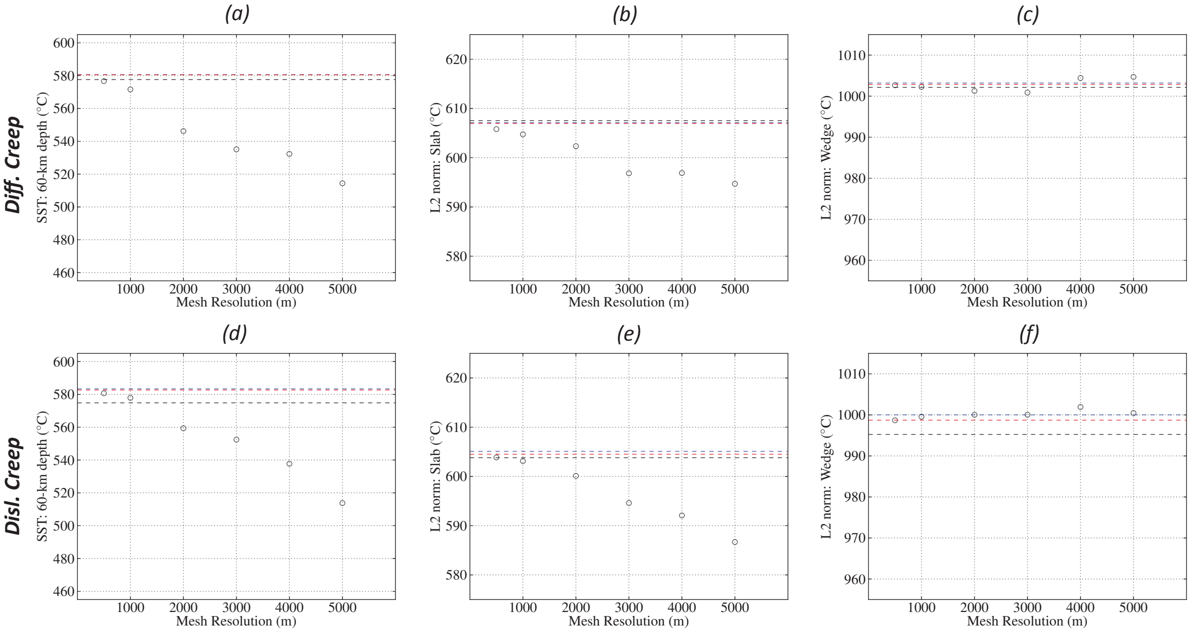

***Figure 3.4:*** *Fluidity's predictions (black circles) of various diagnostics from the benchmark study of van Keken et al. [2008]. Dashed horizontal lines denote the highest resolution predictions of three representative codes from the benchmark study: (i) UM (blue); (ii) VT (black); and (iii) PGC (red). Fluidity's results are presented for diffusion (a–c) and dislocation (d–f) creep rheologies, at a range of grid resolutions.*

## 3.6 Conclusions

We have demonstrated that Fluidity is an excellent tool for studying mantle wedge flow because of its flexibility in setting up grids with highly variable resolution. In particular, mantle wedge temperature benchmarks reported by finite element codes (UM, VT and PGC) in van Keken et al. [2008] are most closely in agreement to those within Fluidity for diagnostics obtained under the creep conditions likely dominant for wedge rheology. Fluidity offers further flexibility to expand wedge models to fully dynamic scenarios, where the slab responds to flow in the wedge and around it, but for the systematic investigations of this thesis we will use a kinematic set-up that closely resembles this benchmark.

# Chapter 4

# A Systematic 2-D Investigation into the Mantle Wedge's Transient Flow Regime and Thermal Structure: Complexities arising from a Hydrated Rheology and Thermal Buoyancy.

## 4.1 Summary

**Arc volcanism at subduction zones is likely regulated by fluid abundance in the mantle wedge. Most previous studies focussed on slab-driven flow under a dry rheology, neglecting the role of buoyancy. Some showed that the effects of variable hydration and buoyancy in a wetter wedge, for ridge source-like mantle composition, can be strong. This study explores how these factors impact the variability of flow styles in the mantle wedge, and the associated effects on the thermal structure. Finite-element numerical simulations of wedge flow above a kinematically driven subducting plate allow a systematic 2-D parameter space search for a range of plausible subduction velocities ($v_{subd} = 2-10$cm yr$^{-1}$), upper plate ages ($T_{upper} = 50-120$Myr) and water contents ($C_{OH} = 0-5000$H/$10^6$Si). Under the effect of buoyancy, the development of small-scale convection is a typical occurrence. Lithospheric drips have more time to develop and impact wedge thermal structure most when plate–driven corner flow velocities are low. High velocities and high viscosities result in the strongest upper-plate erosion above the wedge corner (limited by the prescribed depth of coupling). By constrast, back–arc upper plate erosion by SSC is not affected by subduction velocity, but**

**is determined by wedge viscosity, which needs to be less than $5 \cdot 10^{18} Pa \cdot s$, and the length of the plate available for destabilisation, which needs to exceed instability wavelengths. Thus the 2–D models indicate that thermal buoyancy significantly affects wedge dynamics and thereby dehydration and melting conditions and upper–plate evolution if hydrous weakening of wedge rheology extends at least 100 km or more from the trench.**

## 4.2 Introduction

Subduction zones are host to the largest earthquakes and most violent volcanic eruptions recorded on Earth. The magmatic processes occurring in these regions play a fundamental role in Earth's long-term thermo-chemical evolution, including the formation and growth of continental crust [e.g. McCulloch and Bennett, 1994, Hawkesworth et al., 2010]. The mantle wedge, which is bounded by the downgoing and overriding plates, plays an important role in the integrated subduction system, controlling the partitioning of fluids into the deep mantle and towards the upper plate, where they control arc volcanism [e.g. Tatsumi, 1989, Manning, 2004]. It is likely that the mantle wedge also plays a crucial role in the dynamics of subduction, influencing the extent of coupling between the downgoing plate and the overlying mantle [e.g. Billen and Gurnis, 2001, Manea and Gurnis, 2007]. An improved understanding of the subduction zone mantle wedge is therefore of fundamental importance. Of particular interest is the wedge's flow field and associated thermal structure, which govern: (i) the buoyancy and rheology that control the large-scale dynamics of the mantle wedge and subducting plate; (ii) the generation of arc volcanism; and (iii) the cycling of volatiles and minerals between mantle, lithosphere, hydrosphere and atmosphere. Numerical models provide the key to an improved understanding of these processes.

Dynamic models of mantle wedge flow, driven solely by a kinematically prescribed subducting plate, are becoming increasingly realistic, incorporating plausible physical properties (e.g. a stress and temperature dependent rheology) and matching regional subduction characteristics [e.g. Syracuse et al., 2010]. Under such a framework, a corner flow regime is generated, where viscous drag from the downgoing plate pulls hot mantle material from below the overriding plate into the mantle wedge corner and, subsequently, downwards parallel to the subducting slab [e.g. Davies and Stevenson, 1992, Peacock, 1996, Peacock and Wang, 1999, van Keken et al., 2002, Kelemen et al., 2003]. Conductive thickening of the overriding plate facilitates strong focussing of flow into the mantle wedge corner, which leads to erosion (or 'pinching') of the overriding plate and elevated heat-flow beneath the fore-arc region [van Keken et al., 2002, van Keken, 2003]. This is inconsistent with local observations of low heat-flow and low seismic attenuation (high Q) [e.g. Furukawa and Uyeda, 1989, Kincaid and Sacks, 1997, Currie and Hyndman, 2006]. To circumvent this effect, recent models regulate the viscous coupling between downgoing plate and mantle wedge, with reduced coupling generally prescribed from the surface to a depth of 80 km [e.g. Conder, 2005, Wada and Wang, 2009, Syracuse et al., 2010]. Fully dynamic models, where the subducting slab evolves self-consistently, are likely required for this coupling to evolve naturally [e.g. Gerya and Yuen, 2003, Arcay et al., 2007].

With such a treatment of plate coupling, plate-driven mantle-wedge models match a wide-range of subduction zone observations that are sensitive to wedge temperatures, such as seismic anisotropy [Kneller et al., 2007, Long and Becker, 2010] and surface topography [Hebert and Gurnis, 2010]. They also agree with measurements pertaining to the thermal structure of the downgoing plate [Plank et al., 2009], the distribution of intermediate-depth Benioff seismicity [Abers et al., 2006] and a correlation of slab parameters, such as subduction velocity and dip angle, with the location of the volcanic-arc [e.g. England et al., 2004, England and Wilkins, 2004, Syracuse et al., 2010, Grove et al., 2012]. As a consequence, such models are now used in deriving volatile budgets for global subduction [e.g. Hacker and Abers, 2004, van Keken et al., 2011].

However, other observations, in particular those of a thin lithosphere and high heat-flow beneath many back-arc regions [e.g. Andrews and Sleep, 1974, Currie and Hyndman, 2006], indicate that wedge flow may be more complex than is implied by these previous studies. The flow field of previous plate-driven models is usually realized by prescribing relatively high viscosities (consistent with a dry mantle) and neglecting the effects of buoyancy (only kinematic effects of subducting plate buoyancy are applied), whilst they are often aided by the choice of boundary conditions. However, at least part of the wedge is likely damp (as is background mantle sampled below mid-ocean-ridges - Hirth and Kohlstedt [1996]), or wet (due to the introduction of fluids released from the downgoing plate). The production of hydrous melt will extract water from the wedge, thus drying it out where melt is formed [e.g. Hebert et al., 2009]. However, the efficiency of dehydration by melt extraction is unclear, as seismic imaging of back-arc mantle reveals extensive low-velocity and high-attenuation anomalies which are easiest explained with high water concentrations [e.g. Currie and Hyndman, 2006, Wiens et al., 2008, Hwang et al., 2011]. If the upper mantle rheology is damp or wet, upper mantle viscosities are likely to be low [e.g. Karato and Wu, 1993, Hirth and Kohlstedt, 1996] and, accordingly, buoyancy will become important in controlling wedge dynamics [e.g. Davies and Stevenson, 1992]. Indeed, regional studies indicate that wedge viscosities may be an order of magnitude lower than background mantle [Billen and Gurnis, 2001, Jadamec and Billen, 2010].

Models that have previously considered these effects produce small-scale-convection (SSC), driven by Rayleigh-Taylor instabilities from the base of the overriding plate [e.g. Honda and Saito, 2003, Arcay et al., 2005, Currie et al., 2008, Wirth and Korenaga, 2012]. Such instabilities help to explain finger-like seismic velocity patterns below Japan [Tamura et al., 2002], and the aforementioned observations of thin lithospheric back-arcs with a high heat-flow [Currie et al., 2008]. They also lead to a transient thermal structure, which has been proposed to explain temporal variations in volcanic activity [Honda et al., 2010]. Previous studies have been region specific, or involved feedback between a number of processes in the wedge [Arcay et al., 2005, Gerya et al., 2006, Zhu et al., 2009]. Such models highlight that SSC significantly affects dehydration and melt conditions [Arcay et al., 2005, 2006, 2008]. To better understand how different factors contribute to wedge dynamics, it is useful to analyse a set of models in between the kinematic models that have been successful in explaining a range of observations, and the dynamic models that illustrate how feedbacks between dehydration, rheology and dynamics yield a wide range of behaviour.

Our aims for this study are: (i) to perform a systematic investigation into the different possible modes of mantle wedge flow, under a range of subduction configurations and rheological parameters; and (ii) to determine their implications for mantle wedge thermal structure. We intentionally keep our set-up simple, with subducting plate motion and the coupling between downgoing and overriding plates prescribed kinematically. We also focus on end-member cases of uniform wedge hydration. In this chapter, we conduct 2-D analyses, with fully 3-D wedge flow examined thereafter in the next chapters. We note that a systematic analysis of SSC in 2-D complements a recent study by Wirth and Korenaga [2012], who used a 3-D single-mode approximation to examine SSC within the mantle wedge. Although SSC patterns will vary in 3-D [Richter, 1973, van Hunen et al., 2003, Wirth and Korenaga, 2012], the 2-D models examined herein allow for a wide parameter-space sensitivity study, and both a qualitative and quantitative understanding of the dominant controlling mechanisms, which will aid in interpreting any 3-D results. our 3-D models demonstrate that the 2-D simulations are a good representation of the average characteristics of the 3-D system and, as such, the results presented herein provide insights into the magnitude of temperature variations associated with SSC and, accordingly, the likely importance of SSC for slab dehydration and melting.

## 4.3 2-D Model Setup

We follow a standard 'kinematic' modelling approach, in which prescribed slab velocities drive fully-dynamic flow in the mantle wedge, beneath an overriding plate. We solve the Stokes and energy equations, assuming an incompressible, Bousinessq formulation, using Fluidity, a recently developed finite-element, control-volume code [Davies et al., 2011, Kramer et al., 2012]. The solution strategy employed for the Stokes equations is identical to that presented in [Davies et al., 2011], whilst a control-volume method is utilised to solve the energy equation. The accuracy of Fluidity for simulations of this nature has previously been demonstrated via comparisons with a range of analytical and benchmark solutions [Davies et al., 2011, Kramer et al., 2012]. In addition, Chapter 3 already documented Fluidity's ability to accurately simulate kinematically driven subduction, via comparisons with the well-established benchmark of van Keken et al. [2008].

### 4.3.1 Geometry, Boundary & Initial Conditions

Our model setup is illustrated in Fig. 4.1. The subducting plate travels horizontally at the surface for 50 km prior to subduction. It then follows a down-dipping circular arc, to a depth of 75 km, below which it subducts at a constant dip angle. The domain extends to a depth of 400 km, with domain length scaling with slab dip, taking values of 490 km, 700 km and 1110 km, respectively, for 70°, 50° and 30° dip cases. Subducting plate velocities are prescribed parallel to the slab surface. A resolution of 1 km is used close to the wedge corner, although resolution increases away from this corner, approaching 8-km at the domain's base. Such high-resolution is necessary to capture the fine-scale dynamics arising in these complex systems and, additionally, to limit the influence of the well-known pressure 'singularity' in the mantle wedge corner [e.g. Davies et al., 2008, van Keken et al., 2008]. Sensitivity tests revealed that the same wedge dynamics were found as long as minimum element sizes were less than 2 km at the wedge corner.

By limiting the depth of our domain to 400 km, the deeper slab's influence on the flow regime is not simulated. However, we account for the deeper slab's role by: (i) prescribing a basal wedge outflow boundary condition, equal to the subduction velocity; and (ii) positioning the lower right hand corner of the domain at a location that approximates the region of influence of the slab, inferred from deeper models. Unlike the majority of previous studies, our overriding plate is not fully fixed or rigid: it is free to evolve self-consistently in response to the

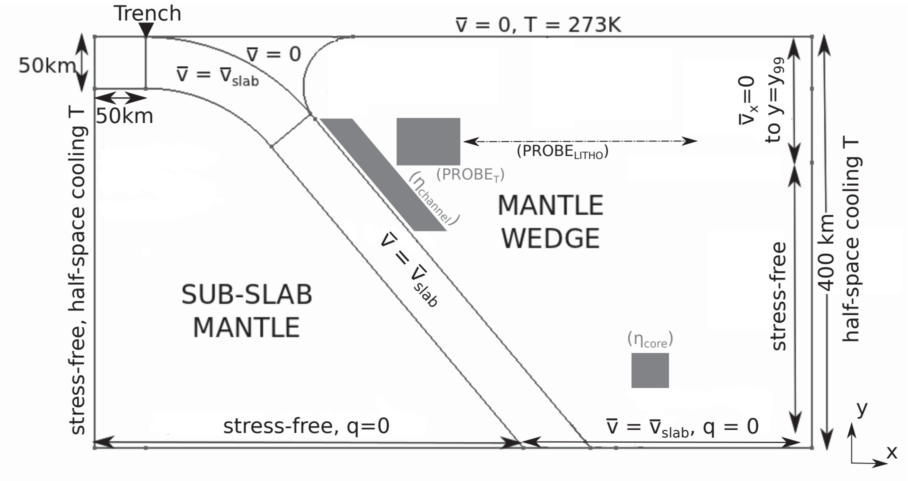

***Figure 4.1:*** *Model set-up: the domain is 400 km deep and either 490 km, 700 km or 1110 km wide, for* $70^\circ$, $50^\circ$ *and* $30^\circ$ *dip cases, respectively. It is divided into 4 regions: (i) a prescribed downgoing plate, where* $V = V_{slab}$*; (ii) a prescribed rigid forearc corner, where* $V = 0$*; (iii) a prognostic mantle wedge; and (iv) a prognostic sub-slab mantle. Temperature is calculated throughout the computational domain. The subducting slab curves to a constant dip angle at 75 km depth, and is fully coupled to wedge flow below 80 km depth. Temperature boundary conditions follow a half-space cooling relationship everywhere, except at the model's surface (prescribed to 273K) and base, where a zero heat flux boundary condition,* $q = \frac{dT}{dn} = 0$*, is enforced. Mechanical boundary conditions are stress-free everywhere except along the top of the overriding plate (fixed), at the base of the wedge (equal to slab velocity, in order to account for the drag which the slab would exert at greater depths) and on the side of the overriding plate, to the depth* $y_{99}$*, where temperatures equal 99% of the mantle temperature (in order to compensate for the absence of lithospheric thickening at the boundary). The 50 km*$^2$ *grey square (marked* $\eta_{core}$*, centered at 275 km depth and a horizontal distance of 50 km from the slab tip) and parallelogram (a 5–15 km thick strip, 10 km above the slab surface, between 80 and 130 km depth, marked* $\eta_{channel}$*) represent areas where wedge and channel viscosities are analysed (Section 4.5.1). Temperature transients in Figs. 4.8 and 4.11 are evaluated over the area marked by the* $40 \times 20$ *km grey rectangle (labelled* $PROBE_T$*), centered at 100 km depth, at a horizontal distance of* $75 \cdot tan(dip)$ *km from the wedge corner. The average depth of the 1400K isotherm, which is used as a proxy for lithospheric thickness in Section 4.4.4, is measured along the horizontal length spanned by the black dotted double-pointed arrow (labelled* $PROBE_{LITHO}$*), at a horizontal distance of 100–350 km from the wedge corner.*

local thermal structure and flow-field [e.g. Kelemen et al., 2003], aside from: (i) at its surface, where we impose a no-slip boundary condition; and (ii) in a curved triangle-shaped region above the subducting plate, where velocities are fixed to zero to a depth of 80-km. Below this depth, however, the subducting slab and mantle wedge are fully coupled, in a manner consistent with the *D80* model of Syracuse et al. [2010]. As noted previously, such a setup yields the so-called 'cold nose', which is consistent with observational constraints [e.g. Kincaid and Sacks, 1997, Rychert et al., 2008]. In selected models, where we examine the influence of a step in lithospheric thickness on the underlying flow field (caused, for example, by a strong craton), the length of the 'free' overriding plate is reduced by 200-km and replaced by a 200-km thick square, with a viscosity of $10^{24}$ Pa s, in the upper right-hand corner of the domain.

The surface temperature, $T_s$, is fixed to 273K. Side boundary conditions for temperature follow an error-function:

$$T(x=0,y) = T_s + (T_0 - T_s)erf(\frac{y}{2\sqrt{\kappa t_{plate}}}). \tag{4.1}$$

Here $T_0$ is the reference mantle temperature (fixed at 1623K), $t_{\text{plate}}$ is either the subducting slab age, $t_{\text{subd}}$, or the overriding plate age, $t_{\text{upper}}$, and $\kappa$ is thermal diffusivity. Eq. 5.1 is utilised in defining initial conditions, with $t_{\text{plate}} = t_{\text{subd}}$ imposed within the subducting plate and $t_{\text{plate}} = t_{\text{upper}}$ imposed in the mantle wedge, for all cases. We note that the fixed-temperature boundary condition on the right hand side of the domain does not account for lithospheric conductive cooling and thickening of the overriding plate over time. To minimise this boundary effect, we enforce a no normal-flow boundary condition down to a depth where temperature reaches a nominal value of 99% of mantle temperature.

Models are initialised until the thermal signature of the downgoing plate is advected to the base of the domain. In our results, we refer to the time when the slab reaches 400-km depth as $t = 0$. After a further $\approx 10$ Myr, wedge flow patterns stabilize into a single mode, although they do evolve further as the overriding plate thickens conductively. Accordingly, we analyse our results in the $t = 10 - 100$ Myr time window.

### 4.3.2 Material Properties

Material properties are summarised in Table 4.1. Standard values are used for equation of state parameters, and these do not vary spatially. For viscosity, a composite diffusion and dislocation creep rheology is utilised. Olivine is assumed to be the dominant constituent of the upper mantle, so that the following laws can be used when conditions are dry:

$$\begin{aligned} \eta_{\text{diff,d}}(T) &= A \exp\Big(\frac{E_{\text{diff,d}} + (PV_{\text{diff,d}})}{RT}\Big), && (4.2) \\ \eta_{\text{disl,d}}(T, \bar{\bar{\dot{\varepsilon}}}) &= B \exp\Big(\frac{E_{\text{disl,d}} + (PV_{\text{disl,d}})}{nRT}\Big)\bar{\bar{\dot{\varepsilon}}}^{\frac{(1-n)}{n}} && (4.3) \end{aligned}$$

whilst the following apply when hydration is introduced (i.e. for a damp, wet or very wet mantle):

$$\eta_{\text{diff,h}}(T) \;=\; D\,C_{\text{OH}}\exp\Big(\frac{E_{\text{diff,h}}+(PV_{\text{diff,h}})}{RT}\Big), \tag{4.4}$$

$$\eta_{\text{disl,h}}(T,\bar{\bar{\dot{\varepsilon}}}) \;=\; F\,(C_{\text{OH}}^{-r})^{\frac{1}{n}}\exp\Big(\frac{E_{\text{disl,h}}+(PV_{\text{disl,h}})}{nRT}\Big)\bar{\bar{\dot{\varepsilon}}}^{\frac{(1-n)}{n}}. \tag{4.5}$$

Here, $T$ and $P$ denote modelled temperature and reference pressure ($P = \rho_0 gh$, where $h$ denotes depth), respectively, whilst subscripts diff, disl, d and h denote diffusion creep, dislocation creep, and dry and hydrated mantle conditions ($C_{\text{OH}}$ and $r$ represent the water content and water content exponent, respectively [Hirth and Kohlstedt, 2003]). The exponent $n$ in the power-law relationship between viscosity, $\eta_{\text{disl}}$, and the second-invariant of the strain-rate tensor, $\bar{\bar{\dot{\varepsilon}}}$, accounts for the effects of stress dependence under dislocation creep; $R$ is the universal gas constant. The activation energies ($E_{\text{diff}}$, $E_{\text{disl}}$) and volumes ($V_{\text{diff}}$ and $V_{\text{disl}}$) used herein, from Hirth and Kohlstedt [2003], are listed in Table 4.1. Note that: (i) hydrated parameters are used here for all cases, excluding the dry cases; (ii) when calculating viscosities, an adiabatic gradient of 0.5 K/km is added to our Boussinesq potential temperature solution. We do not include a stress-limiting rheology, but, instead, truncate viscosity at a fixed maximum $\eta_{\text{max}}$ of $10^{24}$Pa, yielding effective diffusion and dislocation viscosities $\eta_{\text{diff,eff.}}$ and $\eta_{\text{disl,eff.}}$ as follows:

$$\eta_{\text{diff,eff.}} \;=\; \Big(\frac{1}{\eta_{\text{diff}}}+\frac{1}{\eta_{\text{max}}}\Big)^{-1} \tag{4.6a}$$

$$\eta_{\text{disl,eff.}} \;=\; \Big(\frac{1}{\eta_{\text{disl}}}+\frac{1}{\eta_{\text{max}}}\Big)^{-1} \tag{4.6b}$$

Diffusion and dislocation creep laws are, in turn, combined via a harmonic mean, to obtain a composite creep viscosity:

$$\eta_{\text{comp}} = \Big(\frac{1}{\eta_{\text{diff,eff.}}}+\frac{1}{\eta_{\text{disl,eff.}}}\Big)^{-1}. \tag{4.7}$$

| **Quantity** | **Symbol** | **Reference value** |
|---|---|---|
| Gravity | $g$ | $9.81 m \cdot s^{-2}$ |
| Reference Density | $\rho_0$ | $3300 kg \cdot m^{-3}$ |
| Mantle Temperature | $T$ | $T_0 = 1623K = 1350°C$ |
| Surface Temperature | $T_s$ | $T_s = 273K = 0°C$ |
| Thermal conductivity | $k$ | $3.1 W \cdot m^{-1} \cdot K^{-1}$ |
| Specific heat capacity (constant pressure) | $c_p$ | $1250 J \cdot kg^{-1} \cdot K^{-1}$ |
| Thermal diffusivity | $\overline{\overline{\kappa}}$ | $0.75 \cdot 10^{-6}$ $\mathrm{m^2 s^{-1}}$ |
| Thermal expansivity | $\alpha$ | $2.5 \cdot 10^{-4} K^{-1}$ |
| Activation energy - dry diff. creep | $E_{\text{diff,d}}$ | $375 kJ \cdot mol^{-1}$ |
| Activation energy - dry disl. creep | $E_{\text{disl,d}}$ | $530 kJ \cdot mol^{-1}$ |
| Activation energy - hyd. diff. creep | $E_{\text{diff,h}}$ | $335 kJ \cdot mol^{-1}$ |
| Activation energy - hyd. disl. creep | $E_{\text{disl,h}}$ | $480 kJ \cdot mol^{-1}$ |
| Activation volume - dry diff. creep | $V_{\text{diff,d}}$ | $6 \cdot 10^{-6}\ kJ \cdot mol^{-1}$ |
| Activation volume - dry disl. creep | $V_{\text{disl,d}}$ | $20 \cdot 10^{-6}\ kJ \cdot mol^{-1}$ |
| Activation volume - hyd. diff. creep | $V_{\text{diff,h}}$ | $4 \cdot 10^{-5}\ m^3 \cdot mol^{-1}$ |
| Activation volume - hyd. disl. creep | $V_{\text{disl,h}}$ | $11 \cdot 10^{-5}\ m^3 \cdot mol^{-1}$ |
| Power-law exponent | $n$ | $3.5$ |
| Maximum viscosity | $\eta_{\text{max}}$ | $10^{24} Pa \cdot s$ |
| Reference grain size | $g_0$ | $10 mm$ |
| Universal gas constant | $R$ | $8.3145 J \cdot mol^{-1} \cdot K^{-1}$ |
| Water Content - damp mantle | $C_{\text{OH},\text{damp}}$ | $1000\ \mathrm{H}/10^6\mathrm{Si}$ |
| Water Content - wet mantle | $C_{\text{OH},\text{wet}}$ | $3000\ \mathrm{H}/10^6\mathrm{Si}$ |
| Water Content - very-wet mantle | $C_{\text{OH},\text{v.wet}}$ | $5000\ \mathrm{H}/10^6\mathrm{Si}$ |
| Water content exponent | $r$ | $1.2$ |
| Pre-exponential constant - dry diff. creep | $A$ | $10^{8.82} Pa \cdot s$ |
| Pre-exponential constant - dry disl. creep | $B$ | $10^{\frac{-11.04}{n}} Pa \cdot s^{\frac{1}{n}}$ |
| Pre-exponential constant - hydrated diff. creep | $D$ | $10^{12} Pa \cdot s \frac{H}{10^6 Si}^{\frac{r}{n}}$ |
| Pre-exponential constant - hydrated disl. creep | $F$ | $10^{(6+\frac{1.95}{n})} Pa \cdot s^{\frac{1}{n}} \cdot \frac{H}{10^6 Si}^{\frac{r}{n}}$ |

***Table 4.1:*** *Nomenclature and reference values for 2-D model parameters used in this chapter.*

### 4.3.3 Model Cases

To unravel the dominant controls on the mantle wedge's flow-regime and thermal structure, we examine a suite of simulations, where we systematically vary a range of subduction parameters. To examine the role of viscosity, we vary wedge hydration between dry, 'damp' ($C_{\text{OH}} = 1000$ H/$10^6$Si – representative of sub-ridge mantle [Hirth and Kohlstedt, 1996]), wet ($C_{\text{OH}} = 3000$ H/$10^6$Si) and very-wet ($C_{\text{OH}} = 5000$ H/$10^6$Si) - as end-member subduction-zone hydration cases [e.g. Karato, 2003, Katz et al., 2003]. In all but a few cases, hydration is assumed to be constant throughout the wedge.

Most present-day downgoing plates subduct at dips ranging from 30° (e.g. Colombia, Chile), to 50° (Aleutians, Ryukyu, Tonga-Kermadec) and 70° (Hebrides, Izu-Bonin) [Lallemand et al., 2005, Syracuse and Abers, 2006, e.g.]. We choose to model subduction dynamics at such slab dips, so that model results are comparable to the majority of real subduction zones, with the exception of outliers such as Alaska (very flat subduction) or the Marianas (almost vertical subduction). Subduction velocity is also varied over a representative range of present-day descent rates, as slow (2 cm yr$^{-1}$, e.g. Nankai), intermediate (5 cm yr$^{-1}$, e.g. Aleutians, Scotia) and fast (10 cm yr$^{-1}$, e.g. New Britain, Solomon) subducting slabs are modelled [e.g. Lallemand et al., 2005, Syracuse and Abers, 2006, Seton et al., 2012]. For the overriding plate, we consider relatively young (50 Myr) and old (120 Myr) cases. The age of the downgoing plate is set to 50 Myr at the trench, on the low side of the average of current subducting plate ages, which range between ca. 10 Myr in Mexico and South Chile, to ca. 150 Myr in the Marianas and Izu-Bonin. However, we find that downgoing plate age has little effect on wedge conditions (Section 4.5.3)

The remainder of this chapter is structured as follows: in Section 4.4, we illustrate the different flow regimes that arise as a consequence of the aforementioned variations, in addition to how we distinguish between them. In Section 4.5, we examine how these parameters control the flow style, and we also explore several variations, which are not listed above: (i) an older subducting plate, where we increase $t_{\text{subd}}$ to 100 Myr at the trench; (ii) imposing a strong lithospheric block in the top-right-hand corner of the model; and (iii) excess hydration in a target region of the wedge corner. In Section 4.6, we discuss the impacts of the different flow regimes on wedge thermal structure, with conclusions and avenues for future work are discussed in Section 4.7.

| **Dip** (°) | **v$_{slab}$** (cm yr$^{-1}$) | **T$_{upper}$** (Myr) | **C$_{OH}$** ( H/10$^6$Si) | $\eta_{wedge}$ (Pa s) | $\eta_{channel}$ (Pa s) | **Stability** | **t$_{drips}$** (Myr) |
|---|---|---|---|---|---|---|---|
| 30 | 5 | 50 | 0 | $2.7 \cdot 10^{20}$ | $3.4 \cdot 10^{19}$ | *Corner flow* | n/a |
| 30 | 5 | 50 | 1000 | $1.1 \cdot 10^{19}$ | $3.4 \cdot 10^{18}$ | *Corner flow*, weak decoupling | n/a |
| 30 | 5 | 50 | 3000 | $4.5 \cdot 10^{18}$ | $2.2 \cdot 10^{18}$ | SSC-drips, weak decoupling | 7 |
| 30 | 5 | 50 | 5000 | $2.9 \cdot 10^{18}$ | $1.8 \cdot 10^{18}$ | SSC-drips, strong decoupling | 5 |
| 50 | 2 | 50 | 0 | $4.6 \cdot 10^{20}$ | $1.0 \cdot 10^{20}$ | *Corner flow* | n/a |
| 50 | 2 | 50 | 1000 | $1.2 \cdot 10^{19}$ | $7.1 \cdot 10^{18}$ | *Corner flow*, weak decoupling | n/a |
| 50 | 2 | 50 | 3000 | $5.4 \cdot 10^{18}$ | $4.1 \cdot 10^{18}$ | SSC-drips, strong decoupling | 4.8 |
| 50 | 2 | 50 | 5000 | $3.4 \cdot 10^{18}$ | $2.5 \cdot 10^{18}$ | SSC-drips, strong decoupling | 3.0 |
| 50 | 5 | 50 | 0 | $2.9 \cdot 10^{20}$ | $3.3 \cdot 10^{19}$ | *Corner flow* | n/a |
| 50 | 5 | 50 | 1000 | $1.0 \cdot 10^{19}$ | $3.3 \cdot 10^{18}$ | *Corner flow*, weak decoupling | n/a |
| 50 | 5 | 50 | 3000 | $3.7 \cdot 10^{18}$ | $1.6 \cdot 10^{18}$ | SSC-drips, weak decoupling | 9.0 |
| 50 | 5 | 50 | 5000 | $2.7 \cdot 10^{18}$ | $1.2 \cdot 10^{18}$ | SSC-drips, strong decoupling | 5.4 |
| 50 | 10 | 50 | 0 | $1.9 \cdot 10^{20}$ | $1.7 \cdot 10^{19}$ | *Corner flow* | n/a |
| 50 | 10 | 50 | 1000 | $7.9 \cdot 10^{18}$ | $2.4 \cdot 10^{18}$ | *Corner flow* | n/a |
| 50 | 10 | 50 | 3000 | $3.4 \cdot 10^{18}$ | $1.1 \cdot 10^{18}$ | SSC-drips | ca.30 |
| 50 | 10 | 50 | 5000 | $2.1 \cdot 10^{18}$ | $7.7 \cdot 10^{17}$ | SSC-drips, strong decoupling | 9.1 |
| 50 | 2 | 120 | 0 | $4.0 \cdot 10^{20}$ | $1.3 \cdot 10^{20}$ | *Corner flow* | n/a |
| 50 | 2 | 120 | 1000 | $1.2 \cdot 10^{19}$ | $8.2 \cdot 10^{18}$ | SSC-ripples, weak decoupling | ca.18.5 |
| 50 | 2 | 120 | 3000 | $4.9 \cdot 10^{18}$ | $3.9 \cdot 10^{18}$ | SSC-drips, strong decoupling | 7.9 |
| 50 | 2 | 120 | 5000 | $3.0 \cdot 10^{18}$ | $2.5 \cdot 10^{18}$ | SSC-drips, strong decoupling | 6.5 |
| 50 | 5 | 120 | 0 | $2.4 \cdot 10^{20}$ | $4.2 \cdot 10^{19}$ | *Corner flow* | n/a |
| 50 | 5 | 120 | 1000 | $1.0 \cdot 10^{19}$ | $3.9 \cdot 10^{18}$ | SSC-edge | 12.6 |
| 50 | 5 | 120 | 3000 | $3.9 \cdot 10^{18}$ | $1.9 \cdot 10^{18}$ | SSC-drips, weak decoupling | ca.10.2 |
| 50 | 5 | 120 | 5000 | $2.4 \cdot 10^{18}$ | $1.2 \cdot 10^{18}$ | SSC-drips, strong decoupling | ca.7.6 |
| 50 | 10 | 120 | 0 | $1.6 \cdot 10^{20}$ | $2.1 \cdot 10^{19}$ | *Corner flow* | n/a |
| 50 | 10 | 120 | 1000 | $7.8 \cdot 10^{18}$ | $2.4 \cdot 10^{18}$ | SSC-edge | ca.8.7 |
| 50 | 10 | 120 | 3000 | $3.4 \cdot 10^{18}$ | $1.2 \cdot 10^{18}$ | SSC-ripples, weak decoupling | ca.6.6 |
| 50 | 10 | 120 | 5000 | $2.1 \cdot 10^{18}$ | $8.7 \cdot 10^{17}$ | SSC-drips, weak decoupling | ca.8.9 |
| 70 | 5 | 50 | 0 | $3.7 \cdot 10^{20}$ | $2.2 \cdot 10^{19}$ | *Corner flow* | n/a |
| 70 | 5 | 50 | 1000 | $1.7 \cdot 10^{18}$ | $1.1 \cdot 10^{18}$ | SSC-drips, strong decoupling | ca.20 |
| 70 | 5 | 50 | 3000 | $3.2 \cdot 10^{18}$ | $1.4 \cdot 10^{18}$ | Outflow-dominated | n/a |
| 70 | 5 | 50 | 5000 | $2.5 \cdot 10^{18}$ | $1.3 \cdot 10^{18}$ | Outflow-dominated | n/a |

***Table 4.2:*** *Summary of 2-D model cases. For each, slab dip, slab velocity* $\mathrm{v}_{slab}$*, upper plate age* $\mathrm{T}_{upper}$*, wedge water content* $\mathrm{C}_{OH}$*, wedge core viscosity* $\eta_{wedge}$*, subduction channel viscosity* $\eta_{channel}$*, accounts on flow regime, and timescales* $t_{drips}$ *for eventual drip formation are given.*

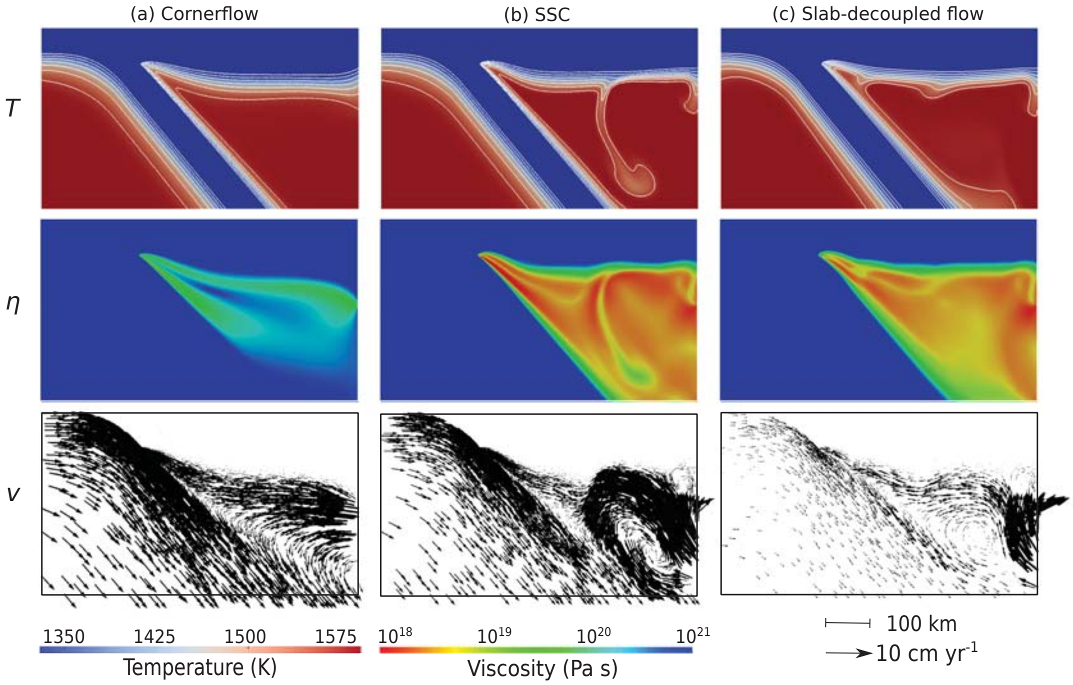

***Figure 4.2:*** *Thermal structure (T), viscosity ($\eta$) and corresponding velocity vectors (V) for example cases with: (a) corner flow; (b) small-scale convection (SSC); and (c) slab-decoupled wedge flow. All models shown have a 120 Myr old upper plate. Models illustrated in (a) and (b) have subduction velocities of 5cm/yr, with (a) dry and (b) wet rheologies, respectively. The model shown in (c), which exhibits a decoupled flow regime, has a subduction velocity of 2cm/yr (hence the smaller velocity vectors) and a wet rheology. Temperature contours range from 1320–1620K, in 50K intervals.*

## 4.4 Flow Styles & Characteristics

In this section, results are described in terms of wedge flow styles and characteristics, using the set of models with an intermediate 50° dip. In Section 4.5, we analyse which parameters exert the main controls on the flow regime.

### 4.4.1 Flow Regimes

We observe three distinct flow regimes in the mantle wedge, across the parameter space examined (Fig. 4.2):

1. **Corner flow**: this flow regime exhibits a stable velocity pattern. Strong coupling between the downgoing slab and the mantle wedge drags sub-lithospheric material towards the wedge corner, where it induces local erosion, or 'pinching' of the overriding plate [e.g. van Keken et al., 2008], and then downwards parallel to the slab (Fig. 4.2a). Such a stable flow configuration allows for relatively unperturbed conductive cooling and thickening of the overriding plate. In previous wedge flow studies, this mode has been promoted by: (i) focusing on flow dynamics under a dry rheology, with wedge-core viscosities that

are at, or above, (the upper mantle average of) $10^{21}$ Pa s; (ii) neglecting buoyancy effects; or (iii) prescribing boundary conditions based on corner flow solutions [e.g. van Keken et al., 2002, Hasenclever et al., 2011].

2. **Small-scale-convective (*SSC*) flow**: in this unsteady flow regime instabilities develop at the base of the overriding plate. In such cases, a corner flow type of drag persists to some degree, so that after formation, instabilities are advected towards the wedge corner. Once developed, instabilities can rapidly increase in vigour and, due to the composite rheology, can attain velocities that exceed the subduction velocity (Fig. 4.2b). Previous studies have found that SSC is promoted by low mantle viscosities, as is expected from wedge hydration [e.g. Honda and Saito, 2003, Arcay et al., 2005, Currie et al., 2008, Wirth and Korenaga, 2012].

3. **Slab-decoupled flow**: in this unsteady flow regime a decoupled convective cell develops at some distance from the slab, which attains velocities far exceeding those of the slab, replacing corner flow or SSC in a large area of the wedge (Fig. 4.2c). This is a mode that most models try to suppress, since the model domain size and boundary conditions used for studying wedge flow tend to result in unrealistically strong and focussed forms of this regime. However, we found that boundary conditions that suppress this flow in our set-up tend to be overly prescriptive on the flow into the wedge. Furthermore, this style is of interest in that it illustrates when the downgoing plate is inefficient at driving wedge flow and, accordingly, other sources of buoyancy, such as the temperature contrast between the slab and the warm wedge-inflow boundary (which likely exists in real subduction settings too), control wedge flow. Such decoupling may, for example, facilitate mantle flow that allows back-arc spreading.

In corner flow models, wedge viscosity is largely dominated by diffusion creep. However, dislocation creep leads to the formation of two low-viscosity areas in regions of high strain-rate: (i) close to the wedge corner, above the interface with the downgoing plate; and (ii) below the upper plate (see viscosity panel on Fig. 4.2a). The former, identified in literature as a 'subduction channel' [e.g. Hebert et al., 2009], stretches from the minimum depth of plate decoupling, down to 150–250km depth; its thickness ranges between 5-km and 20-km. As would be expected, in cases with SSC and decoupled flow, the wedge rheology is modified, through variations in temperature and strain-rates: where instabilities propagate from the lithosphere's base into

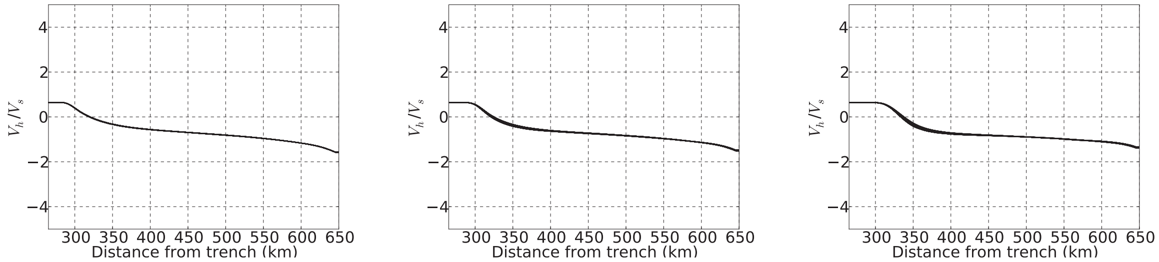

***(a)*** Dry, 10cm yr$^{-1}$, CORNERFLOW

***(b)*** Dry, 5cm yr$^{-1}$, CORNERFLOW

***(c)*** Dry, 2cm yr$^{-1}$, CORNERFLOW

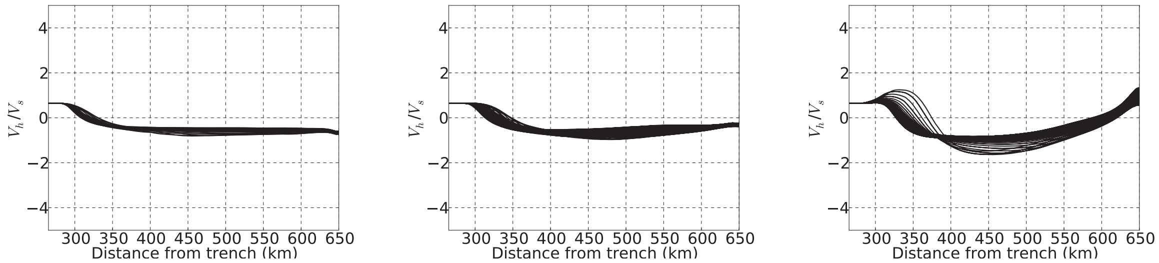

***(d)*** Damp, 10cm yr$^{-1}$, SSC

***(e)*** Damp, 5cm yr$^{-1}$, SSC

***(f)*** Damp, 2cm yr$^{-1}$, SSC, Weak Decoupling

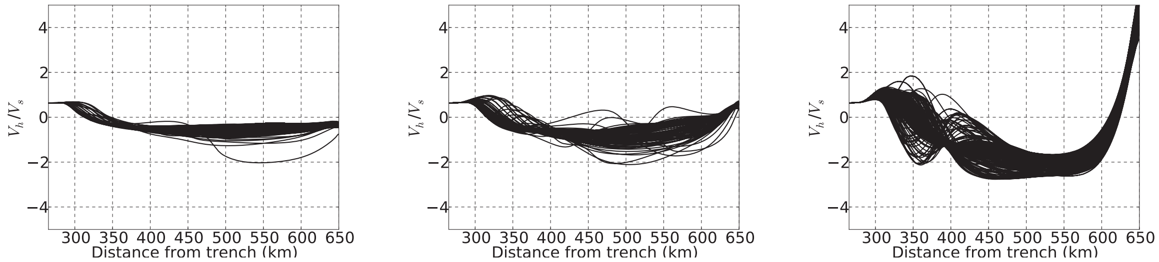

***(g)*** Wet, 10cm yr$^{-1}$, SSC

***(h)*** Wet, 5cm yr$^{-1}$, SSC, Weak Decoupling

***(i)*** Wet, 2cm yr$^{-1}$, SSC, Strong Decoupling

***Figure 4.3:*** *Horizontal velocities at 200 km depth, normalized to slab velocity for: (a-c) dry; (d-f) damp; and (g-i) wet; models with 120 Myr-old upper plates. Shown here are superimposed horizontal velocity snapshots at 0.5 Myr intervals, for a simulation time of 10-40 Myr. Smooth and irregular profiles, respectively, pertain to corner flow and SSC modes; decoupled flow cases have a positive horizontal velocity close to the right-hand-boundary. Positive velocities, on the left of each plot, are associated with return wedge flow immediately above the slab surface.*

the wedge core, regions of higher viscosity can be observed (lower temperatures), which are surrounded by low-viscosity zones (higher strain-rates), thus easing their passage through the mantle wedge. We note that in decoupled flow cases, the feedback between strain-rate and viscosity progressively enhances the strength of decoupled flow: once a decoupled cell develops, it is self-sustaining.

### 4.4.2 Characteristic Velocities

The flow regime's characteristics are best illustrated via horizontal velocity profiles, normalized against slab velocity. Velocities change through time, as flow patterns evolve and/or the lithosphere thickens through diffusive cooling. Examples of superimposed snapshots, at intervals

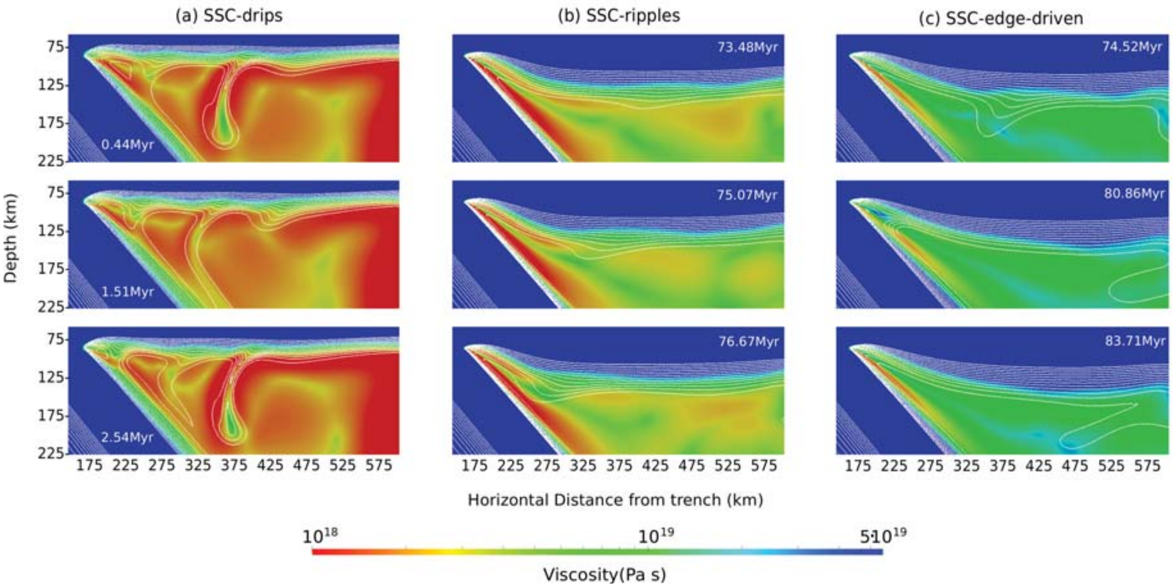

***Figure 4.4:*** *Different styles of small-scale convection (SSC): (a) drips; (b) ripples; and (c) edge-instabilities, respectively, for (a) a very-wet, 2cm/yr, 50 Myr-old upper plate case; (b) a wet, 10cm/yr, 120 Myr-old upper plate case; and (c) a damp, 5cm/yr, 120 Myr-old upper plate case. Temperature contours range from 1320–1620K, in 25K intervals, revealing comparable temperature fluctuations between fully developed drips and sheared ripples, upon interaction with the wedge corner. In all SSC cases, asthenospheric viscosities are below* $10^{19}$ *Pa s.*

of 0.5 Myr, for model times of 10-40 Myr, on a horizontal line at a constant depth of 200-km (i.e. below the overriding plate), are presented in Fig. 4.3. At this depth, corner flow cases (top row) exhibit smooth horizontal velocity profiles, since the flow pattern is regular and approximately steady-state. In SSC-dominated models (middle row), sub-lithospheric instabilities manifest themselves as transient fluctuations in the horizontal velocity profiles. Note that individual instabilities can leave a sequential signature, as their passage across the wedge is registered by more than one snapshot. As cases become more unstable, mantle wedge velocities can exceed those of the subducting slab. In this decoupled flow regime (bottom row), the dominant flow is no longer that towards and parallel to the subducting plate: it is the hot rising material, along the domain's right-hand-side, which leaves through the right-hand boundary. In such cases, a positive horizontal velocity near the right-hand boundary, associated with a flip in the direction of flow, identifies a decoupled outflow 'cell'. Cases where the horizontal velocity exceeds that within the wedge core are termed 'strong decoupling', whilst cases where the horizontal velocity at this boundary is positive, but small in comparison to flow in the wedge core, are termed 'weak decoupling'. Most models are in the corner flow or SSC regime, however in a few end-member cases, the decoupled flow dominates.

### 4.4.3 Styles of Small-Scale-Convection

Several distinct styles of small-scale-convection are observed across the parameter space examined, with Table 6.1 summarising our classification, for all cases. In the most unstable 'SSC-drip' models (Fig. 4.4a), small-scale-convection takes the form of cold, Rayleigh-Taylor type instabilities, which are nucleated in the back-arc region. Here, cold sub-lithospheric material begins to detach, forming downwelling plume-like structures, which penetrate into the wedge core. These drips are more viscous than the surrounding mantle wedge, due to their lower temperatures. They become entrained by background wedge flow and are swept towards the wedge corner, where they induce thermal fluctuations of 50-100K (variations in the thermal structure are discussed, in detail, in Section 4.6). As noted previously, due to the non-Newtonian rheology, low-viscosity zones surround these drips, easing their passage through the mantle wedge. As such, they can attain velocities that exceed the subduction velocity.

'SSC-ripple' cases exhibit instabilities in the form of cold ripples, which remain rooted to the lithosphere's base, and rapidly migrate towards the wedge corner after forming, as a consequence of background mantle flow. In comparison to SSC-drip cases, these ripples have less of an influence on the thermal structure of the wedge core (their expression is more difficult to observe in Fig. 4.4b, for example, but can be identified by tracking the transient sub-lithospheric bulge in the warmest temperature contour plotted). However, they display a comparable influence in the wedge corner, temporarily reducing local temperatures by 50-100K. Instabilities of this form are most notably observed below overriding plates that experience high sub-lithospheric shearing (i.e. cases with high subduction velocities).

In other cases, an instability of a different type is generated, which is nucleated at the edge of the model – 'SSC-edge-driven' instabilities (Fig. 4.4c). In our models, these instabilities largely diffuse away during their passage across the wedge (the exception being the damp 120 Myr old upper plate case with slow subduction, where a robust thermal signature does reach the wedge corner). The same behaviour is exhibited by otherwise corner flow cases, when imposing a strong, dry cratonic corner in the upper right corner of the domain (discussed in Section 4.5.4).

### 4.4.4 Evolution of Upper Plate Lithospheric Thickness

Small-scale-convection is a consequence of upper plate instability. As such, the upper-plate thickness evolves differently under each of the aforementioned flow regimes. It is therefore insightful to examine this evolution over time. We track the 1400K isotherm as a proxy of thermal lithospheric thickness, averaging over a horizontal distance that approximately spans the back-arc length (see the double-pointed dash-dotted arrow, labelled PROBE$_{LITHO}$, in Fig. 4.1), with results presented in Fig. 4.5. We verified this measure against the conductive thermal thickness that can be inferred from lithospheric geotherms. The depth of the base of the conductive layer approximately coincides with the 1400K isotherm and follows the same trends as those displayed in Fig. 4.5. Do note that by $t = 0$ for our analyses, the upper plate has cooled for 5, 10 and 25 Myr, respectively, for fast, intermediate and slow cases and, hence, upper plates differ in thickness, at $t = 0$. We display for each case, lithospheric thickness evolution up to a total upper-plate cooling time of 105 Myr (i.e. until a model time of 100, 95 and 80 Myr, for fast, intermediate, and slow cases, respectively). This allows for a comparison of final thicknesses for all cases.

For corner flow cases with a dry wedge rheology, a continuous conductive thickening of the upper plate is observed. Cases that exhibit SSC also display an average thickening trend with age. However, for the most unstable cases (wetter), we observe: (i) intervals of lithospheric thickening at higher rates than the conductive dry case, which correspond to periods where lithospheric instabilities are growing; and (ii) sudden decreases in lithospheric thickness, when instabilities detach from the upper plate. The net effect is that the lithosphere thickens less in SSC cases, when compared to dry corner flow cases. We note that some of the damp cases examined are an exception to this rule, with thickening more rapid than the dry reference cases over comparable time intervals. Analysis of the convective planform, in such cases, demonstrates that an instability is in the process of forming beneath the lithosphere. However, the time-scale for such instabilities exceeds our simulation time (and likely also those available in natural subduction zones, before other changes in the system occur) and, consequently, these instabilities are unable to develop fully.

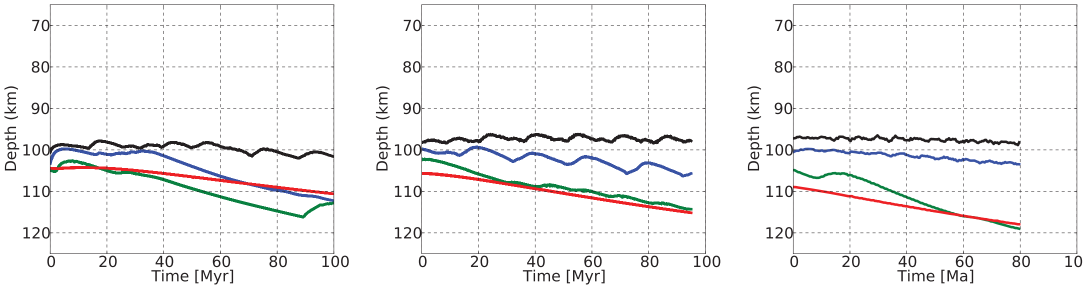

***(a)*** 10cm yr$^{-1}$, 120Myr ***(b)*** 5cm yr$^{-1}$, 120Myr ***(c)*** 2cm yr$^{-1}$, 120Myr

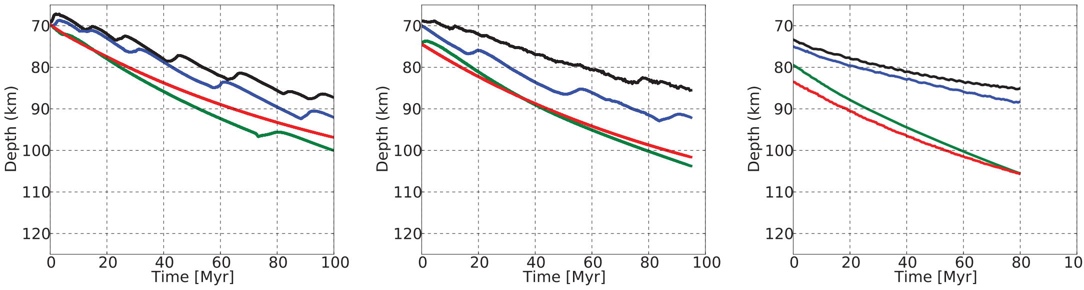

***(d)*** 10cm yr$^{-1}$, 50Myr ***(e)*** 5cm yr$^{-1}$, 50Myr ***(f)*** 2cm yr$^{-1}$, 50Myr

***Figure 4.5:*** *Temporal evolution of the 1400K isotherm's depth (which we use as a proxy for conductive lithospheric thickness), horizontally averaged between 100 km and 350 km from the wedge corner (labelled PROBE$_{LITHO}$ in Fig. 4.1), for all 50°–dip cases. The figures illustrate the sensitivity of lithospheric thickness to subduction velocity, (hydration-dependent) viscosity and overriding plate age. In dry corner flow cases, the overriding plate monotonically thickens with time through diffusive cooling. For wet and very-wet cases, small-scale convection can lead to transient and local periods of thinning, which are associated with detaching drips, thereby counteracting the process of conductive thickening. Cases with an older (120 Myr-old) upper plate are generally more unstable than those with a younger (50 Myr-old) upper plate.*

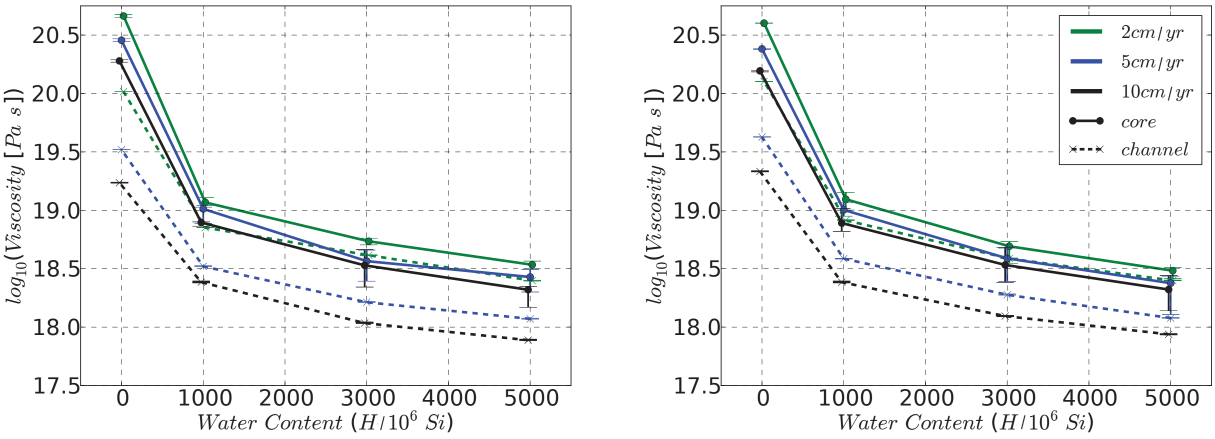

(a) 50Myr

(b) 120Myr

***Figure 4.6:*** *Log$_{10}$(viscosity) in the wedge core (marked $\eta_{core}$ in Fig. 4.1: solid lines) and the subduction channel (marked $\eta_{channel}$ in Fig. 4.1: dashed lines), as a function of wedge hydration, for: (a) 50 Myr-old; and (b) 120 Myr-old upper plates, respectively.*

## 4.5 Flow Style Controls

In this section, we further analyse how plate velocity, wedge viscosity and upper-plate thickness influence wedge flow styles in general (4.5.1), with an emphasis on the style of SSC (4.5.2). We also consider the role of downgoing-plate properties (Sec. 4.5.3) and additional complexities, such as local variations in upper-plate thickness (lithospheric blocks/cratons) and variable wedge hydration (4.5.4 and 4.5.5).

### 4.5.1 Wedge Viscosity, Subduction Velocity & Overriding Plate Properties

To characterise viscosity, we measure it at two locations: (i) immediately above the downgoing plate, to analyse the low-viscosity 'subduction channel', within a 10 km thick parallelogram, marked $\eta_{\text{channel}}$ in Fig.4.1; and (ii) in the wedge core, at a location where mantle mixing is high and velocity fluctuations are minimal, as an indication of background wedge viscosity, within a 25-km square box, located 50-km to the right of the slab tip at 350-km depth (marked $\eta_{\text{core}}$, in Fig. 4.1).

Wedge channel and core viscosities as a function of water content and convergence velocity are shown in Fig. 4.6. Error bars illustrate that, within our measurement boxes, the temporal variation in viscosity is small compared to the range between cases. The chosen rheological parameters lead to a strong decrease in wedge viscosity for wetter conditions. There is a $\sim 1.5$ order of magnitude viscosity difference between dry and damp cases, and a further order of magnitude decrease from damp to very-wet cases. The minimum viscosity attained, for all cases examined, ranges between $8 \cdot 10^{17}$ Pa·s and $6 \cdot 10^{18}$ Pa·s. Due to strain-rate dependence, viscosities decrease with increasing subduction velocity, and the subduction channel is best developed for higher subduction velocity cases. We note that channel and wedge viscosities are largely insensitive to upper-plate age.

Fig. 4.7 documents how variations in slab velocity and wedge hydration relate to the different flow styles for cases with young (50 Myr) and old (120 Myr) overriding plates. Symbols denote variations in SSC style, while the grayscale fill indicates the strength of decoupled flow. Average wedge-core viscosity is annotated. This summary figure illustrates that dry cases, with higher viscosities, exhibit a corner-flow pattern, whereas SSC and decoupled flow become more common with increasing water content. Whether SSC occurs is strongly controlled by wedge viscosity, whilst plate velocity only affects the style and strength of SSC. Cases with an old overriding plate are somewhat more unstable than those with a younger overriding plate ($cf.$ for example, damp cases in Fig. 4.7, which exhibit a corner flow regime for young overriding plates, but an unstable regime for old overriding plates). The decoupled flow regime is not affected by upper–plate age, but is promoted by a combination of low wedge viscosity and low plate velocity.

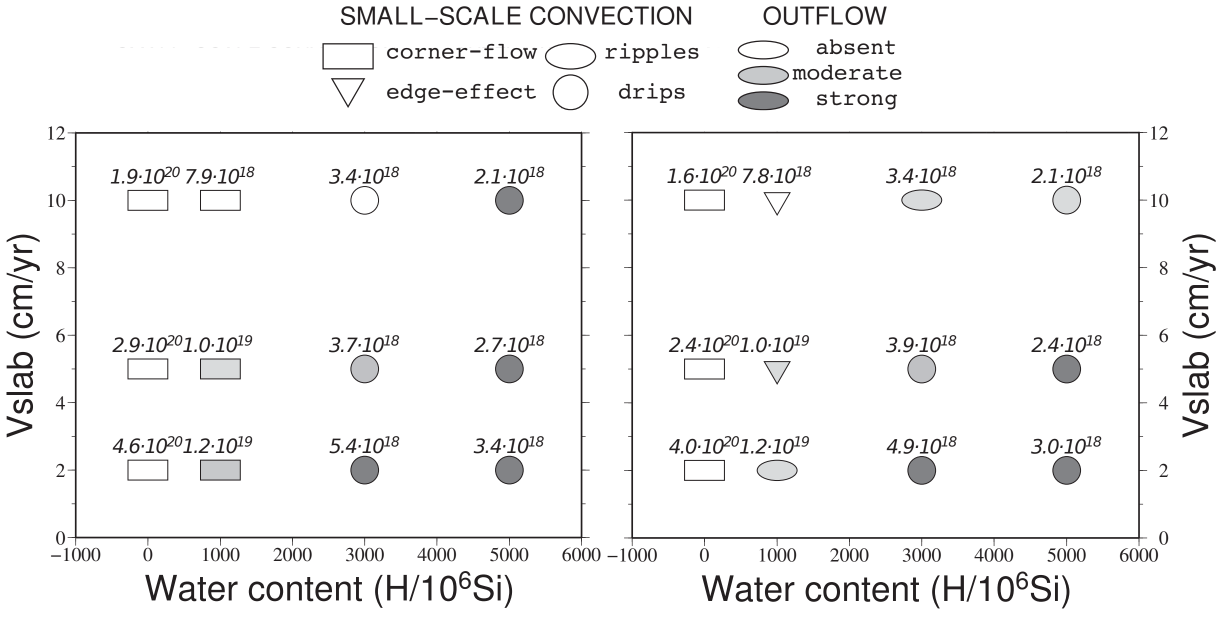

(a) 50Myr

(b) 120Myr

***Figure 4.7:*** *Wedge flow style as a function of slab velocity and wedge hydration, for cases with: (a) 50 Myr-old; and (b) 120 Myr-old overriding plates, respectively. Symbols denote the observed flow regime: rectangles, inverted triangles, ellipses and circles indicate corner flow, edge-driven instabilities, SSC-ripples and SSC-drips, respectively. Light to dark grayscale shading represents the strength of decoupled flow. Annotations indicate wedge core viscosities ($\eta_{core}$ of Fig. 4.1), in Pa·s.*

Sub-lithospheric instabilities arise due to the lithosphere's negative buoyancy, which increases with overriding plate age, thus explaining why cases with an old overriding plate are somewhat more unstable than those with a younger overriding plate. Instability formation is resisted by viscous forces (and thermal diffusion). The increased propensity for SSC at lower viscosities is thus a simple consequence of decreased viscous resistance and, accordingly, an increase in the local Rayleigh number [Davaille and Jaupart, 1994]. As with previous studies, we find that wedge viscosities below a threshold value of $\approx 5 \cdot 10^{18} Pa \cdot s$ are necessary for the development of Rayleigh-Taylor instabilities at the base of the lithosphere [e.g. Honda and Saito, 2003, Wirth and Korenaga, 2012].

Subduction velocities control the vigour of SSC. SSC occurs when the time-scale required to develop a Rayleigh-Taylor drip (a time-scale which is shorter for higher lithospheric density, larger lithospheric thickness and lower lithospheric viscosity) is less than the time-scale with which drips are advected away, in this case, by slab-driven corner flow. Higher subduction velocities lead to a stronger corner flow, which: (i) thins the lithosphere (see Fig. 4.5) and hence the thickness of the layer available for destabilisation, and (ii) shears instabilities before they can fully develop. The influence of subduction velocity is not sufficient to suppress SSC if the viscosity is sufficiently low, however sometimes the style of SSC changes. For example, for the wet wedge below a 120 Myr old upper plate, the instabilities at the highest velocity take the form of ripples rather than drips, and for the fastest damp old upper-plate cases, drips only form at the model edge.

The attenuating effect of shearing velocity on the development of (2-D) SSC that we find is consistent with a range of other analytical and numerical studies [Richter, 1973, van Hunen et al., 2003, Huang et al., 2003], which assumed stress-independent rheology. However, it is opposite to the findings of Currie et al. [2008], who attribute their result to a strong strain-rate softening, where higher subduction velocities lead to a stronger corner flow, which reduces effective viscosities in the mantle wedge. Their strong softening is likely due to the inclusion of a highly strain-rate dependent plastic deformation mechanism. By contrast, in our composite dislocation-diffusion creep models, strain softening is not strong enough to outweigh the intrinsic viscosity factors, and we observe that the growth of instabilities is stunted at high subduction velocities.

Subduction velocity has a larger effect on the generation of decoupled flow, such that the threshold viscosity for significant outflow increases with decreasing velocity. The effect of viscosity is, in this case, two-fold, as lower viscosities: (i) increase the Rayleigh number of local buoyancy-driven flow; and (ii) decrease coupling between the slab and mantle wedge and hence the strength of slab-driven flow. A decreased contribution of corner flow also explains the inverse proportionality between slab velocity and the strength of decoupled flow: as subduction velocities decrease, decoupled buoyancy-driven flow velocities become larger in magnitude than those of slab driven corner flow.

### 4.5.2 SSC Time Scales, Amplitudes, & Lithospheric Erosion

To further understand what governs SSC, we have analysed: (i) time-scales for the observed instabilities; and (ii) the evolution of lithospheric thickness, over time. Fig. 4.8 illustrates the temporal evolution of temperature, in a box at the base of the plate near the wedge corner (labelled PROBE$_T$ in Fig. 4.1). The box was chosen to best capture the instabilities that form: instabilities are spawned from different locations at the base of the overriding plate, but all are advected towards the mantle wedge corner (i.e. close to this corner, most are detected – only a few instabilities die out before reaching the detection box).

In dry cases, we observe a steady flow regime, with no drips. Conversely, in wet and very wet cases, drips manifest themselves as sharp reductions in temperature, as they traverse our detection box. The time interval between instabilities generally increases: (i) with increasing wedge viscosity; (ii) with decreasing subduction velocity; (iii) for thicker (older) upper-plate lithosphere. The first two trends are as expected from the previous section. The third trend is more puzzling, as thicker lithosphere was found to be more unstable, yet instability time-scales are longer.

To better understand the dependence of instability time-scales on lithospheric thickness, the evolution of upper-plate thickness (Fig. 4.5) is summarised for an 80 million year time interval before t=100 Myr, 95 Myr and 80 Myr, for fast, intermediate and slow cases, respectively in Fig. 4.9 (i.e., actual upper-plate cooling time between 25 and 105 Myr). Lithospheric drips are promoted by the Rayleigh number pertaining to the lower layer of the lithosphere that is able to become unstable. The thickness of this layer is related to the thickness of the lithosphere but also depends on lithospheric viscosity and density stratification. The difference in thickness between the dry, conductively-thickening, case and wetter cases, where SSC occurs, is an approximate measure of the thickness of the unstable basal layer of the upper plate.

In dry and damp corner flow cases the lithosphere thickens conductively, but is affected by flow shearing. As a result back-arc lithosphere is about 10 km thinner (95 km instead of 105 km) for

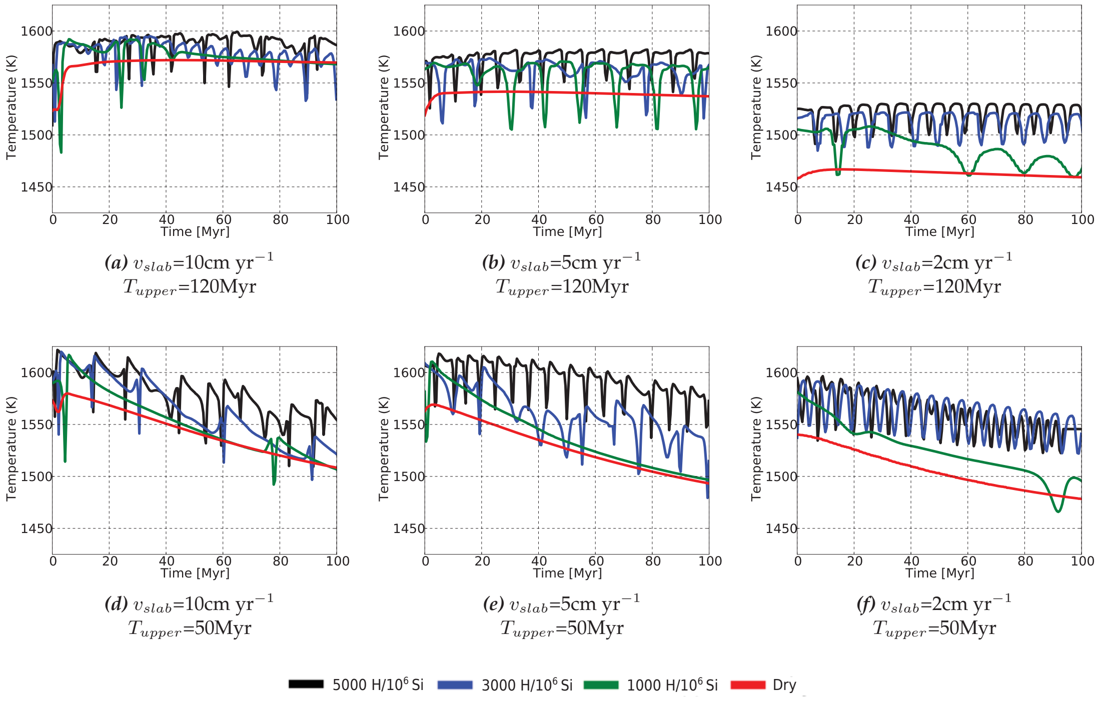

***(a)*** $v_{slab}$=10cm yr$^{-1}$ $T_{upper}$=120Myr

***(b)*** $v_{slab}$=5cm yr$^{-1}$ $T_{upper}$=120Myr

***(c)*** $v_{slab}$=2cm yr$^{-1}$ $T_{upper}$=120Myr

***(d)*** $v_{slab}$=10cm yr$^{-1}$ $T_{upper}$=50Myr

***(e)*** $v_{slab}$=5cm yr$^{-1}$ $T_{upper}$=50Myr

***(f)*** $v_{slab}$=2cm yr$^{-1}$ $T_{upper}$=50Myr

***Figure 4.8:*** *Thermal evolution of the sub-lithospheric area, labelled '$PROBE_T$' in Fig. 4.1, for: (a-c) old; and (d-f) young overriding plates, as a function of wedge hydration and subduction velocity. Drips propagating through the box result in transient low-temperature troughs. Older, thickened plates destabilize more efficiently, promoting small-scale convection in all hydrated cases. Increased hydration leads to more unstable behaviour, which is characterised by smaller and more regular time intervals between drips.*

a case with a subduction velocity of 10 cm/yr, when compared to a case with a subduction velocity of 2 cm/yr. In wetter cases, where SSC develops, subduction velocity has a less significant affect on lithospheric thickening. The net result of corner flow shearing and lithospheric instabilities is that, generally, the upper plate thickens most for the highest wedge viscosities, whilst low wedge viscosities lead to efficient upper-plate erosion, thus limiting lithospheric thickening (Figs. 4.5 and 4.9). Interestingly, the thickness of the unstable layer does not differ substantially between young and old upper-plate cases (Fig. 4.5). In either case, the unstable part of the lithosphere for the lowest (wettest) wedge viscosities is between 10 km (for the highest velocities) and about 20 km (for the lowest velocities) thick. This result is in fact consistent with scaling analyses by Davaille and Jaupart [1994], which predict that, while instability time depends on local Rayleigh number, thickness of the unstable layer and temperature contrast across this layer are determined by mantle temperature and the sensitivity of viscosity to temperature changes (i.e., activation energy) and thus would not vary significantly with lithospheric age. This implies that a larger proportion of the younger than the older lithosphere is destabilised. We analysed viscosities, and it appears that for the younger plate, the net effect of temperature- and depth-dependent viscosity is that the unstable layer has a lower viscos-

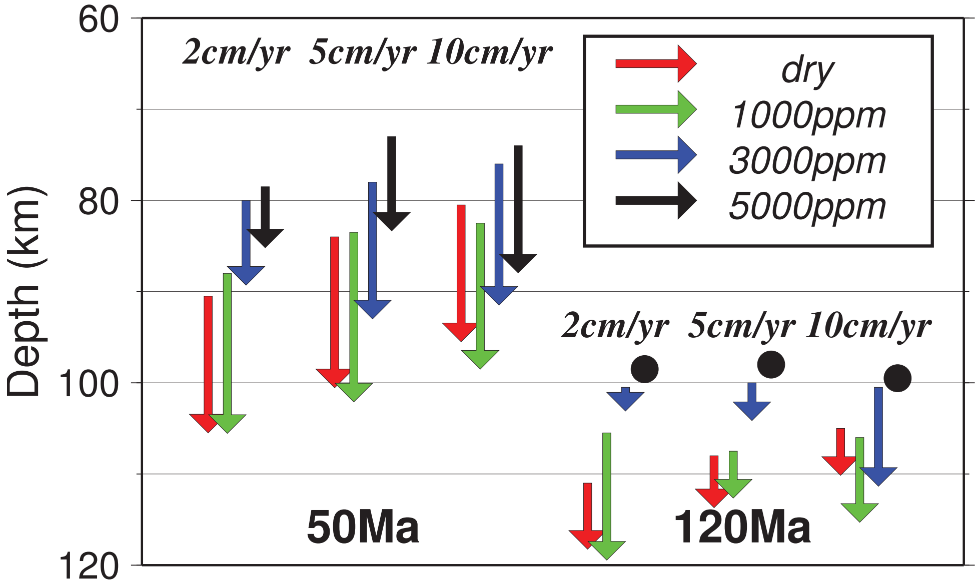

***Figure 4.9:*** *Summary of lithospheric thickening, in the time interval 20-100 Myr, 15-95 Myr and 0-80 Myr, for fast, intermediate and slow cases, respectively (thus corresponding to a similar total lithospheric cooling time – see Fig.4.5) as a function of subduction velocity and wedge hydration.*

ity than in the case of the older plate. This would be associated with a larger local Rayleigh number, and explain the shorter drip time scales for the younger plate. Nonetheless, older lithosphere is intrinsically more unstable than younger lithosphere, due to its larger overall negative buoyancy, as evidenced by the fact that SSC occurs for damp cases with a 120 Myr old upper plate, but not damp cases with a 50 Myr old upper plate, similar to what has been established in many studies on oceanic lithosphere [e.g. Davaille and Jaupart, 1994, van Hunen et al., 2003].

There are additional complexities in this unstable dynamic system. The weaker styles of SSC (ripples and edge-controlled) follow anomalous time-velocity trends. Furthermore, drip amplitudes vary (Fig. 4.8), sometimes alternating between strong and weak drips, which are the result of different or interacting instabilities. Instabilities often spawn at different locations and, in some cases, multiple instabilities can coexist (e.g. $C_{\mathrm{OH}} = 5000\ \mathrm{H}/10^6\mathrm{Si}$, 2cm/yr case). In the most unstable cases, drips tend to form in the back arc were the upper–plate thickness is relatively constant. In other instances, the region where the lithosphere starts to pinch above the wedge corner serves to localise an additional, or the only, instability. Instabilities that form closer to the wedge corner have less time to grow and, therefore, have a different amplitude to those forming adjacent to model's right-hand side. Multiple drips can also coalesce near the wedge corner, resulting in variable amplitudes.

### 4.5.3 Lower Plate Parameters

In general, the thermal and flow structure of the mantle wedge are principally affected by rheological variations, upper plate behaviour and subducting velocity. Other parameters, such as downgoing plate dip and age have only a secondary effect. Nonetheless, we discuss the modifying role of these parameters in this section.

#### Downgoing Plate Age

The models discussed above all have a downgoing plate with a thermal age of 50 Myr at the trench. On Earth, however, the age of the downgoing plate varies between 0 Myr at Cascadia and 160 Myr at Izu-Bonin-Mariana [e.g. Sdrolias and Müller, 2006] and it is important to examine the significance of such variations. We have done so, by testing how a plate age of 100 Myr at the trench modifies results. As expected, older slabs have lower slab-surface temperatures (by $\approx$70K), which will influence slab dehydration [e.g. Syracuse et al., 2010] (see Section 4.6 for further discussion). However, consistent with the recent study by Wirth and Korenaga [2012], we find that the subducting slab age has a negligible effect on wedge dynamics. This is to be expected in models where slab motion is kinematically prescribed: convective processes in the wedge are sufficiently strong that thermal diffusion has only a minor impact on the flow field. We note, however, that the role of downgoing plate age is likely more important in dynamic subduction models, where slab motion and geometry adjust in response to buoyancy forces and rheology, which are both dependent upon slab age [e.g. Arcay et al., 2005, Capitanio et al., 2007].

#### Slab Dip

To investigate how slab dip influences SSC, we have examined additional cases, where the subducting plate dips at angles of 30° and 70° (all cases have an intermediate subduction velocity of 5 cm/yr and a 50 Myr old upper plate). Flow styles, as a function of dip and wedge hydration, are illustrated in Fig. 4.10, with wedge-core viscosities annotated. For our wet and very-wet cases, decreased wedge viscosities at higher dips may be expected to decrease upper-plate stability. However, we observe SSC for the 30° and 50° dip models, under approximately the same conditions, but with smaller instability time-scales for the 30° dip case (Fig. 4.11), indicating that it is more, rather than less, unstable in comparison to the 50° case. Results for the 70° dip slab cannot really be compared to the 30° and 50° dip cases. In this model, the subducting slab is inefficient at driving wedge flow, which facilitates the development of a decoupled outflow cell. In the damp 70° dip case, some SSC develops, but for the wetter cases, outflow dominates the flow regime. Our results for the sensitivity of SSC are, therefore, very different to the study by Wirth and Korenaga [2012], who, in models of longitudinal SSC, found that increasing dip led to enhanced lithospheric instability.

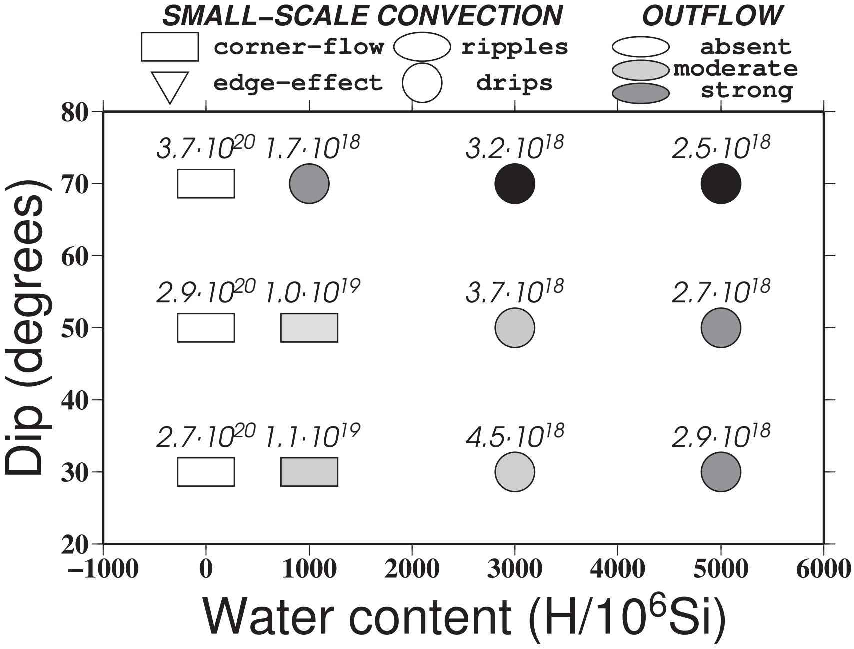

***Figure 4.10:*** *Wedge flow style as a function of slab dip and water content, for cases with 50 Myr old upper plates and a subduction velocity of 5cm/yr. As in Fig. 4.7, rectangles, circles and triangles respectively denote corner flow, SSC drips, and outflow-dominated cases without SSC. Light to dark grayscale shading represents weak to dominating outflow patterns. Annotations denote wedge core viscosities in Pa·s, measured, as for the 50°-dip case, in a 25 km square box at 350 km depth, 50 km in front of the slab tip.*

Examination of the convective planform of each case suggests that the observed variability in strength and time-scales of SSC between the 30° and 50° dip models is controlled by the longer upper plate in the 30° model. As can be seen for the dry, conductively thickening case (Fig. 4.11), the larger domain of the 30° dip model (and thus larger distance between the trench and the fixed upper-plate temperature boundary) allows for more conductive thickening in comparison to the smaller-domain 50° dip case. This enhanced thickening results in a thicker unstable layer and decreased instability time–scales. The longer lithosphere also provides more space for instabilities to form according to their intrinsic wavelength (rather than being controlled by model boundaries or the lithospheric gradients above the wedge corner). This leads to a much more regular destabilisation pattern of the wet 30° case than the wet 50° case. The instability wavelength of the very-wet case was already significantly smaller than the upper-plate length for the 50° case (around 150 km) and, hence, for this case, the effect of dip is less pronounced, although lithospheric thinning for both wet cases is more efficient in the smaller dip models (Fig. 4.12).

These results further illustrate the complex nature of this system. While we could design a set of models where upper-plate length does not vary with dip, such models will necessarily differ in other respects (e.g. depth extent of the models or boundary conditions at the bottom boundary, which would also affect wedge flow). Nonetheless, we can conclude that the influence of slab dip is relatively mild. Modifications of the upper-plate have a stronger influence, as we will next illustrate.

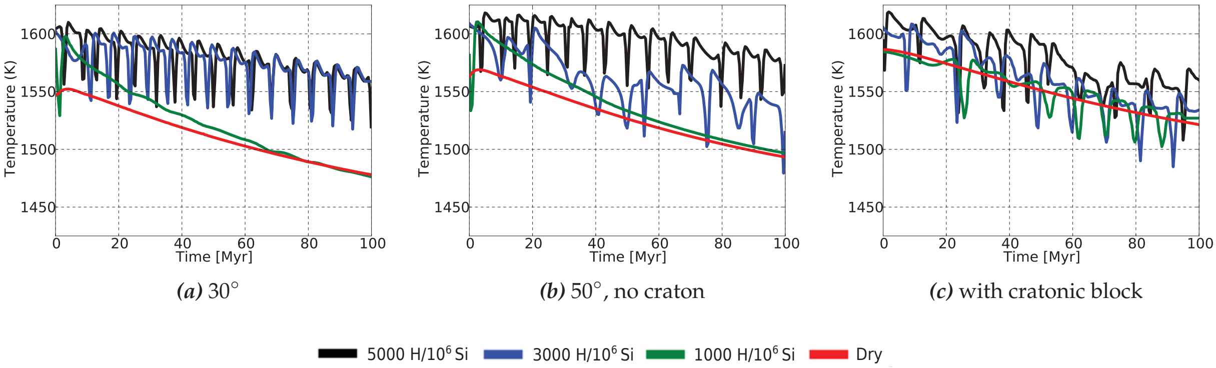

***(a)*** 30° ***(b)*** 50°, no craton ***(c)*** with cratonic block

***Figure 4.11:*** *Temperature evolution at the base of the lithosphere for a few variations on the reference case. All models have 50 Myr-old overriding plates, subduction velocities of 5 cm/yr and a range of water contents: (a) displays a model with a dip of 30°; (b) denotes the 50° dipping case, previously presented in Fig. 4.8e; whilst (c) is for a variant of the model in (b), with a strong lithospheric block / craton, on the right–hand–side of the domain.*

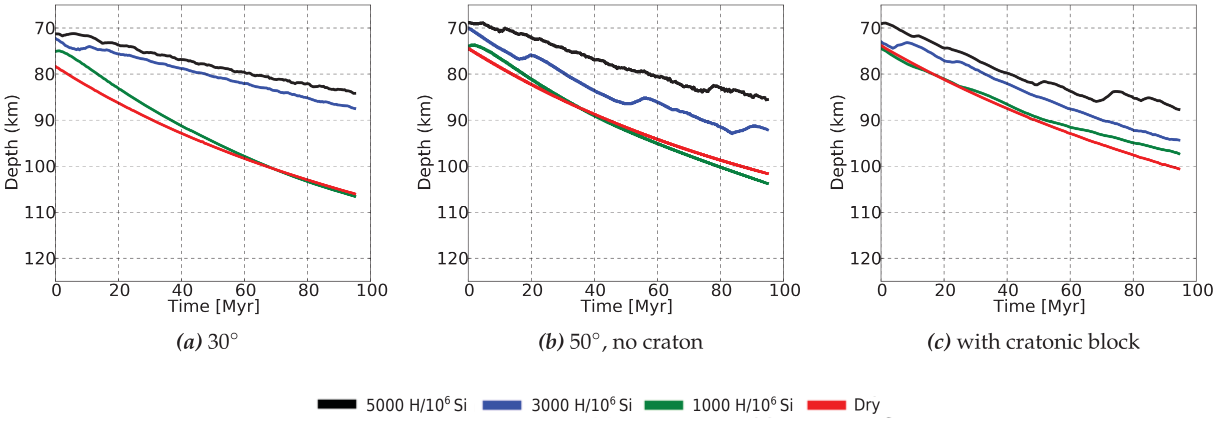

***(a)*** 30° ***(b)*** 50°, no craton ***(c)*** with cratonic block

***Figure 4.12:*** *As in Fig. 4.5, but for a few variations on the reference case. As in Fig. 4.11 all models have 50 Myr-old overriding plates, subduction velocities of 5 cm/yr and a range of water contents. (a) and (c) are variations on the 50° dipping reference model for which lithospheric thickness is displayed in (b): (a) is for a model with a smaller dip of 30° whilst (c) illustrates a model with cratonic block on the right–hand–side of the domain.*

### 4.5.4 Lithospheric Steps

On Earth, back-arc lithosphere is often non-uniform and may contain discontinuities/steps in thickness (e.g. at the continent-ocean boundary, between tectonic and stable continental block boundaries, or as a result of differential hydration [Arcay et al., 2006, Currie et al., 2008]). Such lithospheric steps are well-known nucleation points for instabilities, giving rise to a style of SSC commonly known as edge-driven convection [e.g. King and Anderson, 1998, Hardebol et al., 2012]. In some of our cases, edge-instabilities form adjacent to the no-flow boundary condition at the upper-right-hand side of the model (see Fig. 4.4c). Such a boundary condition will have similar dynamical consequences to a step that would occur on the edge of a thicker and high-strength lithospheric block. To further examine the role of edge-instabilities, we include a thicker and stronger block at the top-right-hand corner of the domain, with dimensions $200 \times 200$ km, and a fixed viscosity of $10^{24} Pa \cdot s$, in a model with a 50 Myr-old upper plate. The influence of such a block on instability time-scales and lithospheric thickening are illustrated in Figs. 4.11(b)/(c) and 4.12(b)/(c), which highlight two key observations:

1. The edge of the lithospheric block allows regular nucleation of instabilities for the damp case, which was marginally stable for models without such a block (cf. Fig. 4.11b/c). As a consequence, lithospheric thickness decreases for the damp case, when a craton is present (cf. Fig. 4.12b/c).

2. As demonstrated in Section 4.5.3, conductive lithospheric thickening is enhanced in cases with longer upper plates, and the time-interval between gravitational instabilities is more regular. When a stable, fixed craton is introduced (in a model where the domain size remains fixed), the length of lithosphere that is able to destabilise decreases. Accordingly, the time-intervals between instabilities and the amount of lithosphere that they destabilise become more irregular. Indeed, for the wet and very-wet cases, the lithosphere was sufficiently unstable in the absence of the craton – the addition of a strong cratonic block, therefore, does not enhance instability. Rather, the additional space constraints lead to slightly increased intervals between instabilities, in both cases, and a minor increase in lithospheric thickness.

The net effect of a step in lithospheric thickness, therefore, is strongly dependent upon the subduction setting. Nonetheless, in cases that are marginally stable, a step in lithospheric thickness may play an important role in triggering SSC.

### 4.5.5 Wedge-Corner Hydration

Investigations into the stability fields of hydrous phases indicate that slab dehydration is limited to a depth of about 200-km [e.g. Schmidt and Poli, 1998]. While it remains unclear how water is transported through the mantle wedge, several proposed mechanisms lead to a relatively vertical migration from the point where it is released ([e.g. Gerya and Yuen, 2003, Gerya et al., 2006, Gorczyk et al., 2007, Zhu et al., 2009]). The consequence of such fluid migration would be that significant hydration is limited to the wedge corner, as was modelled by Arcay et al. [2005, 2006], Cagnioncle et al. [2007] and Hebert et al. [2009], and as was assumed by Honda and Saito [2003], Manea and Gurnis [2007], Currie et al. [2008] and Honda et al. [2010].

Our results, thus far, demonstrate that the propensity for SSC is controlled by lithospheric density, strength and thickness, in addition to steps in upper-plate properties and the length of the upper-plate that is available for destablisation. Hydration localised to the wedge corner introduces a step in strength of the upper plate, which would facilitate instability nucleation. However, at the same time, limiting hydration to the wedge corner would significantly limit the region over which instabilities can form. To quantify the net effect of such localised hydration, we have examined several cases where the extent of the hydrated corner is varied, in addition to the difference in water content between the corner and back-arc region.

We find that if the back-arc is dry or damp, no drips form for hydrated corners that extend 100 km, or less, from the slab-upper-plate decoupling point: in such a small region the wavelength of a Rayleigh-Taylor instability exceeds the length of the water-weakened upper plate. In our reference models, the minimum wavelength of instabilities, in cases with strong hydration throughout the wedge, was 120–150 km. As such, when the hydrated corner extends 150 km from the decoupling point, drips form when the back-arc is dry and the corner is very-wet. However, they do not form if the corner is wet, or if the back-arc is damp. For a hydrated corner extending 200 km from the decoupling point, instabilities do form for the smaller viscosity contrast between a wet or very-wet corner, and a damp back-arc (Fig. 4.13). The chief reason that SSC occurs in the very-wet corner/dry back-arc case, for the 150 km extent hydrated corner, is the strong viscosity contrast, which provides a nucleation point for instabilities. In addition, for the high-viscosity dry rheology, corner flow is most efficient at eroding the lithosphere over the wedge tip, thus keeping the wedge corner warm enough for instabilities to form.

Thus, if only part of the mantle wedge is significantly hydrated, SSC may only ensue under favourable conditions, where lithospheric destabilisation in encouraged by hydration to at least

150-km from the wedge corner (corresponding to a slab depth of 200-km for a 50° dip case), and is aided by high plate velocities (and probably larger dips), which allow corner flow to keep the wedge corner relatively hot. Previous studies that found SSC in models where only the wedge corner was hydrated assumed a dry back-arc mantle and strong water-weakening in the wedge corner. As in these models, our simulations also show that the lithospheric instabilities mainly nucleate at the dehydration boundary, and lead to enhanced thinning of the hydrated lithosphere, when compared to the damp/dry lithosphere.

Observations show that a hot, thin lithosphere back-arc is common [Currie and Hyndman, 2006]. When combined with the finger-like seismic structures that are observed in the arc corner below Japan Tamura et al. [2002], these are strong indications that the conditions necessary for SSC are quite often met in natural subduction settings.

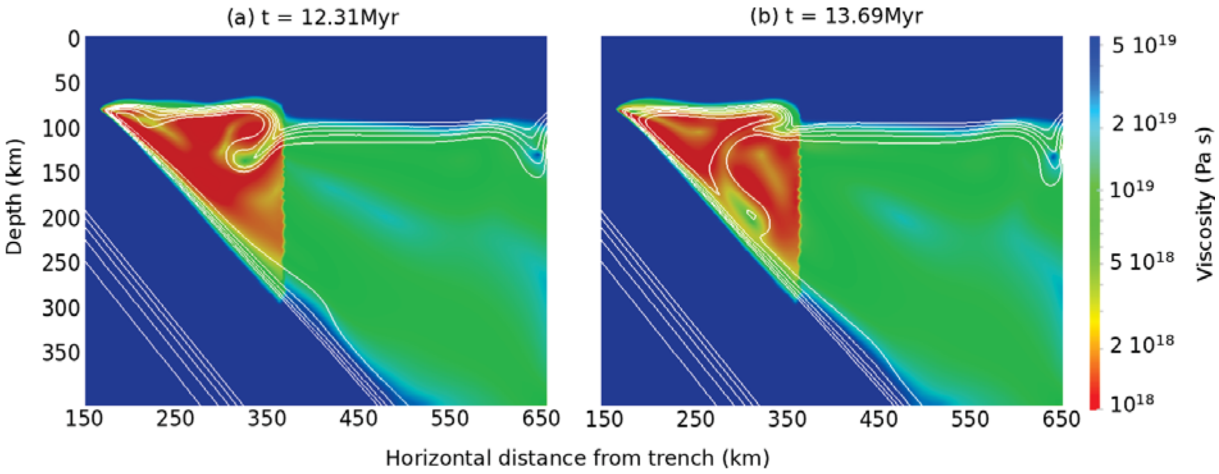

***Figure 4.13:*** *An example case with SSC, when only the wedge corner is hydrated, illustrating the evolution of instabilities and their interaction with the slab surface. In the case shown, the wedge corner and overlying lithosphere are very-wet, whilst the back-arc is damp. The upper plate is 50 Myr old and the plate subducts at a velocity of 5 cm/yr. The hydrated corner extends 200 km from the decoupling point, where the slab surface reaches 250 km depth. Temperature contours range from 1500-1600K, in intervals of 25K.*

## 4.6 Implications for Wedge Thermal Structure

The mantle wedge's flow regime strongly affects upper plate structure, slab dehydration conditions, the wedge's thermal structure and the extent and mode of melting [Arcay et al., 2005, 2006, 2007, Currie et al., 2008]. Each of these are next discussed.

### 4.6.1 Upper-plate Evolution

Thinning of the upper plate beneath the volcanic arc exerts an important control on the scale and location of the melt zone, the mode of melting, and the depth of mineral dehydration at and above the slab's surface. Lithospheric thinning beneath the back-arc facilitates the localisation of deformation, including the formation of back-arc spreading centres, and back arc melting.

#### Fore-arc Lithosphere

Several previous studies have documented that kinematically driven wedge-flow models develop enhanced erosion, or 'pinching', of the upper plate beneath the fore-arc, when coupling between upper and lower plates is prescribed to a given depth [e.g. Conder, 2005, Arcay et al., 2005, 2007]. Our dry models are consistent with these previous studies, with a clear pinch zone developing beneath the fore-arc and extending as shallow as our minimum coupling depth of 80 km. For some of our damp cases, mild pinching is observed, which introduces a strong gradient in lithospheric thickness beneath the fore-arc, from which instabilities can nucleate. For wet and very-wet cases, the pinch zone is poorly developed. However, in these cases, lithospheric thinning occurs over a larger region (including the fore-arc and volcanic-arc regions), due to SSC that nucleates beneath the back-arc. We note that in published models with a dynamic slab and rheologically controlled coupling, lithospheric erosion in the fore-arc region is enhanced relative to our models [Arcay et al., 2005, 2007]. Consistent with previous studies, we find that pinching is enhanced in models with higher subduction velocities.

#### Back-arc Lithosphere

A number of observations indicate that several back-arc regions, not recently subjected to extension, are characterised by relatively thin lithosphere (≈60-km), over distances of 200–900-km from the trench. These observations include: (i) high back-arc surface heat flow ($> 70$ mWm$^{-2}$ for continental crust with radiogenic heat production; $> 60$ mWm$^{-2}$ for oceanic crust); (ii) low seismic velocities at 50–100-km depth; (iii) temperature estimates from mantle xenoliths; and

(iv) widespread sporadic volcanism [Currie and Hyndman, 2006]. Most available measurements are for continental back-arcs, but include a few oceanic regions [e.g. Currie and Hyndman, 2006, Manga et al., 2012]. Zones of active back-arc extension also regularly exhibit very slow mantle velocities, up to relatively shallow depths [e.g. Currie and Hyndman, 2006, Wiens et al., 2008]. Currie and Hyndman [2006] proposed SSC at the base of hydrated lithosphere as a mechanism for lithospheric thinning and, subsequently, demonstrated that this can lead to rapid and substantial thinning of a hydrated visco-plastic plate [Currie et al., 2008].

In our models with a composite dislocation-diffusion creep rheology, thinning is less strong and rapid: in our wet and very wet cases that exhibit SSC, upper-plate thicknesses of around 70-km are observed at a thermal age of 60 Myr, and around 85-km after 100 Myr (Fig. 4.12), which are slightly greater than the thicknesses of 60-km, inferred by Currie and Hyndman [2006]. Nonetheless, the lithosphere in our wet and very wet cases can be 20-km thinner (after 100 million years of cooling) than in the dry, corner-flow cases, implying that SSC has a significant influence on upper plate evolution. For the unstable cases, back-arc surface heat-fluxes are in the range of 50-65 mWm$^{-2}$, when we account for radiogenic heating within the continental crust (at a heat production rate of 1.3 Wm$^{-3}$ in the upper crust down to 15 km depth, and 0.27 Wm$^{-3}$ in the lower crust down to 50 km depth), and 35-55 mWm$^{-2}$, in the absence of such internal heating (i.e. in oceanic regions). These values are at the lower end of observations [Currie and Hyndman, 2006].

We note that our lithospheric thicknesses are greater than those inferred by Currie and Hyndman [2006], although all of our models have relatively high plate ages (cooling ages are 55 Myr, or older). Nonetheless, studies of SSC beneath oceanic lithosphere indicate that younger plates have not acquired sufficient negative buoyancy to destabilize [Davaille and Jaupart, 1994, van Hunen et al., 2003], whilst continental lithosphere is commonly older than oceanic lithosphere and, hence, would not be expected to be thinner than 55 Myr old oceanic lithosphere. We find that thinning is most efficient when a large section of the upper plate is hydrated: given that the largest distances of thin, hot back-arcs correspond to zones that have experienced significant trench retreat (e.g. Aleutians, Kamchatka), this may suggest that dehydration by melt extraction is less efficient than wedge hydration by the downgoing plate, at least when trench retreat occurs rapidly.

### 4.6.2 Slab Surface Temperatures

The rate at which a slab is heated during subduction controls the depths where hydrous minerals destabilize and, therefore, release their fluids into the overlying wedge [e.g. Peacock, 1990a, Peacock and Wang, 1999, Poli and Schmidt, 2002]. In Fig. 4.14, we show examples of model geotherms at the slab's surface, alongside dehydration boundaries for oceanic crust [Hacker, 2008] and the stability fields for hydrous mantle minerals [Grove et al., 2009].

Below 80-km (i.e. the upper-lower plate decoupling depth), temperatures can vary by almost 100 K between different cases. We find that higher subduction velocities, higher wedge viscosities and larger upper plate thickness all result in decreased SSTs, which is consistent with recent studies by Lee and King [2009] and Syracuse et al. [2010]. As such, the completion of dehydration for MORB material at the slab's surface (taken as the boundary where water content drops below 0.1 wt %) can shift by 5–25 km, between the different models examined. It is important to note that in addition to controlling crustal dehydration, SSTs can also affect the dehydration of mantle minerals [e.g. Peacock, 1990b, 1996, van Keken et al., 2011], where they are exposed at the slab's surface (e.g. in oceanic core complexes). Indeed, if mantle minerals are exposed, the range of predicted model SSTs could shift the depth where serpentinite and chlorite break-down by as much as 25-km.

Temperatures within the slab's mantle lithosphere and, hence, the dehydration of mantle minerals below the oceanic crust, are principally dictated by subduction velocities rather than wedge dynamics [Syracuse et al., 2010]. As such, they are not examined here. However, temperatures within the thermal boundary layer above the slab are strongly affected by wedge dynamics. In this thermal boundary layer, hydrous mantle minerals take up water released from the slab until temperatures exceed their stability and fluids are released to migrate through the wedge core or form hydrous melts [e.g. Grove et al., 2012]. The thermal boundary layer will further be affected by 50–100K fluctuations in temperature that are caused by drips from the upper plate, which can be entrained with the flow above the subducting plate (e.g. Fig. 4.13b). We note that in our models, the temperature fluctuations associated with instabilities do not significantly affect the slab surface (aside from the general cooling trend, we see no evidence for transients in our SSTs over time). Conversely, in models by Arcay et al. [2005], where extreme thinning of the upper plate occurs in the arc region, drips are strong enough to result in significant time-dependent cooling of the slab surface.

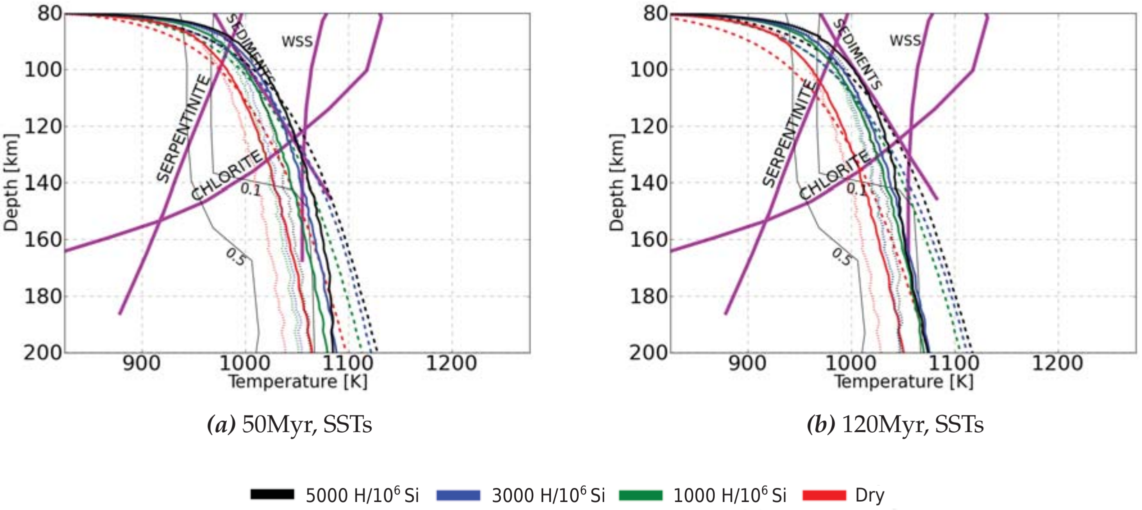

***(a)*** 50Myr, SSTs ***(b)*** 120Myr, SSTs

***Figure 4.14:*** *Slab surface temperatures (SSTs) for a number of models. Dotted, continuous and dashed lines represent models with fast, intermediate and slow subduction velocities, respectively, with: (a) a 50 Myr-old upper plate; and (b) a 120 Myr-old upper plate, at a simulation time of 30 Myr. Thin solid black lines are dehydration boundaries (in w.t.%) for an oceanic crustal composition [Hacker, 2008]. The solid magenta lines denote the water-saturated peridotite solidus (labelled WSS), the water-saturated solidus for sediment, and the margins of chlorite and serpentinite stability fields [Grove et al., 2012].*

### 4.6.3 Wedge-core Temperatures & Melting

If a constant viscosity is assumed, analytical scaling relations for mantle wedge temperatures predict that the maximum temperature in the wedge corner scales with the dimensionless quantity: $v_s r \delta^2/\kappa$, where $v_s$, $r$, $\delta$ and $\kappa$ denote subducting slab velocity, distance from the wedge corner, slab dip and thermal diffusivity, respectively [England and Wilkins, 2004]. In general, our composite viscosity models are consistent with this relationship: wedge corner temperatures tend to increase with subduction velocity, due to enhanced lithospheric thinning and pinching of the upper plate, whilst increasing slab dip allows more warm mantle material into the wedge corner. However, as demonstrated herein, the hydrated rheology modifies the flow regime substantially and, accordingly, exerts a stronger control on wedge temperatures than the basic kinematic parameters of slab dip and subduction velocity. Furthermore, under such a hydrated rheology, SSC induces temperature fluctuations of 50–100 K, on time-scales of a few million years (Fig. 4.8). It is therefore important to analyse how such variations in the flow regime, and transient fluctuations in temperature, influence the location, extent and mode of melting within the mantle wedge.

Regions of our models where pressure and temperature conditions exceed the wet and damp solidi of Katz et al. [2003] are illustrated in Fig. 4.15. We include only figures for dry, damp and wet cases, as the melt regions for wet and very-wet cases are qualitatively very similar. In addition, we draw damp and wet melting contours on all models, as there may be small–scale processes leading to localised high concentrations of fluids that allow for damp/wet melting, but are insufficient to affect the overall rheology [e.g., Gerya et al., 2006, Zhu et al., 2011]. This also facilitates comparison between the temperature conditions achieved in different models.

Consistent with recent studies by Grove et al. [2009] and England and Katz [2010], our results demonstrate that melting temperatures are most likely to be exceeded in the wedge corner, below the volcanic-arc region, where high temperature isotherms are drawn up to shallow depths. As a consequence, the region where melting is possible is largest for models with the highest subduction velocities, which exhibit the strongest pinching. In almost all of our models, there is a region, below the volcanic-arc, where the wet solidus is exceeded, the exception being the dry, low-velocity case, where the lithosphere is too thick to permit melting (see Fig. 4.15a). In some cases (for example, the wet case with a subduction velocity of 10 cm/yr - see Fig. 4.15f), there is also a small region where damp melting is possible.

In cases where SSC has thinned the upper plate sufficiently, wet melting is possible beneath the back-arc. Whilst the extent of this melt zone is greater for younger upper plates, a thin wet melting region does occur beneath older plates. Significantly, the temperature fluctuations induced by propagating instabilities are sufficient to disrupt melting processes beneath the back-arc and volcanic-arc (cf. Fig. 4.15e/f). Honda and Yoshida [2005] proposed SSC to be the cause of time-dependent volcanism in the Japan arc: our models demonstrate that thermal fluctuations, induced by SSC, are sufficient to temporarily shut down the melt supply, on timescales of a few million years (i.e. the time taken for a drip to propagate through the melt zone).

We note that none of the cases examined herein exhibit a thin enough lithosphere beneath the volcanic-arc to permit dry melting. Whilst this is consistent with studies by Grove et al. [2009] and Syracuse et al. [2010], it differs to the predictions of models where shallower coupling depths are imposed [e.g. England and Katz, 2010, Harmon and Blackman, 2010]. We also note that wedge and slab-surface temperatures would be increased by up to 70K in our models, had we accounted for the effects of mantle compressibility and viscous dissipation, although this is only a secondary effect [Lee and King, 2009].

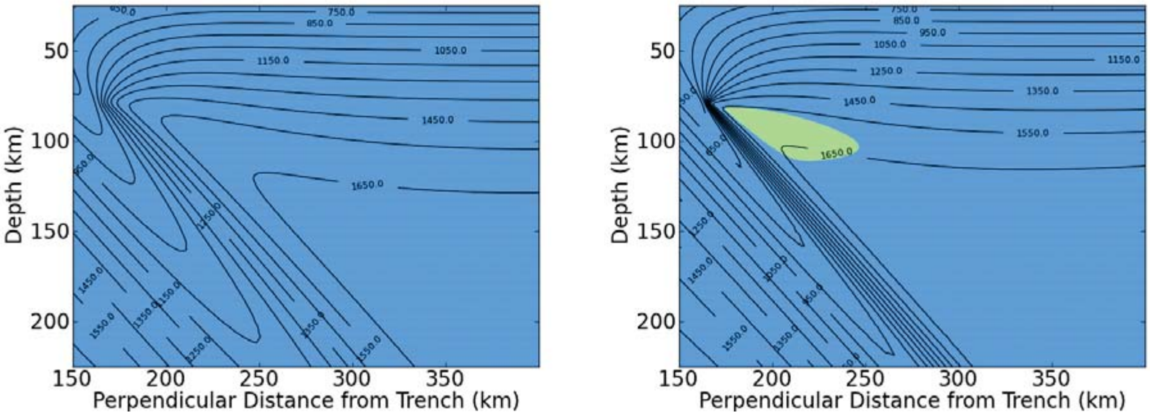

*(a)* Dry, 2cm/yr, t=10 m.y.

*(b)* Dry, 10cm/yr, t=30 m.y.

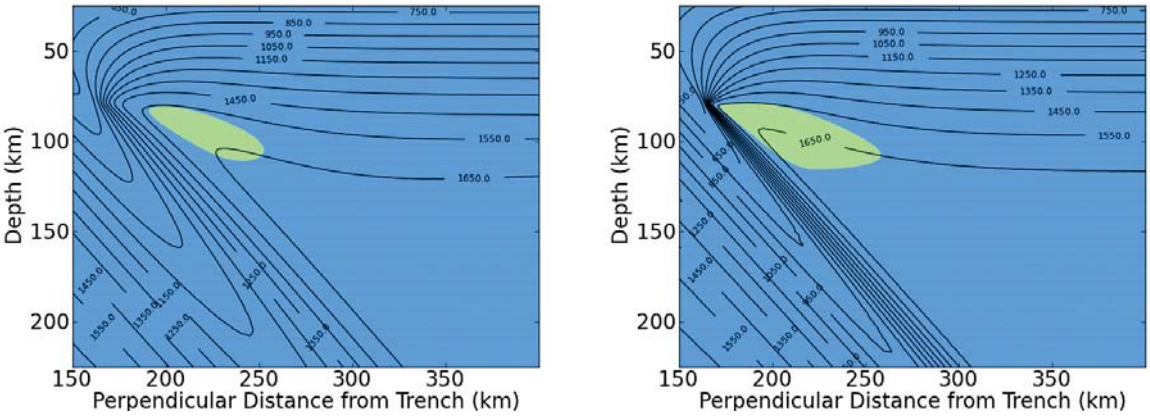

*(c)* 1000 H/$10^6$Si, 2cm/yr, t=10 m.y.

*(d)* 1000 H/$10^6$Si, 10cm/yr, t=30 m.y.

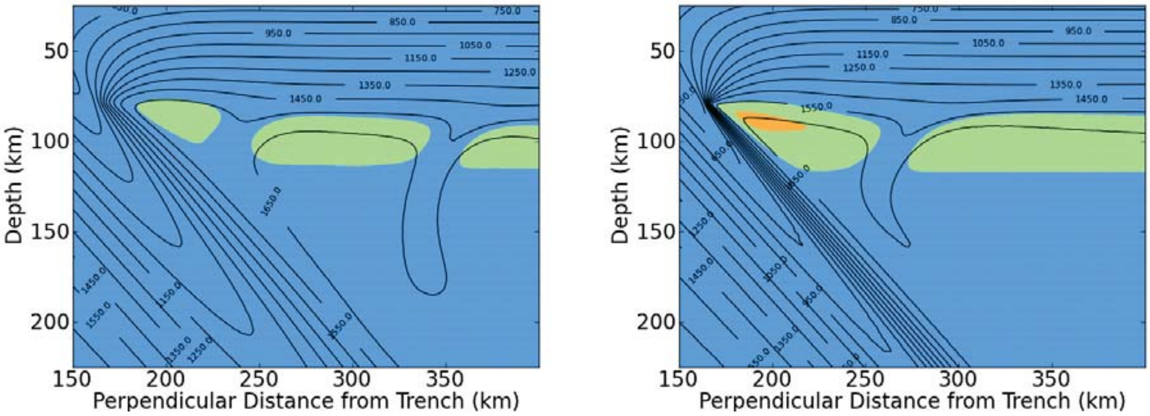

*(e)* 3000 H/$10^6$Si, 2cm/yr, t=10 m.y.

*(f)* 3000 H/$10^6$Si, 10cm/yr, t=30 m.y.

***Figure 4.15:*** *Snapshots of the thermal structure close to the wedge corner for cases with a dry, damp and wet rheology, at fast and slow subduction velocities. Regions of the wedge where pressure and temperature conditions exceed the wet and damp solidi of Katz et al. [2003], for a MORB composition, are coloured in green and orange, respectively. Snapshots are taken when the original 50 Myr old upper plate has cooled for a similar time, in both fast and slow cases.*

## 4.7 Conclusions

We have undertaken a systematic study into the dominant controls on the flow regime and thermal structure of the mantle wedge, under a range of subduction parameters, considering the influence of buoyancy and a hydrated rheology. Our results demonstrate that under a dry rheology, the flow field exhibits a corner flow pattern, where the downgoing slab drags sub-lithospheric material towards the wedge corner and, subsequently, downwards parallel to the slab surface, as found in many previous studies [e.g. Davies and Stevenson, 1992, Peacock, 1996, Peacock and Wang, 1999, van Keken et al., 2002, Kelemen et al., 2003]. However, lower viscosities, which are expected to arise under hydrated conditions ($C_{\text{OH}}$ $>=$1000 H/10$^6$Si) [Karato and Wu, 1993, Hirth and Kohlstedt, 1996], favour the development of SSC, for a wide-range of subduction configurations. Although corner flow persists, to some degree, in such cases, instabilities of variable morphologies are initiated at the base of the lithosphere. Their morphology is largely governed by the subduction velocity: in cases with low and intermediate velocities, classical Rayleigh-Taylor type instabilities, or ‘drips’, develop and propagate into the wedge core; conversely, in cases with higher subduction velocities, the instabilities take the form of ripples, which remain rooted to the base of the lithosphere whilst being advected towards the wedge corner by background mantle flow. Under very-wet ($C_{\text{OH}} = 5000$ H/10$^6$Si) and occasionally under wet ($C_{\text{OH}} = 3000$ H/10$^6$Si) conditions, the downgoing plate becomes inefficient at driving corner flow.

There are several indications that back-arcs may be wet over large distances. For example, their seismic signatures are often anomalously slow and attenuating, whilst back-arc lithosphere is regularly observed to be thin [e.g. Currie and Hyndman, 2006, Wiens et al., 2008, Hwang et al., 2011]. The link between a hydrated rheology and thin back-arcs is confirmed in our models: in wetter cases, SSC reduces lithospheric thickness, with the extent of thinning dominantly controlled by the level of hydration (viscosity) and largely insensitive to subduction velocity. We note, however, that the efficiency of lithospheric thinning is also dependent upon the length of lithosphere that is able to destabilise: if the length of potentially unstable lithosphere is less than the instability wavelength ($>$ 100–150 km for our minimum hydrated viscosities of $\sim 1 \cdot 10^{18} Pa \cdot s$), no SSC develops. Steps or strong gradients in lithospheric strength/thickness, as are observed on Earth, provide nucleation points for instabilities: under such scenarios, the tendency for SSC increases.

In cases where SSC has thinned the upper plate, wet-melting is possible beneath the back-arc. Furthermore, SSC results in transient pulses of 50–100K colder, more viscous, material being swept towards the mantle wedge corner. These affect wedge temperatures most strongly in the low-velocity cases, where drips have time to develop fully. Their anomalous temperatures are sufficient to suppress melting and affect the stability of hydrous phases within the thermal boundary layer above the downgoing plate. Different wedge viscosities influence the vigour of wedge convection, such that more hydrated wedges yield overall higher slab-surface temperatures (SSTs). However, in our models, there is no significant time-dependent effect from the drips on SSTs.

We note that with a dynamic (temperature and hydration controlled) coupling depth, corner erosion can be stronger, resulting in lower wedge-corner viscosities (due to the presence of high temperature material at lower pressures), increased instability and a stronger influence on slab-surface-temperatures [Arcay et al., 2006, 2007]. Further complexity may arise from thermo-chemical modes of flow involving low density sediments and melt-fluid mixtures, which can form small-scale, cold plumes that rise from the downgoing plate [Gerya et al., 2006, Zhu et al., 2009, Behn et al., 2011]. The interaction between thermo-chemical plumes and SSC, driven by lithospheric instability, remains to be investigated.

Our results demonstrate that hydrated wedges are unstable in 2-D. Theoretical and numerical studies [e.g. Richter, 1973, Honda et al., 2010, Wirth and Korenaga, 2012] predict that in 3-D, longitudinal, 'Richter' rolls are the dominant form of instability, and that these are enhanced with increasing subduction velocity. This implies that Earth's lithosphere may be even more unstable than we have inferred herein. The flow regimes developing in a hydrated 3-D mantle wedge, and their impacts on mantle wedge thermal structure, therefore, is the subject of the study presented in the next chapter. The insights gained through this two-dimensional investigation will aid in interpreting the three-dimensional results.

# Chapter 5

# A systematic 3-D investigation into the mantle wedge's transient flow regime and thermal structure

## 5.1 Summary

**The subduction zone mantle wedge controls the channeling of fluids towards the upper plate and into the deep mantle and, thus, plays a key role in arc volcanism, long-term volatile cycling, mineralisation and continental crust formation. The mantle wedge's flow regime is often assumed to follow a regular, corner-flow pattern. However, recent studies, which analysed the effects of a hydrated rheology and local thermal buoyancy, predict a more complex and time-dependent flow regime. In the previous chapter, we used 2-D models to demonstrate that, for a wide range of parameters, these factors lead to small-scale convection (SSC) in the wedge, and that this can significantly affect melting conditions, mineral stability fields, dehydration and upper-plate evolution. In this chapter, we explore how these effects are modified in fully 3-D numerical simulations of wedge flow. The introduction of the third dimension promotes the development of longitudinal Richter rolls of SSC, with axes aligned perpendicular to the trench. We observe two separate, but interacting, SSC systems, each with a distinct wavelength and time-scale: (i) an arc system, with a characteristic wavelength of 50-200 km, that varies on a few Myr time scale; and (ii) a back-arc system, with a characteristic wavelength of 100-400 km, which varies on a 3-10 Myr time scale. The arc rolls have similar trench-parallel and trench-perpendicular dimensions, whilst back-arc instabilities coalesce into elongated sheets, which are preferentially**

**aligned in a trench perpendicular direction. Although the alignment of back-arc sheets is more prominent at increased subduction velocities, the sheets themselves are best defined at intermediate subduction velocities of 5 cm yr$^{-1}$: at higher velocities, drips are sheared by background corner flow, before they can fully coalesce into sheets, thus reducing their vertical extent. The degree of interaction between both systems increases with increased levels of wedge hydration and increased subduction velocities, with SSC suppressed when viscosities exceed $5 \cdot 10^{18}$ Pa s. Along strike averages of wedge velocities and temperatures are consistent with those predicted in 2-D. However, lithospheric erosion is stronger in 3-D, which expands the regions where melting is possible and shifts dehydration boundaries. Furthermore, the Richter rolls produce significant trench parallel variability, with sub-arc temperatures varying by up to 150K along strike. Such lateral temperature anomalies are stronger than those predicted in 2-D, further increasing regions where hydrous melting is possible below the arc and back-arc.**

## 5.2 Introduction

The majority of Earth's seismicity and volcanism occurs at destructive plate margins. These locations accommodate substantial cycling of volatiles and other elements, which are carried to depth by subducting plates. Below the overriding plate, viscous drag exerted by the subducting slab forces mantle to flow in from the back-arc region towards the wedge corner where down-going and upper plates meet. The high temperatures thus reached in the wedge corner lead to dehydration of minerals in the downgoing slab, delivering water to the neighbouring mantle and facilitating melt formation and magmatism.

Computational models which simulate the mantle wedge's flow regime and thermal structure aim to reproduce these mechanisms to help understand what controls the location and style of arc volcanism and the observed variability between different subduction zones. Most previous studies have focussed on 2-D wedge flow kinematically driven by the subducting plate, and have often neglected the role of buoyancy and wedge hydration. Models where wedge flow is purely kinematically driven yield temperatures which agree with many observations [e.g. Syracuse et al., 2010, Kneller et al., 2007, Long and Becker, 2010, Hebert and Gurnis, 2010, Plank et al., 2009], but cannot explain complex wedge seismic structure, temporal-variability in arc volcanism, or the thin lithosphere and high heat flow observed in many back-arc regions [e.g. Tamura et al., 2002, Schurr et al., 2003, Currie and Hyndman, 2006]. Under hydrous conditions, mantle viscosities are likely substantially lower than those of dry mantle [Karato and Wu, 1993, Hirth and Kohlstedt, 1996], leading to small-scale convection (SSC) that is driven by gravitational instabilities from the based of the overriding plate [e.g. Honda and Saito, 2003]. Although a recent study has challenged the rheological influence of water in the wedge [Bali et al., 2013], seismic anomalies that show low-velocity and high-attenuation and back-arc surface topography are most easily explained with a low-viscosity subduction mantle wedge[Billen and Gurnis, 2001, Currie and Hyndman, 2006, Wiens et al., 2008, Jadamec and Billen, 2010].

In Chapter 4, we systematically examined the effect of a number of parameters on the mantle wedge's flow regime and thermal structure, when accounting for the effects of both buoyancy and a hydrated rheology. We found SSC to be a common occurrence under hydrated conditions. When low mantle viscosities, below $5 \cdot 10^{18}$ Pa s, extended over lateral distances greater than 100 km (thus exceeding instability wavelengths), SSC led to strong lithospheric erosion, and a 50-100K variability in wedge temperatures, which is sufficient to affect where melting and dehydration can occur. While the net back-arc lithospheric erosion was largest when slab velocities were highest, drips were most pronounced when subducting plate velocities and, thereby, shearing of the drips by corner-flow, were lowest.

As in other kinematically driven wedge models, additional lithospheric thinning occurred in the sub-arc region (i.e. in the wedge corner, immediately adjacent to the fore-arc nose, where the slab reaches 80-160 km depth — although our models do not predict arc locations, this is the slab-depth range that corresponds to volcanic-arc locations [e.g. England et al., 2004]). Here, dislocation-creep enhanced strain-rates in the wedge corner promote the development of a 'pinch zone'. The size of this zone is affected by the implementation of the decoupled slab/upper-plate interface [e.g. Conder and Wiens, 2007, Arcay et al., 2008], which needs to extend to $\sim 80$ km depth to satisfy observations of low surface heat flow and low seismic attenuation in the fore-arc region [Wada and Wang, 2009, Syracuse et al., 2010]. The differential thinning between back-arc and arc is most pronounced in models with the highest viscosities and highest subduction velocities. In our 2-D models, we found that instabilities sometimes nucleated along the high gradient in lithospheric thickness between back-arc and arc, but usually did not propagate efficiently into the arc region, because of its narrow size relative to instability wavelengths.

It is well established that SSC from a sheared plate has a tendency to preferentially form longitudinal rolls (i.e. with their axes aligned perpendicular to the trench) rather than the transverse rolls (with axes aligned parallel to the trench) that can be modelled in 2-D [e.g. Korenaga and Korenaga, 2008]. These structures, which are termed "Richter" rolls [Richter, 1973], have been shown to facilitate the initiation of SSC and to produce significant complexity in fully 3-D models of a sheared oceanic plate [van Hunen et al., 2003]. In a recent study that used the 3-D single mode approximation, Wirth and Korenaga [2012] predict that significant SSC, with temperature fluctuations of 100-150 K and wavelengths of 100-200 km, should occur in the mantle wedge where viscosities are around $1 \cdot 10^{18}$ Pa s or less. Honda and coworkers [e.g. Honda and Saito, 2003, Honda and Yoshida, 2005, Honda, 2008, Honda et al., 2010] studied wedge flow patterns in 2-D and 3-D, for cases where only a $\sim$100 km wide section of the sub-arc region was hydrated. For viscosities on the order of $10^{18}$ Pa s, they observed a time-dependent pattern of SSC, in which longitudinal rolls interchanged their up and down limbs approximately every 2 Myr. They noted that this frequency is comparable to that of episodes of volcanism in Central Honshu, at arc locations that differ by around 50 km, similar to half a roll wavelength in their models.

In this chapter, we present the first systematic fully 3-D study of SSC in the subduction zone mantle wedge, for a range of subduction velocities, (dry to hydrous) mantle viscosities and upper-plate ages. We first introduce the 3-D model setup, which is intentionally simple in order to focus solely on the impact of the addition of the third dimension to the 2-D system analysed in chapter 4 (section 5.3). We subsequently describe the observed 3-D SSC flow styles, and how they vary with the different parameters (section 5.4). In Section 5.5, we show that, when compared to previous findings from 2-D models, the different style and vigour of the 3-D SSC more readily produces conditions that allow dehydration and melting.

## 5.3 3-D Model Setup

To compare with the 2-D results from chapter 4, we use a comparable model setup and the same parameters. Prescribed slab velocities drive fully-dynamic flow in the mantle wedge beneath an overriding plate, which is able to destabilise. We solve the Stokes and energy equations, assuming an incompressible, Bousinessq formulation, using the Fluidity computational framework [Davies et al., 2011, Kramer et al., 2012]. The solution strategies employed are identical to those of the 2-D study: they are outlined (and validated for problems of this nature) in chapter 3, and explained in more detail in Davies et al. [2011].

### 5.3.1 Geometry, Boundary & Initial Conditions

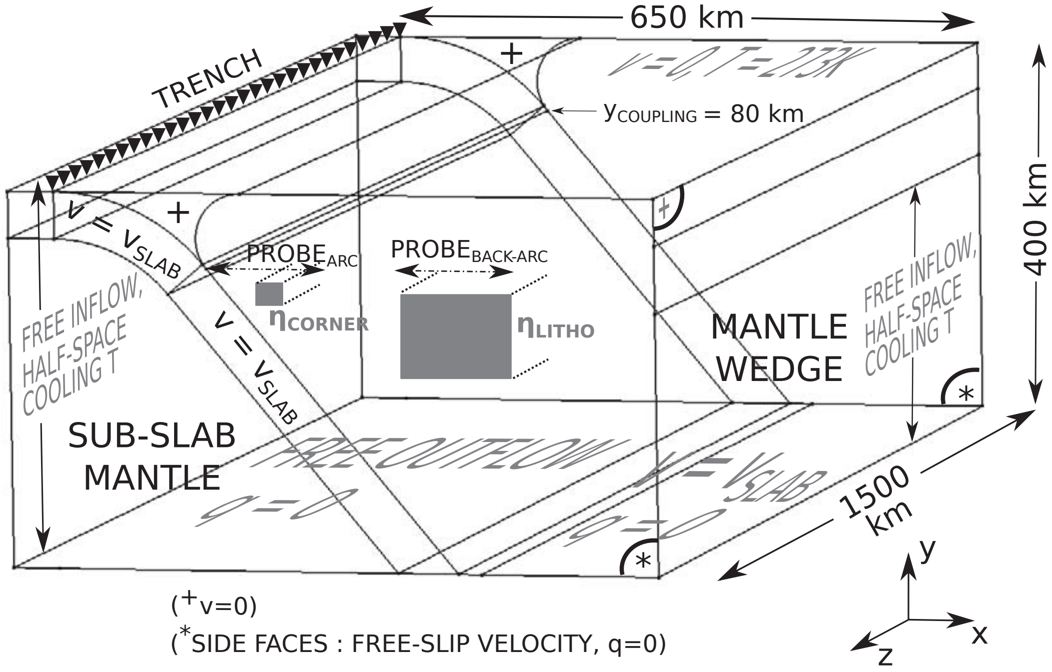

***Figure 5.1:*** *Model set–up to simulate 3-D mantle–wedge dynamics: the domain is 400-km deep, 700-km wide in the transverse (x-)direction, and 1500-km wide in the longitudinal (z-)direction. It is divided into 4 regions: (i) the prescribed downgoing plate, where* $V = V_{SLAB}$*; (ii) a prescribed rigid forearc corner, where* $V = 0$*; and (iii) a mantle wedge and (iv) a sub-slab mantle where flow is solved. Temperature is solved throughout the computational domain. The subducting slab curves to a constant dip angle of* 50° *at 75-km depth, and is fully coupled to wedge flow below 80-km depth. Velocities are fixed along the top and side of the overriding plate, prescribed to slab velocity at the bottom of the wedge, and free along other boundaries. Temperature boundary conditions follow a half-space cooling relationship everywhere, except at the model's base and front and back, where a zero heat flux boundary condition,* $q = \frac{dT}{dn} = 0$*, is enforced. The grey parallelepipeds (marked* $\eta_{CORNER}$ *and* $\eta_{LITHO}$*)) represent areas where wedge corner and sub-lithospheric viscosities are analysed (Section 5.4.3). The average depth of the 1400K isotherm, which is used as a proxy for sub-arc and sub-back-arc lithospheric thicknesses in Section 5.5.1, is measured along the horizontal lengths spanned by the black dotted double-pointed arrows (labelled* $PROBE_{ARC}$ *and* $PROBE_{BACK-ARC}$*). In order to minimise edge effects, these measures are longitudinally averaged along the central 1200km of the domain only.*

Our model setup is illustrated in Fig. 5.1. In 2-D, we examined the effect of different slab dips, whereas in 3-D, we concentrate on the 50° dip case, in a computational domain that is 400 km deep (y-direction) and 700 km wide in the trench-perpendicular (x-) direction. For the 3-D configuration, the domain is extended 1500 km in the longitudinal (z-)direction. The subducting plate spans the full 1500-km width of the domain. Mesh resolution varies from a minimum of 2 km at the wedge corner, to a maximum of 8 km at the base of the domain. 3-D sensitivity tests showed that for a minimum element size of $\leqslant$ 2 km along the trench-parallel edge of the wedge corner, 3-D wedge dynamics are the same.

Velocities are prescribed to be horizontal in the down-going plate for 50 km prior to subduction, and then follow a down-dipping circular arc to a depth of 75 km, below which they dip at a constant angle. The overriding plate is not fully fixed or rigid: it is free to evolve self-consistently in response to the local thermal structure and flow-field [e.g. Kelemen et al., 2003], aside from: (i) at its surface, where we impose a no-slip boundary condition; and (ii) in a curved prism-shaped region above the subducting plate, where velocities are fixed to zero to a depth of 80 km. Below this depth, the subducting slab and mantle wedge are fully coupled, in a manner consistent with the *D80* model of Syracuse et al. [2010]. Vertical surfaces below the incoming and upper plate at $x = x_{\text{min}}$ and $x = x_{\text{max}}$ are stress-free. At the side of the the overriding plate, at $x = x_{\text{max}}$, a no-normal flow boundary condition is enforced down to a depth where temperature reaches a nominal value of 99% of mantle temperature. At the domain's lowermost boundary, we prescribe an outflow boundary condition equal to the subduction velocity on the wedge side of the slab and a stress-free boundary condition for the sub-slab basal surface. Free-slip boundary conditions are specified at the domain's front and back faces ($z = 0, z_{\text{max}}$).

The thermal boundary conditions comprise: a surface temperature, $T_s$, fixed to 273K and zero heat-flux conditions on the bottom as well as on the domain's front and back faces ($z = 0, z_{\text{max}}$). On the $x = 0$ and $x = x_{\text{max}}$ sides, temperatures are fixed to an error function:

$$T(x = 0, y) = T_s + (T_0 - T_s)\text{erf}(\frac{y}{2\sqrt{\kappa t_{\text{plate}}}}). \tag{5.1}$$

Here $T_0$ is the reference mantle temperature (fixed at 1623K), $t_{\text{plate}}$ is either the subducting slab age, $t_{\text{subd}}$, or the overriding plate age, $t_{\text{upper}}$, and $\kappa$ is thermal diffusivity. Eq. 5.1 is also utilised in defining model initial conditions, where for all cases, $t_{\text{plate}} = t_{\text{subd}}$ on the down-going plate side of the trench, and $t_{\text{plate}} = t_{\text{upper}}$ on the upper-plate side of the trench. Models are then initialised until the thermal signature of the downgoing plate has advected to the base of the domain. We refer to the time when the slab reaches 400 km depth as $t = 0$. After a further $\approx 5$ Myr, 3-D wedge flow patterns stabilise into a single mode, although they do evolve further as the overriding plate thickens conductively. We analyse our results in the $t = 5 - 100$ Myr time window.

| Quantity | Symbol | Reference value |
|---|---|---|
| Gravity | $g$ | $9.81 m \cdot s^{-2}$ |
| Reference Density | $\rho_0$ | $3300 kg \cdot m^{-3}$ |
| Mantle Temperature | $T$ | $T_0 = 1623K = 1350°C$ |
| Surface Temperature | $T_s$ | $T_s = 273K = 0°C$ |
| Thermal conductivity | $k$ | $3.1 W \cdot m^{-1} \cdot K^{-1}$ |
| Specific heat capacity (constant pressure) | $c_p$ | $1250 J \cdot kg^{-1} \cdot K^{-1}$ |
| Thermal diffusivity | $\overline{\overline{\kappa}}$ | $0.75 \cdot 10^{-6}\ \mathrm{m^2 s^{-1}}$ |
| Thermal expansivity | $\alpha$ | $2.5 \cdot 10^{-4} K^{-1}$ |
| Activation energy - dry diff. creep | $E_{\text{diff,d}}$ | $375 kJ \cdot mol^{-1}$ |
| Activation energy - dry disl. creep | $E_{\text{disl,d}}$ | $530 kJ \cdot mol^{-1}$ |
| Activation energy - hyd. diff. creep | $E_{\text{diff,h}}$ | $335 kJ \cdot mol^{-1}$ |
| Activation energy - hyd. disl. creep | $E_{\text{disl,h}}$ | $480 kJ \cdot mol^{-1}$ |
| Activation volume - dry diff. creep | $V_{\text{diff,d}}$ | $6 \cdot 10^{-6}\ kJ \cdot mol^{-1}$ |
| Activation volume - dry disl. creep | $V_{\text{disl,d}}$ | $20 \cdot 10^{-6}\ kJ \cdot mol^{-1}$ |
| Activation volume - hyd. diff. creep | $V_{\text{diff,h}}$ | $4 \cdot 10^{-5}\ m^3 \cdot mol^{-1}$ |
| Activation volume - hyd. disl. creep | $V_{\text{disl,h}}$ | $11 \cdot 10^{-5}\ m^3 \cdot mol^{-1}$ |
| Power-law exponent | $n$ | $3.5$ |
| Maximum viscosity | $\eta_{\text{max}}$ | $10^{24} Pa \cdot s$ |
| Reference grain size | $g_0$ | $10 mm$ |
| Universal gas constant | $R$ | $8.3145 J \cdot mol^{-1} \cdot K^{-1}$ |
| Water Content - damp mantle | $C_{\text{OH,damp}}$ | $1000\ \mathrm{H}/10^6\mathrm{Si}$ |
| Water Content - very-wet mantle | $C_{\text{OH,v.wet}}$ | $5000\ \mathrm{H}/10^6\mathrm{Si}$ |
| Water content exponent | $r$ | $1.2$ |
| Pre-exponential constant - dry diff. creep | $A_{\text{d}}$ | $10^{8.82} Pa \cdot s$ |
| Pre-exponential constant - dry disl. creep | $B_{\text{d}}$ | $10^{\frac{-11.04}{n}} Pa \cdot s^{\frac{1}{n}}$ |
| Pre-exponential constant - hydrated diff. creep | $A_{\text{h,0}}$ | $10^{12} Pa \cdot s {\frac{H}{10^6 Si}}^{\frac{r}{n}}$ |
| Pre-exponential constant - hydrated disl. creep | $B_{\text{h,0}}$ | $10^{(6+\frac{1.95}{n})} Pa \cdot s^{\frac{1}{n}} \cdot {\frac{H}{10^6 Si}}^{\frac{r}{n}}$ |

***Table 5.1:*** *Nomenclature and reference values for 3-D model parameters used in this chapter.*

### 5.3.2 Material Properties

Material properties are summarised in Table 5.1. Standard values are used for equation of state parameters, and these do not vary spatially. For viscosity, a composite diffusion and dislocation creep rheology is utilised, which is identical to that used for our 2-D models. For completeness, and because rheology strongly controls the results, we present the equations here again:

$$\eta_{\text{diff,x}}(T) = A_{\text{x}} \exp\Big(\frac{E_{\text{diff,x}} + (PV_{\text{diff,x}})}{RT}\Big), \tag{5.2}$$

$$\eta_{\text{disl,x}}(T, \overline{\overline{\dot{\varepsilon}}}) = B_{\text{x}} \exp\Big(\frac{E_{\text{disl,x}} + (PV_{\text{disl,x}})}{nRT}\Big) \overline{\overline{\dot{\varepsilon}}}^{\frac{(1-n)}{n}}, \tag{5.3}$$

where the subscript x is d for dry cases, and h for those where hydration is introduced. Subscripts diff and disl denote diffusion creep and dislocation creep. The exponent $n$ in the power-law relationship between viscosity, $\eta_{\text{disl}}$, and the second-invariant of the strain-rate tensor, $\overline{\overline{\dot{\varepsilon}}}$, accounts for the effects of stress dependence under dislocation creep. $T$ and $P$ represent absolute temperature (for which an adiabatic gradient of 0.5 K/km is added to our Boussinesq potential temperature solution) and lithostatic pressure ($P = \rho_0 g h$, where $h$ is depth), respectively. $R$ is the universal gas constant. The activation energies ($E_{\mathrm{diff}}$, $E_{\mathrm{disl}}$) and volumes ($V_{\mathrm{diff}}$ and $V_{\mathrm{disl}}$) are taken from Hirth and Kohlstedt [2003]. Together with the other parameter values, these are listed in Table 5.1. The pre factors for dry rheology, $A_{\mathrm{d}}$ and $B_{\mathrm{d}}$, are constants, while those for hydrated rheologies include a water content term:

$$
\begin{aligned}
A_{\mathrm{h}} &= A_{\mathrm{h},0}\, C_{\mathrm{OH}}, && (5.4)\\
B_{\mathrm{h}} &= B_{\mathrm{h},0}\, (C_{\mathrm{OH}}^{-r})^{\frac{1}{n}}. && (5.5)
\end{aligned}
$$

Here, $C_{\mathrm{OH}}$ and $r$ represent the water content and water content exponent [Hirth and Kohlstedt, 2003]. Note that hydrated parameters are used for all but the dry cases. We do not include a stress-limiting rheology, but, instead, truncate viscosity at a fixed maximum $\eta_{\mathrm{max}}$ of $10^{24}$Pa, yielding effective diffusion and dislocation creep viscosities $\eta_{\mathrm{diff,eff.}}$ and $\eta_{\mathrm{disl,eff.}}$ as follows:

$$
\begin{aligned}
\eta_{\mathrm{diff,eff.}} &= \Big(\frac{1}{\eta_{\mathrm{diff}}} + \frac{1}{\eta_{\mathrm{max}}}\Big)^{-1}, && (5.6a)\\
\eta_{\mathrm{disl,eff.}} &= \Big(\frac{1}{\eta_{\mathrm{disl}}} + \frac{1}{\eta_{\mathrm{max}}}\Big)^{-1}. && (5.6b)
\end{aligned}
$$

Diffusion and dislocation creep laws are subsequently combined via a harmonic mean, to obtain a composite creep viscosity that is given by:

$$
\eta_{\mathrm{comp}} = \Big(\frac{1}{\eta_{\mathrm{diff,eff.}}} + \frac{1}{\eta_{\mathrm{disl,eff.}}}\Big)^{-1}. \qquad (5.7)
$$

### 5.3.3 Model Cases

To unravel the dominant controls on the mantle wedge's 3-D flow-regime and thermal structure, we examine a suite of simulations, where we systematically vary a range of subduction

| $\tau_{\text{upper}}$ (Myr) | $v_{\text{slab}}$ (cm/yr) | $C_{\text{OH}}$ (H/$10^6$Si) | log($\eta_{\text{CORNER}}$) log($Pa \cdot s$) | log($\eta_{\text{LITHO}}$) log($Pa \cdot s$) | Back-arc Stability | Arc Stability |
|---|---|---|---|---|---|---|
| 120 | 2 | 5000 | 18.40 | 18.28 | Drips, weak Ridges, Rolls | Small Rolls |
| 120 | 5 | 0 | 19.74 | 20.31 | *Corner-flow* | No Rolls |
| 120 | 5 | 1000 | 18.70 | 19.22 | Weak Ridges, Large Rolls | Large Rolls |
| 120 | 5 | 5000 | 18.09 | 18.21 | Strong Ridges, Rolls | Small Rolls |
| 120 | 10 | 5000 | 18.02 | 18.29 | Strong, sheared Drips and Ridges, Rolls | Small Rolls |
| 50 | 5 | 0 | 19.59 | 20.13 | *Corner-flow* | No Rolls |
| 50 | 5 | 1000 | 18.61 | 18.88 | Tends towards dripping | No Rolls |
| 50 | 5 | 5000 | 18.01 | 18.20 | Drips and Ridges, Rolls | Small Rolls |

***Table 5.2:*** *Summary of models presented herein. For each, upper plate age $\tau_{upper}$, slab velocity $\mathrm{v}_{slab}$, wedge water content $\mathrm{C}_{OH}$, wedge corner and sub-lithospheric viscosities $\eta_{\text{ARC}}$ and $\eta_{\text{BACKARC}}$ as measured in the grey parallelepipeds on Fig. 5.1, and accounts on sub-back-arc and sub-arc stability are given.*

parameters. To examine the role of viscosity, we vary wedge hydration between dry, ‘damp’ ($C_{\text{OH}} = 1000$ H/$10^6$Si – representative of sub-ridge mantle [Hirth and Kohlstedt, 1996]) and ‘very-wet’ ($C_{\text{OH}} = 5000$ H/$10^6$Si - as an end-member subduction zone hydration case [e.g. Karato, 2003, Katz et al., 2003]). In 2-D, we found that ’wet’ cases, with $C_{\text{OH}} = 3000$ H/$10^6$Si, displayed very similar behaviour, including time, spatial and temperature scales, as very-wet models, and hence wet cases will not be examined here. In all cases, hydration is assumed to be constant throughout the wedge. We also vary the subduction velocity, over a representative range (2, 5 and 10 cm yr$^{-1}$) [e.g. Lallemand et al., 2005, Seton et al., 2012]. For the overriding plate, we consider relatively young (50 Myr) and old (120 Myr) cases. The age of the downgoing plate is always 50 Myr at the trench, as we found in 2-D that subducting plate age had a negligible influence on wedge structure and dynamics (see also Wirth and Korenaga [2012]).

The remainder of this chapter is structured as follows: in Section 5.4, we focus on the observed styles of 3-D wedge flow, which show important differences from those predicted in 2-D. We quantify how wedge-flow style varies in response to different subduction velocities (Section 5.4.2), levels of wedge hydration (Section 5.4.3) and upper plate ages (Section 5.4.4). In Section 5.5, we discuss the consequences of these different flow regimes for upper plate lithospheric thickness, the wedge’s thermal structure and slab surface temperatures, with further discussion of the results and conclusions in Section 5.6.

## 5.4 3D SSC Styles & Controls

In our 2-D models, we observed three distinct flow regimes across the parameter space examined:

1. Corner-flow: classical wedge flow which occurs at high mantle viscosities and is facilitated by faster subduction velocities.

2. Small-scale convection (SSC): the unstable mode of convection obtained for values of wedge viscosity lower than $5 \cdot 10^{18}$ Pa s, which is characterized by the formation of sub-lithospheric instabilities.

3. Decoupled flow: occurs when the slab is inefficient at driving wedge flow (under slow subduction or due to very low mantle viscosity). In the set-up of our models this mode leads to the development of a strong convective cell on the vertical side of the wedge. On Earth, the style of flow would be determined by other sources of buoyancy.

We found that SSC was observed for most cases that included some hydration and was occasionally aided by steps in lithospheric thickness or viscosity. We next examine the styles of flow observed in 3-D models.

### 5.4.1 Richter Roll Style

In 3-D, columnar drips can align and coalesce into downwelling ridge-like structures, forming instabilities that are termed ‘Longitudinal Richter Rolls’ [Richter, 1973] (Fig. 5.2). These rolls have their axes aligned perpendicular to the trench, which differs to the instabilities observed in 2-D, where such an alignment is not possible (the instabilities observed in 2-D, with their axes aligned parallel to the trench, are termed ‘Transverse Richter Rolls’). Snapshots of the wedge structure for a very-wet, 120 Myr upper plate case with a subduction velocity of 10 cm $yr^{-1}$ in Fig. 5.2, show that signatures of the lithospheric drips are still visible on the ridges that form as they get aligned in a trench-perpendicular direction by background wedge corner flow.

Before discussing how different parameters affect these rolls, we present the general characteristics of this type of 3-D SSC, which are best illustrated in a very-wet 120 Myr old upper-plate case. Most notably, as shown in Fig. 5.3, two systems of rolls form within the wedge. The first occurs below the ‘arc’ region (i.e. the region above the subducting slab at a distance of 175-275 km from our trench, where the slab reaches the depth range above which on Earth volcanic arc-systems are observed at the surface). The second system forms below the back-arc region (i.e. distances > 275 km from the trench).

Below the arc region, cross-sections at 100 km depth illustrate that a set of rolls of similar transverse (x) and longitudinal (z) dimensions is formed. These are clearly visible in both the temperature (Fig. 5.3a) and velocity (Fig. 5.3b/c) fields: arc Richter-rolls exhibit a regular pattern of alternating high and low temperatures (variations of 100–150 K) and positive and

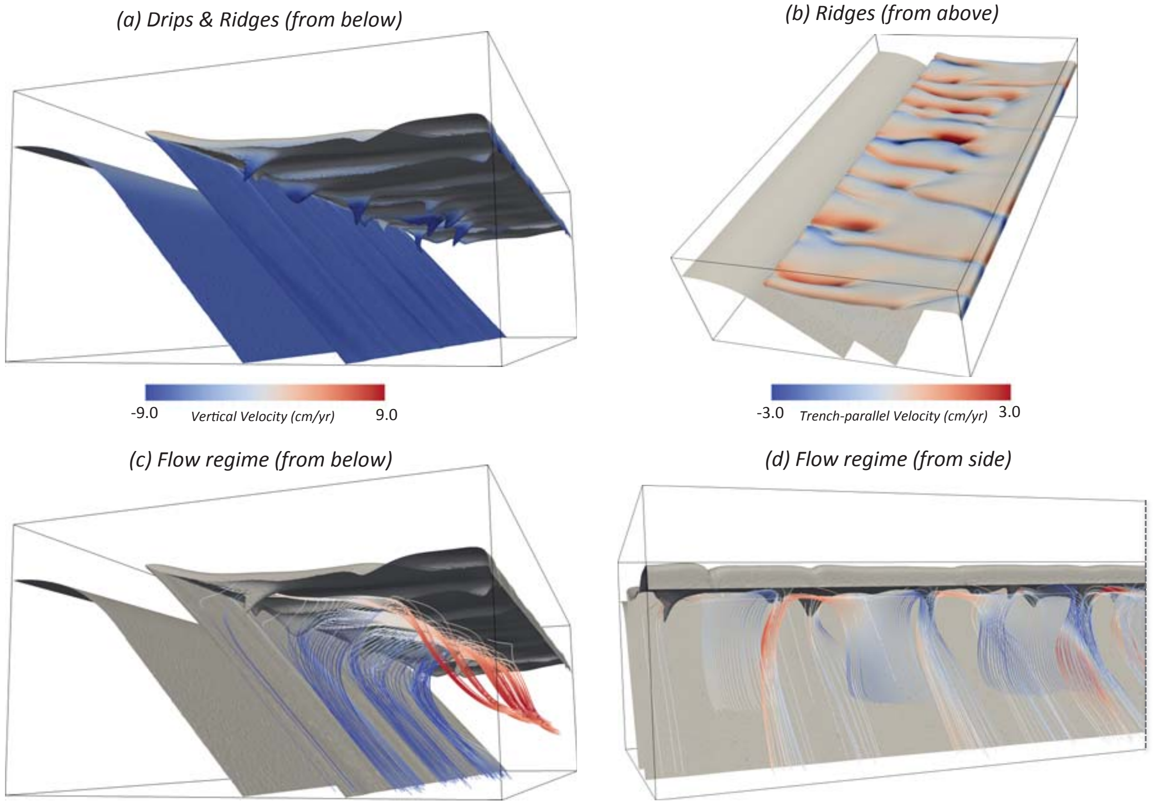

**Figure 5.2:** *An illustration of 3-D small-scale-convection, for a case with a very-wet ($C_{OH}$ =5000 H/$10^6$Si) rheology, a subduction velocity of 10cm/yr and a 120 Myr old upper plate, at a simulation time of 40 Myr. Full model box of 1500 km long by 650 km wide and 400 km deep is shown. In panel (a), which is viewed from below the mantle wedge, the 1550 K temperature isosurface, coloured by vertical velocity, illustrates a series of cold 'ridges' that are principally aligned in the trench-perpendicular direction. Transient 'drips', which sometimes extend into the wedge core, can be seen propagating along these ridges, towards the wedge corner. Ridges mark the downwelling limbs of longitudinal Richter rolls, the influence of which can also be seen at the slab surface, where the 1550 K isosurface protrudes further into the wedge; (b) the 1550 K isosurface, viewed from above, which is coloured by trench-parallel velocity, providing an alternative illustration of the longitudinal Richter rolls. In the example shown, ridges are strongly aligned and extend from the wedge corner to the edge of the domain, often branching or merging; (c/d) an illustration of the mantle wedge's flow regime, from two different directions – images include the 1550 K isosurface (coloured in grey) and stream-tracers, which are coloured by (c) vertical velocity and (d) trench-parallel velocity. The example shown has a high subduction velocity and, hence, the stream-tracers shown a clear corner-flow pattern (c). Nonetheless, due to the Richter rolls and the transient drips, material can descend into the wedge core, without reaching the wedge corner. Furthermore, although corner-flow persists, there is a significant trench-parallel flow component, with material pulled towards the downwelling ridges from both directions, as illustrated in both panels (b) and (d).*

negative vertical and longitudinal velocities, at distances between 200-250 km from the trench. These arc rolls are specific to the 3-D system. In 2-D models, the arc corner, which is a natural consequence of the enhanced thinning ('pinching') of the upper plate by strain-rate weakening in the wedge corner, is too narrow to permit the development of coherent instabilities (instability wavelengths exceeds the space available and, accordingly, are unable to form). However, in 3-D, the third dimension provides the space necessary, and rolls develop with wavelengths of $\sim 50 - 200$km. These temperature variations and wavelengths are similar to those predicted by the single-mode approximation of Wirth and Korenaga [2012].

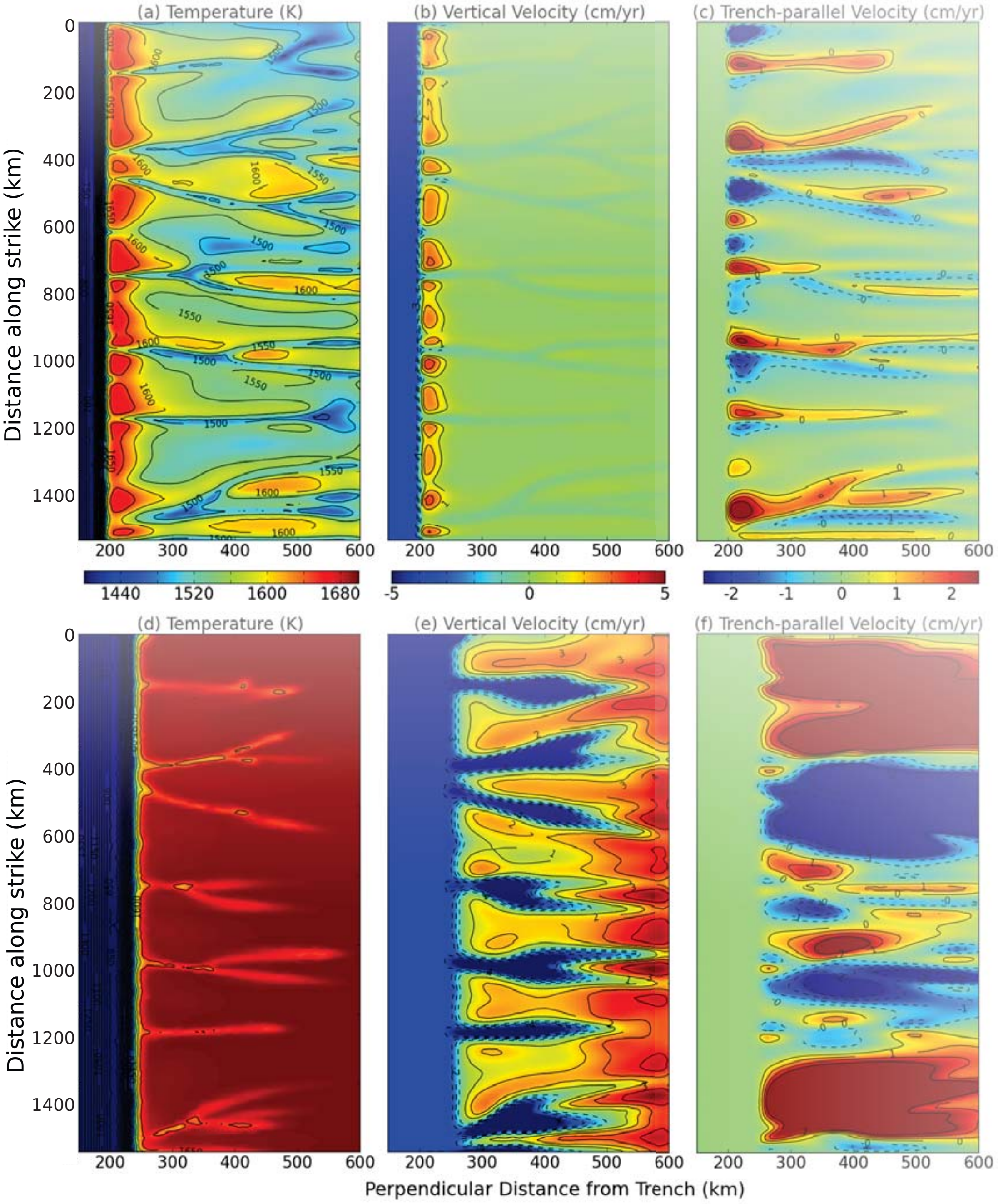

*__Figure 5.3:__ Temperature, vertical (Vy) and longitudinal (Vz) velocity at 100 km (a-c) and 150 km (d-f) depth, for a case with an intermediate slab velocity of 5 cm yr$^{-1}$, old upper plate of 120 Myr, and very wet mantle rheology with water content of 5000 H/10$^6$Si. Vy is positive upward, Vz negative in the direction of the trench strike. Note the distinct, but interacting systems that develop below the arc (100 km depth) and back-arc (150-km depth).*

The morphology of back-arc instabilities differs to those observed below the arc region, as illustrated by cross-sections at 150 km depth (Fig. 5.3d-f): elongated low-temperature ridges are observed, which are 50-150 K cooler than surrounding material, with clear drips along some ridges. Spacing between the ridges is between 100 and 400 km, and they extend in the trench perpendicular direction for 200 to 400 km, some to the edge of the domain. Some of the ridges branch or merge, an expression of the time-dependence of the flow, where different drips may link up at different times to form sheets. The larger wavelength of the back-arc rolls is a consequence of the higher viscosities there than in the arc region (see Section 5.4.3).

The two roll systems interact. The back-arc instabilities partially modulate the location of arc instabilities, imparting a longer wavelength on the arc rolls and enhancing arc downwellings where the back-arc ridges extend into the wedge corner. This interaction is further illustrated in Fig. 5.4, where we display temporal snapshots of the model at 3 Myr intervals. The location and expression of instabilities, both beneath the arc and the back-arc, is strongly time-dependent. The arc-system is generally more time-dependent (as would be expected due to the reduced viscosities in this region), with individual rolls merging and splitting on a few Myr time scale, in addition to migrating in a trench parallel direction. As a consequence, the number of arc Richter-rolls varies between 15 and 20 over time (Fig. 5.4a-d). In the back-arc system, instabilities coalesce into larger-scale ridges and also show some trench parallel migration over time. Branch-like structures are evolving over 3-10 Myr time scales: most ridges are aligned perpendicular or sub-perpendicular to the trench, although some are sub-parallel for shorter time intervals (Fig. 5.4e-h).

As in our 2-D models, the morphology, wavelength and temporal evolution of instabilities varies across the parameter space examined. Table 5.2 summarises the different styles we find in 3-D, with the controls on these styles discussed in the following sections.

### 5.4.2 Influence of Subduction Velocity

To evaluate the effect of subduction velocity on mantle wedge's flow regime, Fig. 5.5 shows horizontal cross sections that highlight the arc and back-arc systems for a slower (2 cm yr$^{-1}$) and faster (10 cm yr$^{-1}$) case than the intermediate velocity case (5 cm yr$^{-1}$) discussed in the previous section (which is shown in Figs. 5.3 and 5.4). The first panels of Fig. 5.4 (at 20 Myr) and the panels of Fig. 5.5 are displayed at model times that correspond to the same upper-plate cooling time (and, hence, instabilities have the same time to develop). Because slower plates take longer to reach the base of the model, we display results for the slowest model at an earlier time (15 Myr) than for the faster models (35 Myr).

Similar to what we found in 2-D, subduction velocities do not control whether SSC does or does not occur, but velocities do affect the style of SSC. In general, increased subduction velocities lead to more prominent back-arc ridges, with a stronger trench perpendicular alignment,

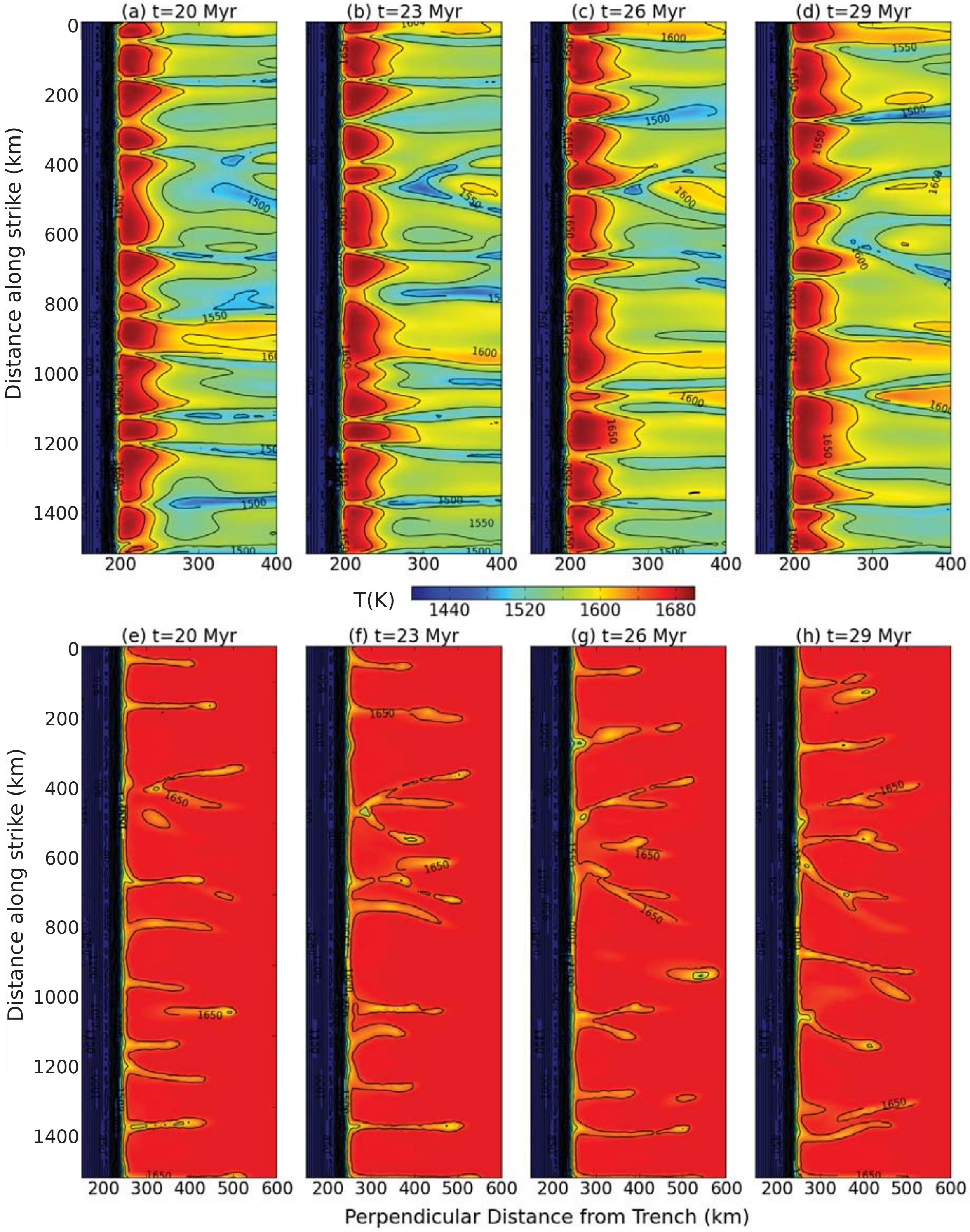

***Figure 5.4:*** *Temperature slices for very-wet, 5 cm yr$^{-1}$, 120 Myr upper plate case at 100 km depth (top four panels) illustrate on what time-scales the arc cells merge and split; while those at 150-km depth (bottom four panels) show the migration and coalescence of back-arc ridges. Note that the sections at 100 km depth have a horizontal scale that is half that of those at 150 km, to see better illustrate the behaviour of the smaller-scale arc system.*

when compared to cases with a smaller subduction velocity (Fig. 5.5). The horizontal extent of back-arc ridges also increases with increased subduction velocity, with ridges extending

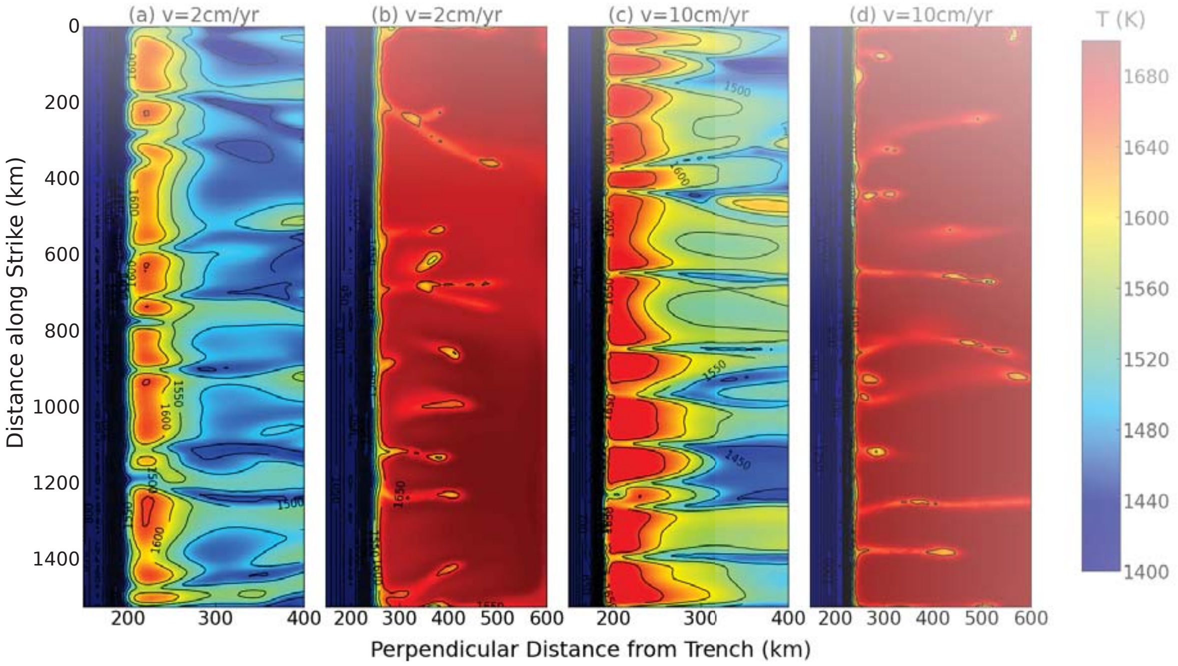

***Figure 5.5:*** *Horizontal temperature slices at 100 km and 150 km depths, for very-wet (5000 H/10$^6$Si) cases, with old (120 Myr) upper plate, under (a-b) 2 cm yr$^{-1}$, slow, and (c-d) 10 cm yr$^{-1}$, fast, subduction. The time slices chosen correspond to the same upper-plate cooling time for the different velocity cases (15 Myr in a-b, 35 Myr in c-d). Note that the corresponding intermediate velocity case (at 20 Myr) is shown in Fig. 5.4.*

from the wedge corner to the boundary of the domain only in the fastest subduction velocity cases. In addition, the faster subduction velocity cases lead to a temporally more stable system: back-arc ridges migrate and interact less when subduction velocities are high, and they exert a stronger influence on the arc system.

However, contrary to theoretical prediction [Richter, 1973], we do not observe a simple increase in the strength of Richter rolls with increasing plate velocity. Instead, the thermal signature of the ridges is most pronounced for the intermediate velocity case (cf. the 1650 K isotherm at 150 km depth in Fig. 5.4e and Fig. 5.5b/d). This can be understood from the 2-D models, where we found that drips have more time to grow in cases of low subduction velocities, while at higher velocities the drips get sheared before fully developing. However, at low velocity, the horizontal velocity of incoming mantle flow is insufficient for the drips to align and coalesce into 3-D ridges, while at faster velocities, they are sheared into prominent sheets due to increased corner flow. Thus, the competition between the time available for drip growth and velocity-controlled strength of shearing leads to ridges being coolest at 150 km in the intermediate velocity case.

For all subduction velocity cases (i.e. 2, 5, 10 cm yr$^{-1}$) sub-arc Richter rolls form with similar wavelengths of 50-150 km (cf. Figs. 5.4a and 5.5a,c). However, with increasing subduction velocity, the modulating influence of back-arc ridges on the arc system becomes more prominent, superimposing a second, longer wavelength of 150-km to 400-km on the arc system (Fig. 5.5c). These more pronounced downwellings then leave stronger signatures in the thermal structure of the wedge corner. As the simulation evolves and the old lithosphere thickens further, the back-arc wavelength becomes increasingly dominant below the arc.

Further insights into the effect of subducting slab velocity on the flow regime beneath the arc can be gained by analysing mantle velocities at 100 km depth (Fig. 5.6). Velocities are scaled to the subduction velocity, so that the relative strengths of each component can be directly compared. Each curve is plotted for a specific time within the 5-40 Myr range of simulation time, at 1 Myr intervals. The results of the 3-D models are shown alongside those for corresponding 2-D cases. The 3-D along-strike averaged velocities (Fig. 5.6b/e/h) display a typical corner flow pattern, with slab parallel horizontal and vertical velocities trenchward of 200 km, and a flip in horizontal and vertical velocity signs at distances exceeding 200 km, where mantle flow is drawn towards the slab and has an upward component into the arc pinch zone. On average, longitudinal flow is negligible. The 2-D velocities display this same corner flow pattern (Fig. 5.6a/d/f), but include fluctuations around the average corner flow trend that are the expression of SSC drips. These fluctuations are strongest (relative to subduction velocity) in the slowest case, where drips have the most time to develop. Beyond 250 km, the fluctuations are most prominent in the horizontal component, as we are sampling the upper plate at depths where material migrates horizontally towards the drips (i.e. their root zone). The effect of the rolls in 3-D is displayed as the spatial variability around the longitudinal average in Fig. 5.6(c/f/i). This variability is calculated as the absolute difference between the maximum and minimum values of a velocity component which are recorded in the trench-parallel direction, as a function of horizontal distance away from trench. Vertical and longitudinal velocity fluctuations of almost equal magnitude, with their maxima aligned, are the signature of longitudinal Richter rolls.

A comparison of sub-arc along-strike averaged velocities in 3-D models (Fig. 5.6b/e/h) and velocities in the corresponding 2-D simulations with similar model parameters (Fig. 5.6a/d/g), show that 2-D models are a good approximations of the longitudinally averaged flow field. Both in 2-D and 3-D models, as subduction velocity increases, we observe a decrease in the strength of horizontal and vertical components with respect to slab velocity, whilst transients corresponding to the expression of SSC become more prominent with decreasing subduction velocity (i.e. for higher velocity cases wedge flow is more corner-flow like). Note, however, that the variability in velocity is substantially larger in the 3-D cases, where variations commonly exceed the slab velocity, than it is in the 2-D cases, where the variability is less than half the magnitude of slab speeds. Variations in vertical velocities associated with Richter rolls exceeding the convergence velocity were also predicted by Wirth and Korenaga [2012].

In Fig. 5.7, we explore velocities in the back-arc region below the upper plate, at 200 km depth. This depth was chosen for consistency with our previous 2-D model analyses (note that velocities at 200 km depth display similar characteristics to those at 150 km, where our model cross sections are drawn). In the back-arc, a clear corner-flow signature consisting of an almost constant horizontal (Vx) velocity approximately equal to -Vslab (at x > 350 km from the trench), a small vertical velocity, and a longitudinal velocity that is close to zero, is only found for the fastest case (Fig. 5.7g/h). At lower subduction velocities, the subducting slab becomes less efficient at driving wedge flow, and a decoupled cell, which develops at the model's right-hand boundary, leads to substantial upward and outward (positive Vx) velocities. At 200 km depth, lithospheric drips leave pronounced fluctuations in vertical velocity, which increase in strength as slab velocities decrease (Fig. 5.7a/c/d/f).

As we found in the arc region, in the back-arc, the averaged 3-D velocity pattern is very similar to the main pattern of 2-D models. As slab velocities increase, the variability of the three components of flow, which is an expression of SSC, is weaker. Ridges, extending all the way from the arc corner to the side of the wedge in the fast subduction velocity case, yield a comparatively uniform along-strike variability in Fig. 5.7i. In contrast, the vertical component of flow at lower subduction velocities, especially in the 2 cm $yr^{-1}$ model (Fig. 5.7c), exhibits peaks, which are related to the maxima in the temperature slices in Fig. 5.5. These represent transient drips that are only partially sheared into ridges. Consistent with the arc region, velocity variability below the back-arc region in 3-D tends to be larger than in 2-D.

### 5.4.3 Influence of Viscosity

Variations in mantle hydration control wedge viscosity, which, in turn, affects mantle wedge flow fields and strain rates, which further feedback on viscosity. As found in our 2-D models, and predicted by Wirth and Korenaga [2012], viscosity exerts the main control on whether or not SSC occurs. Fig. 5.8 shows sub-arc and sub-back-arc thermal structure for a damp case

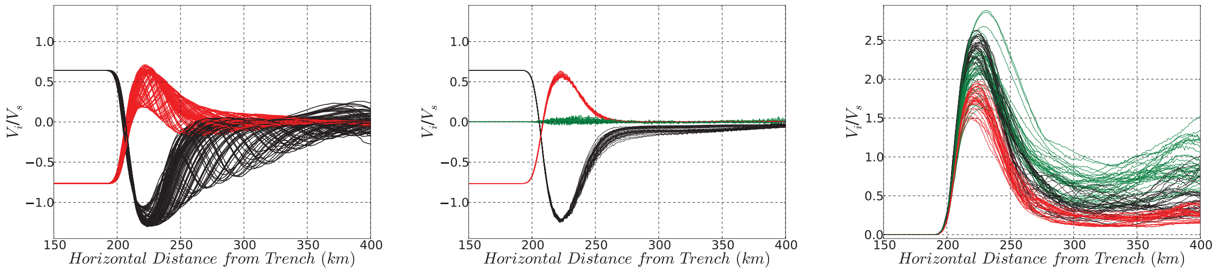

***(a)*** 2D simulation, 2cm yr$^{-1}$

***(b)*** 3D average, 2cm yr$^{-1}$

***(c)*** 3D variability, 2cm yr$^{-1}$

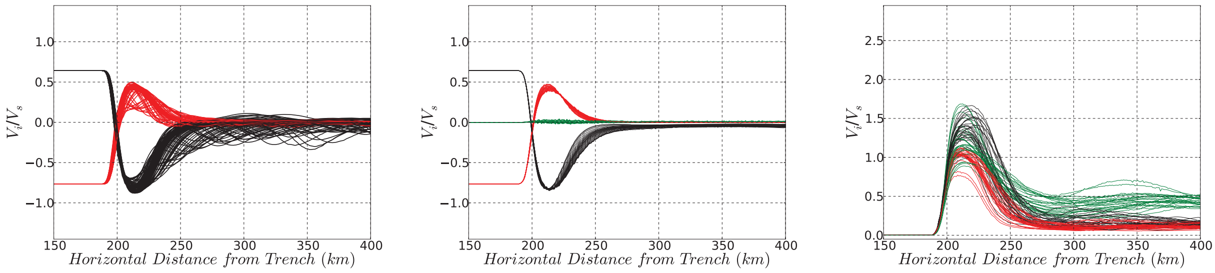

***(d)*** 2D simulation, 5cm yr$^{-1}$

***(e)*** 3D average, 5cm yr$^{-1}$

***(f)*** 3D variability, 5cm yr$^{-1}$

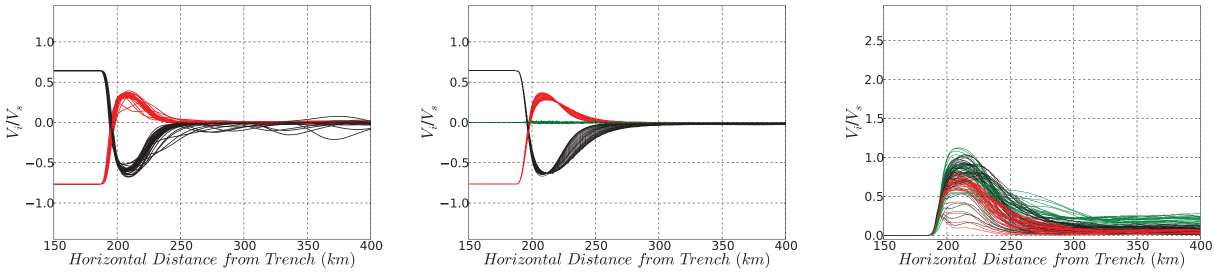

***(g)*** 2D simulation, 10cm yr$^{-1}$

***(h)*** 3D average, 10cm yr$^{-1}$

***(i)*** 3D variability, 10cm yr$^{-1}$

⬛ Horizontal 🟩 Longitudinal 🟥 Vertical

***Figure 5.6:*** *Velocity components of mantle wedge flow close to the wedge corner, at 100 km depth, for cases with a very wet rheology (5000 H/10$^6$Si), old upper plate (120 Myr) and three different slab velocities. Velocities are scaled to the prescribed slab velocity. Positive $V_x$ (black) is in down-dip direction, $V_y$ (red) upward, and $V_z$ (green) in the direction opposite to the trench strike. Lines represents velocities every 1 Myr between model time= 5 Myr and 40 Myr. Note that the total range of relative velocities on all panels is the same, so magnitudes are directly comparable along each row. Comparison of the 2-D simulation velocities (a-d-g), to 3-D longitudinally averaged velocities (b-e-h) illustrates that the 2-D models well capture the average of the 3-D flow. However, the 3-D mean hides the presence of a strong longitudinal component in 3-D models, and significant along-strike variability due to SSC is present in all components of flow (c-f-i).*

with an old upper plate and intermediate subduction velocity of 5 cm yr$^{-1}$. Sub-arc Richter rolls form quite readily, although with a much larger wavelength (Fig. 5.8a) than in the very-wet cases examined previously. Back-arc instabilities, however, take about 40 Myr to form under damp wedge conditions and they are less prominent in comparison to those observed in the very-wet case (Fig. 5.8(b)). Under the arc, 10-12 rolls develop with very similar temperature fluctuations as in the very-wet case. The arc instabilities again interact with the system in the

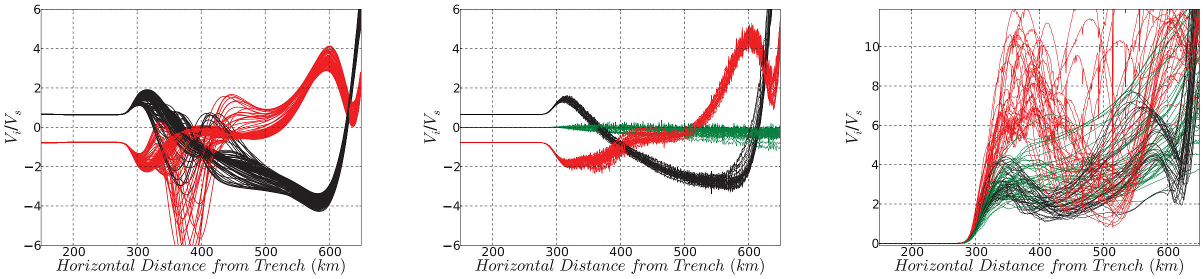

***(a)*** 2D simulation, 2cm $\text{yr}^{-1}$ ***(b)*** 3D average, 2cm $\text{yr}^{-1}$ ***(c)*** 3D variability, 2cm $\text{yr}^{-1}$

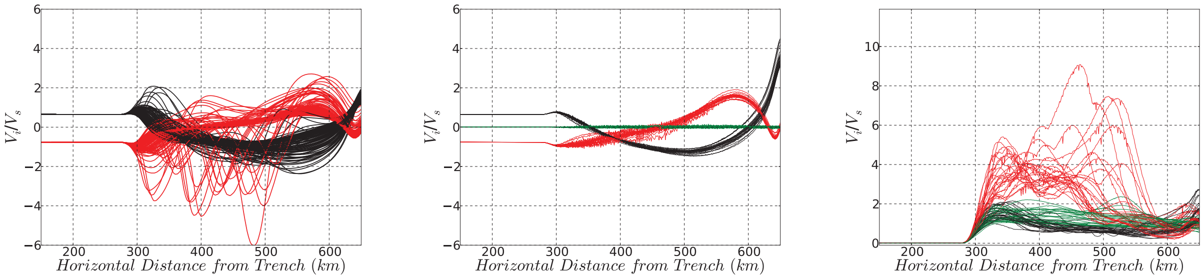

***(d)*** 2D simulation, 5cm $\text{yr}^{-1}$ ***(e)*** 3D average, 5cm $\text{yr}^{-1}$ ***(f)*** 3D variability, 5cm $\text{yr}^{-1}$

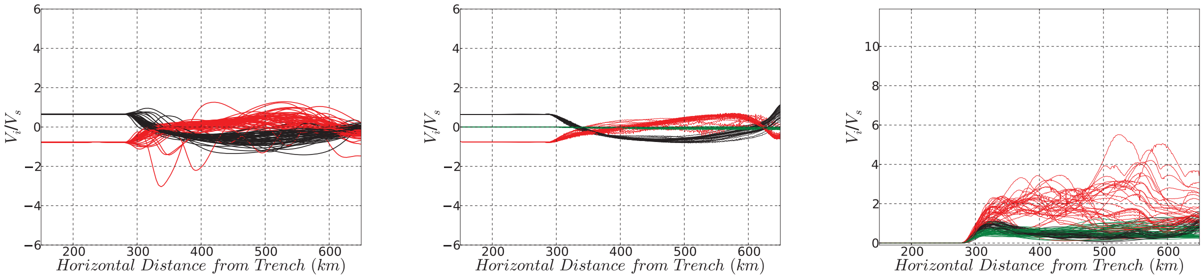

***(g)*** 2D simulation, 10cm $\text{yr}^{-1}$ ***(h)*** 3D average, 10cm $\text{yr}^{-1}$ ***(i)*** 3D variability, 10cm $\text{yr}^{-1}$

▬ Horizontal ▬ Longitudinal ▬ Vertical

***Figure 5.7:*** *Comparison of wedge flow patterns below the upper plates in the back-arc region. Shown are velocity components of mantle wedge flow across the full wedge width, at 200 km depth for cases with a very wet rheology (5000 H/$10^6$Si), old upper plate (120 Myr) and three different slab velocities. As in Fig. 5.6, velocities are scaled to the prescribed slab velocity, and positive $V_x$ (black) is in down-dip direction, $V_y$ (red) upward, and $V_z$ (green) in the direction opposite to the trench strike. The total velocity range is the same on all panels, thus illustrating how SSC becomes increasingly dominant as slab velocity decreases.*

back-arc, once it has developed. Patterns of roll migration are less time-dependent in the model with damp rheology than in the very-wet case.

In contrast, in the dry case, no rolls develop in either the arc or back-arc region over the evolution time of our models (70 Myr for an upper plate that is initially 120 Myr old). Thus for the dry case, as in the 2-D models, the wedge is in a pure corner-flow regime. In the 2-D models, the damp case was also in the corner-flow regime, with a hint of developing back-arc instabilities, however with growth rates that exceeded our 90 Myr long model times. The damp

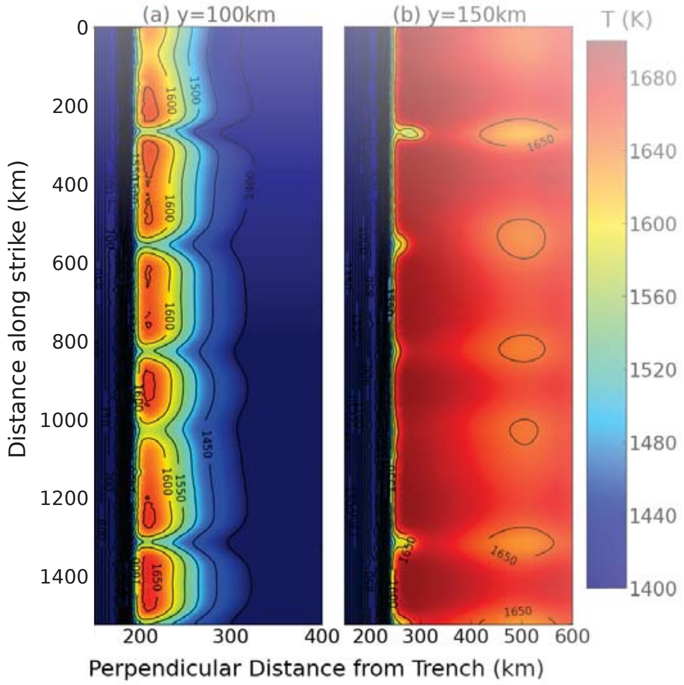

*Figure 5.8: Temperature slices at (a) 100 km and (b) 150 km depths, for a damp (1000 H/$10^6$Si) case with 5 cm yr$^{-1}$ subduction velocity and 120 Myr old upper plate. Richter rolls mainly develop in the arc region, although some interaction with the back-arc system is apparent.*

upper plate is more unstable in 3-D. In the back-arc, 3-D instability time scales may be shorter than in 2-D as previously found for sheared oceanic plate models [van Hunen et al., 2003]. In the arc region, spatial scales, rather than instability time scales, may have suppressed 2-D SSC.

In Figs. 5.9 and 5.10, we examine the differences in velocity systematics in the arc and back-arc regions associated with different viscosities, by probing the evolution of velocity components at 100 km and 200 km depth, again throughout the whole subduction history of our models. The average sub-arc velocity panels in Fig. 5.9 (a/b/d/e) illustrate that, as in 2-D, the average flow pattern is very similar for the three different viscosity cases (compare with Fig. 5.6d/e). The lateral variability in velocities in the damp case (Fig. 5.9c) documents the occurrence of sub-arc Richter rolls (with a Vz component of similar magnitude as Vy), but with about half the velocity variation magnitudes of those in the very wet case with the same subduction velocity (Fig. 5.6f). A small variation observed in the dry case (Fig. 5.9f) hints at the presence of an initiating instability, hampered by high viscosity. In the back-arc, both damp and dry cases are dominated by corner-flow (Fig. 5.10). The damp case does include some ridges with drips, but of very low amplitude compared to the very-wet case, and developing only late in the model evolution.

The dichotomy between arc and back-arc systems is due to differences in mantle viscosity

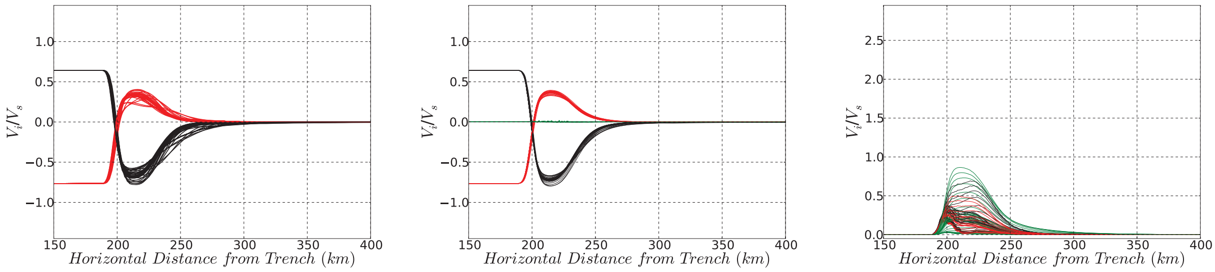

***(a)*** 2D simulation, damp

***(b)*** 3D average, damp

***(c)*** 3D variability, damp

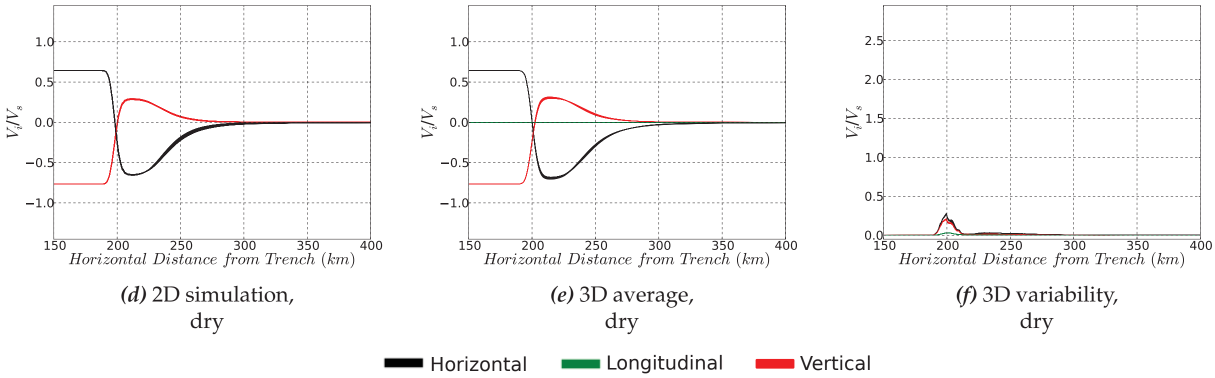

***(d)*** 2D simulation, dry

***(e)*** 3D average, dry

***(f)*** 3D variability, dry

***Figure 5.9:*** *Velocity components in the arc region at 100 km depth for damp (1000 H/$10^6$Si) and dry cases, for a 120 Myr old upper plate and 5 cm yr$^{-1}$ slab velocity, confirm SSC below the arc in the damp case. Figure style and lines are as in Fig. 5.6, where the corresponding panels for the very-wet (5000 H/$10^6$Si) case are shown (panels d-f).*

between the wedge corner, and the region below the upper plate. Estimates of sub-arc and sub-back-arc viscosities are measured inside two volumes (labelled $\mathrm{PROBE}_{\mathrm{ARC}}$ and $\mathrm{PROBE}_{\mathrm{BACK-ARC}}$ on Fig. 5.1) and averaged in the longitudinal direction up to a distance of 150-km away from domain edges. These viscosities are shown in Fig. 5.11 – symbols denote averages with error bars representing trench-parallel variability. Viscosities are displayed for a single time (same upper-plate cooling time for the different velocity cases, i.e., at t=20 Myr for the slow case, t=35 Myr for the intermediate, and t=40 Myr for the fast case). Viscosities in the probed locations vary little with time. Results are illustrated for the cases with a 120 Myr old, thick upper plate (as discussed thus far), as well as for a set of cases with a younger upper plate (discussed in the next section).

The lower viscosities in the sub-arc region are comparable to those observed in 2-D. They are the consequence of bringing material of mantle temperature to shallower depth where the sensitivity of viscosity to temperature is more dominant over that to pressure, compounded by strain-rate weakening that occurs under the power-law creep that dominates this part of the wedge. Mantle viscosities at the base of the upper plate (circles in Fig. 5.11) are up to an order of magnitude higher than below the arc (squares in Fig. 5.11), with the maximum difference

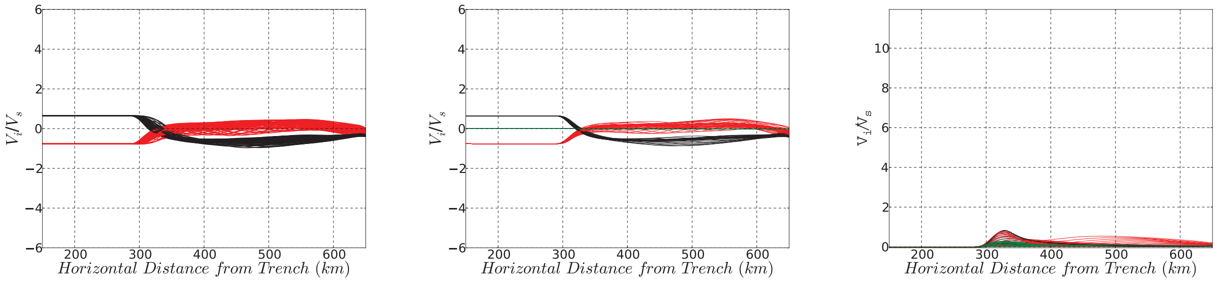

***(a)*** 2D simulation,
damp

***(b)*** 3D average,
damp

***(c)*** 3D variability,
damp

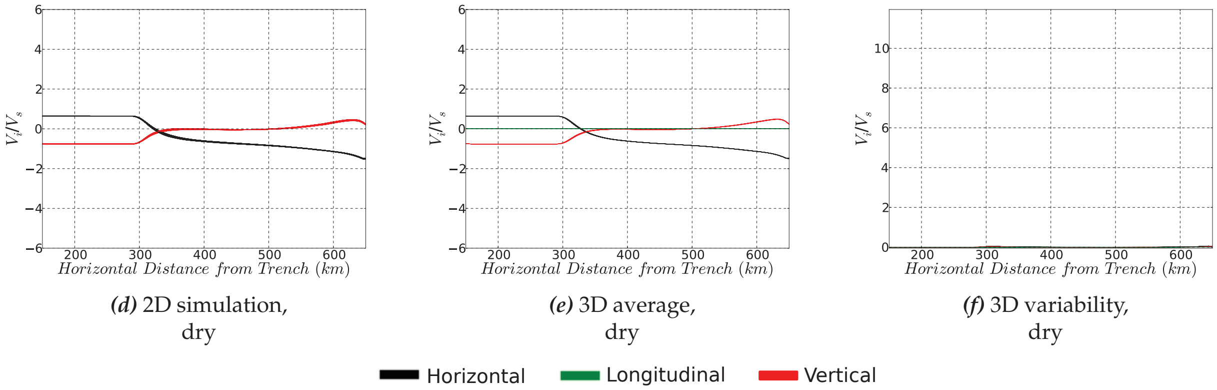

***(d)*** 2D simulation,
dry

***(e)*** 3D average,
dry

***(f)*** 3D variability,
dry

***Figure 5.10:*** *Velocity components in back-arc region at 200-km depth for damp (1000 H/$10^6$Si) and dry cases, 120 Myr old upper plate and 5 cm yr$^{-1}$ slab velocity show that SSC in the damp back-arc is very subdued and SSC is absent for the dry case (zero velocity variation in panel f). Figure style and lines are as in Fig. 5.7, where the corresponding panels for the very-wet (5000 H/$10^6$Si) case are shown (panels d-f).*

observed in the dry case with an old upper plate. In all cases, excluding the 120 Myr old upper plate case with a subduction velocity of 2 cm yr$^{-1}$, viscosity is lower in the wedge corner than below the upper plate. As we have seen in 2-D and in Section 5.4.2, this is the case where SSC most strongly disrupts corner flow. In this case, fluctuations in wedge corner viscosity are very strong, and the measure of average corner viscosity includes signatures of the drips, and is thus not an optimal indicator of the behaviour. The measure of along-strike variability in viscosity shows that viscosities in the corner reach lower maxima than below the upper plate. The lower sub-arc than sub-back-arc viscosities explain the difference in instability wavelengths between the two systems.

In our 2-D models, SSC did not occur where mantle viscosities exceeded a cut-off viscosity of $\approx 5 \cdot 10^{18}$ Pa·s. The same is true in 3-D. This behaviour is compatible with previous results by Wirth and Korenaga [2012] (who used a single-mode 3D approach) and Honda [2008] (who limited wedge hydration to the wedge corner), although the cut-off viscosities are slightly higher in our models, where fully 3-D flow (i.e. with different wavelengths) can develop over a wider region than the hydrated wedge corner defined by Honda [2008].

### 5.4.4 Influence of Upper Plate Age

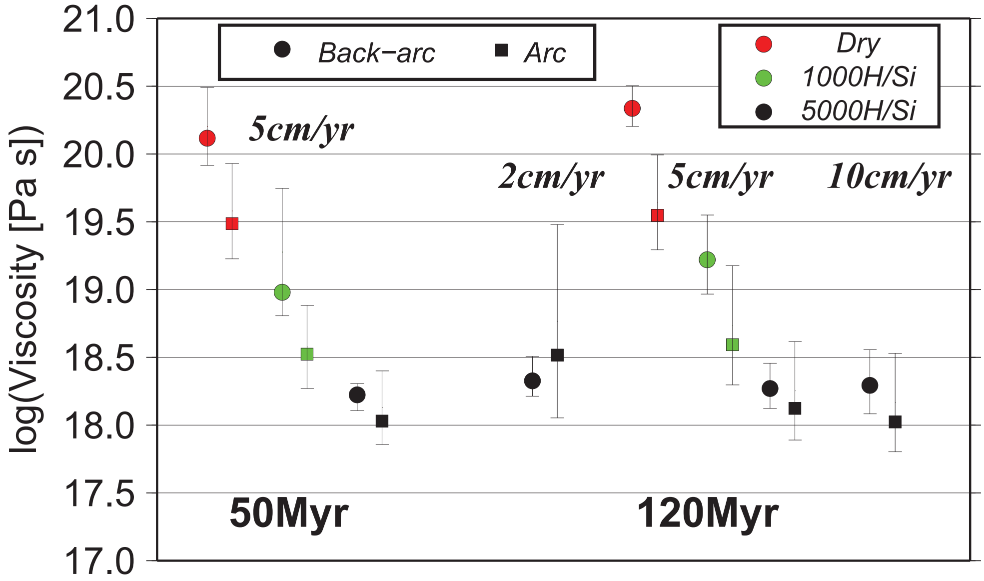

***Figure 5.11:*** *Viscosity as determined in the boxes displayed in Fig. 5.1 beneath the arc (squares) and back-arc (circles) Symbols display the average and error bars variability in the longitudinal direction. Plotted for a time of 20 Myr in the slow case, 35 Myr in the reference and 40 Myr in the fast, corresponding to the same upper plate cooling time in each case. The time variation of viscosity is minor. For the intermediate velocity case, three viscosity cases and two plate thicknesses are shown, while slow and fast cases are only displayed for very wet rheology and thick upper plate.*

Finally, we examine the influence of plate age on the flow regime, as thicker (i.e. older) plates are well-known to be more unstable than thinner (i.e. younger) plates [e.g. Davaille and Jaupart, 1994]. We ran intermediate subduction velocity cases with a 50 Myr old (i.e. younger and thinner) upper plate, for three different viscosities (very-wet, damp and dry). We characterised the arc and back-arc systems at slightly shallower depths than before, 75 km and 150 km, to best capture the character of the two systems below these thinner plates.

The resulting thermal structure is illustrated in Fig. 5.12. We display only the results from the damp and very-wet cases as the dry case exhibits similar behaviour to the damp case (but attains 25-50 K cooler arc temperatures). The young and damp upper-plate does not thicken sufficiently fast to develop instabilities, preventing the formation of rolls below both the arc and back-arc regions. This is the same as in 2-D, where neither damp nor dry models with a young upper plate developed SSC. The very-wet young upper-plate case does develop significant SSC below the arc and back-arc. In 2-D, we observed how a thin upper-plate with very-wet mantle rheology favoured the development of a very short time and length-scale pattern of SSC. Similar behaviour emerges in 3-D.

However, separation between the two SSC systems for the very-wet case is not as marked as that observed below 120 Myr old plates. In comparison with cases with an older overriding plate, sub-arc pinching by mantle flow is less severe. Under these conditions, the geometrical effect of an isolated arc region observed under old upper plates, due to a strong gradient in thickness between the arc and back-arc, is substantially weaker. As a result, the two systems have more similar wavelengths, and the sub-arc Richter rolls are more connected to the instabilities forming in the back-arc (see Fig. 5.12c,d).

Individual velocity components at a depth that cuts through the arc system (Fig. 5.13) reflect the lower amount of sub-arc upper plate erosion in the subdued average vertical velocity component (panels b/e/h) compared to the 120 Myr old upper plate cases (Figs. 5.6 and 5.9). Velocity variations for the very-wet case (Fig. 5.13c) retain some signature of the arc and back-arc systems in the two vertical velocity maxima. However, the maxima have similar velocity magnitudes, due to the reduced viscosity contrast between arc and back-arc regions (Fig. 5.11 – note that the probing locations for viscosity displayed in Fig. 5.11 were the same for old and young plates and, hence, do not capture this difference in viscosity between the old and young cases).

Although these results seem to indicate that the distinct sub-arc and sub-back-arc flow behaviour is principally a feature of systems with thick upper plates, it should be noted that the fixed upper-plate slab coupling depth of 80 km imposed in our models exerts a strong constraint on wedge corner upper-plate erosion. A rheologically (and hence thermally) controlled coupling depth may lead to a more pronounced sub-arc thinning of the upper-plate also for a younger upper plate, although too small a coupling depth is inconsistent with the low-heatflow forearc region [e.g. Arcay et al., 2008, Conder, 2005].

## 5.5 Consequences of SSC in 3-D

Our 2-D study (see Chapter 4) demonstrated that SSC can thin sub-arc lithosphere by a few km, and back-arc lithosphere by 10-15 km, under wet to very-wet mantle conditions, and thereby extend the region where wet melting is possible from absent (for dry cases) to spanning most of the arc and back-arc region, but disrupted by drips. These drips could also modify slab-surface temperatures by up to 100 K and shift dehydration boundaries by up to 20 km. In this section, we analyse each of these consequences for our 3-D models.

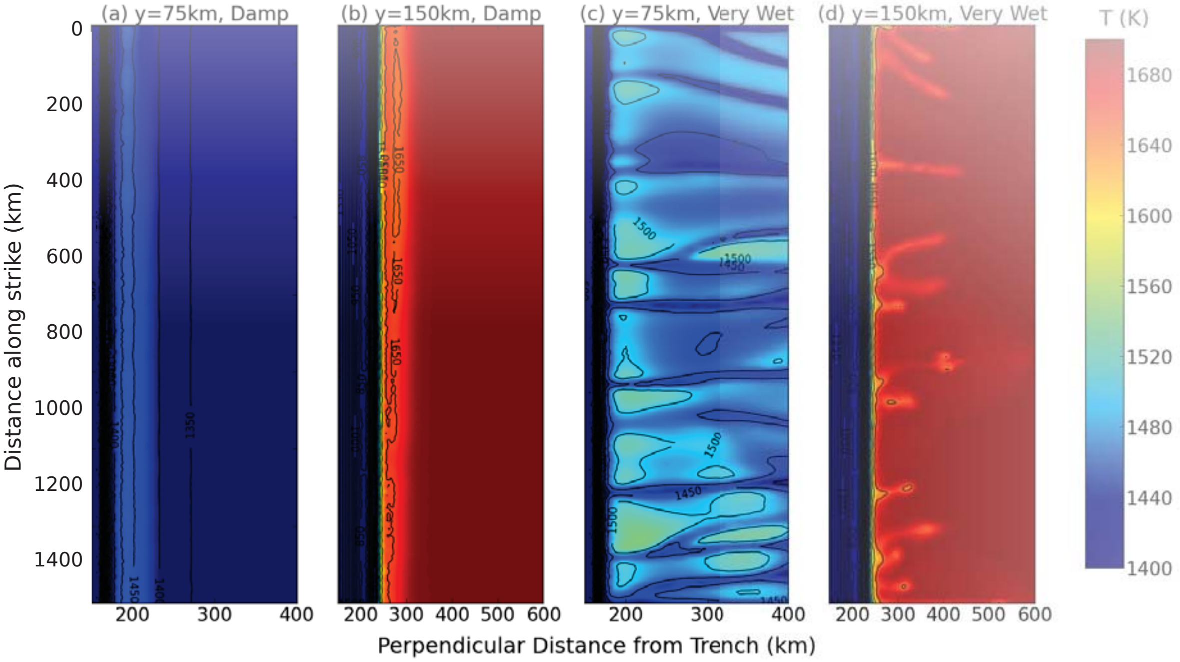

*Figure 5.12: Horizontal slices of temperature at 75 km and 150 km depth, for cases with damp and very wet rheology and $V_{slab}$ of 5 cm $yr^{-1}$. These depths illustrate the flow pattern below the arc and back-arc region for the is young plate case. Note that the horizontal scale of the below-arc slices is half that of the below-back-arc ones.*

### 5.5.1 Upper Plate Lithospheric Thickness

We use the depth of the 1400K isotherm as a proxy for upper plate lithospheric thickness. In the 2-D models, this measure was verified against conductive thermal thicknesses inferred from lithospheric geotherms. Fig. 5.14(a) illustrates that, consistent with our 2-D results, lithospheric thinning below the arc region is generally most efficient in cases with: (i) increased subduction velocities; (ii) increased wedge hydration; and (iii) younger upper plates. A minor, but systematic difference is observed between arc-lithospheric thicknesses in the 2-D and 3-D cases, with 2-D models generally underestimating the extent of lithospheric thinning beneath the arc, by $\leqslant 3$ km. The increased efficiency of lithospheric thinning in 3-D is a direct consequence of arc Richter-rolls, which are unique to the 3-D system. In addition, the 3-D rolls produce trench parallel variations in lithospheric thickness of $\leqslant 7$ km. Such differences will have a minor effect on estimates of surface heat flow, but will affect melting conditions, as these are very sensitive to exact lithospheric thickness (see Section 5.5.2 below).

Our lithospheric thicknesses estimates below the back-arc region are illustrated in Fig. 5.14(b). For dry cases, 2-D models provide a reasonable approximation to the average lithospheric erosion predicted in 3-D. However, consistent with our predictions for the arc region, we find that with increasing levels of wedge hydration, 2-D models systematically under pre-

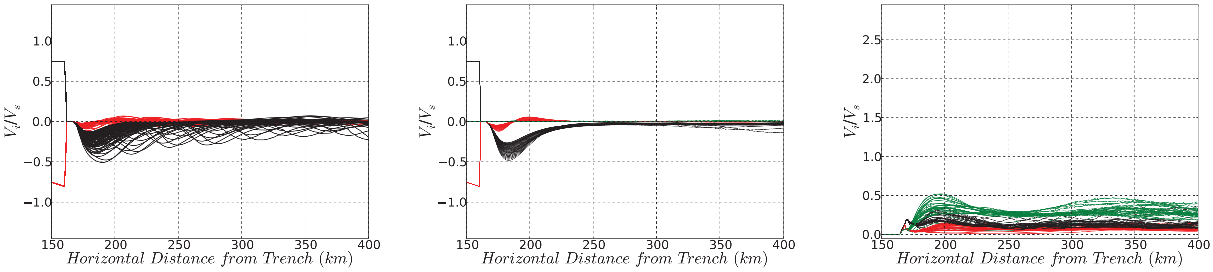

***(a)*** 2D simulation,
very wet

***(b)*** 3D average,
very wet

***(c)*** 3D variability,
very wet

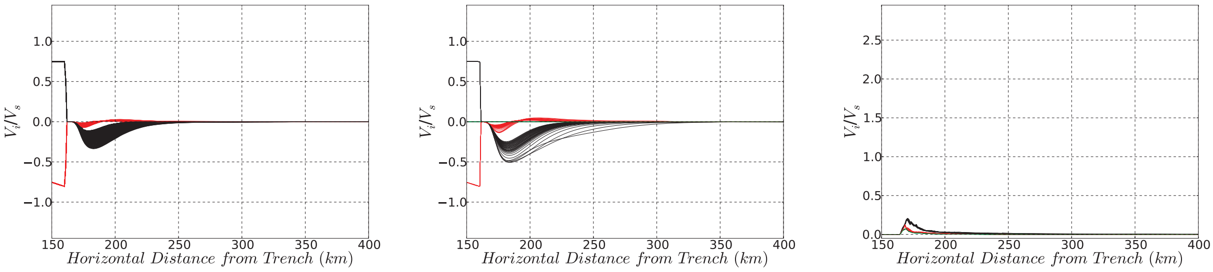

***(d)*** 2D simulation,
damp

***(e)*** 3D average,
damp

***(f)*** 3D variability,
damp

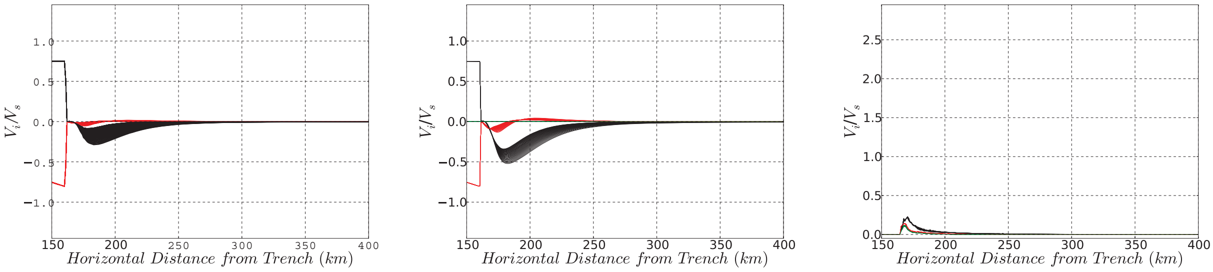

***(g)*** 2D simulation,
dry

***(h)*** 3D average,
dry

***(i)*** 3D variability,
dry

■ Horizontal 🟩 Longitudinal 🟥 Vertical

***Figure 5.13:*** *Velocity components at 75-km depth for very wet (5000 H/$10^6$Si), damp (1000 H/$10^6$Si) and dry cases, with a 50 Myr old upper plate and 5 cm $yr^{-1}$ slab velocity, illustrating the pattern of sub-arc flow. As in Fig. 5.6, velocities are scaled to the prescribed slab velocity, and positive $V_x$ (black) is in down-dip direction, $V_y$ (red) upward, and $V_z$ (green) in the direction opposite to the trench strike. The total velocity range is the same on all panels*

dict the amount of lithospheric thinning, when compared to 3-D models. In very wet cases, the differences between 2-D predictions and the average of 3-D models can be up to 10 km, whilst 3-D models can show substantial trench parallel variations in thickness, of up to 20 km. However, even with this additional thinning our back-arc lithospheric thicknesses remain on the high side compared with the ≈ 60 km back-arc thicknesses inferred from heat flow and seismic velocities by Currie and Hyndman [2006]. Currie et al. [2008] attributed this thinning to even stronger hydrous plate weakening, through visco-plastic mechanisms.

*(a)* Sub-Arc Lithospheric Thickness

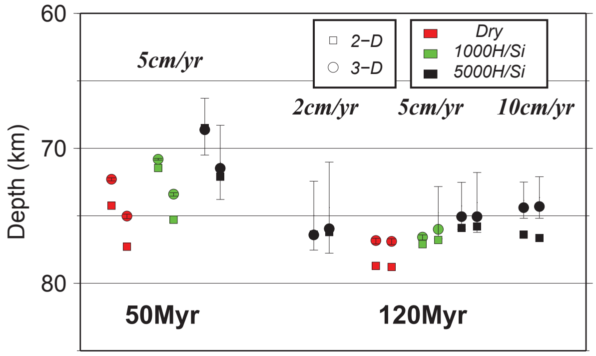

*(b)* Sub-Back-Arc Lithospheric Thickness

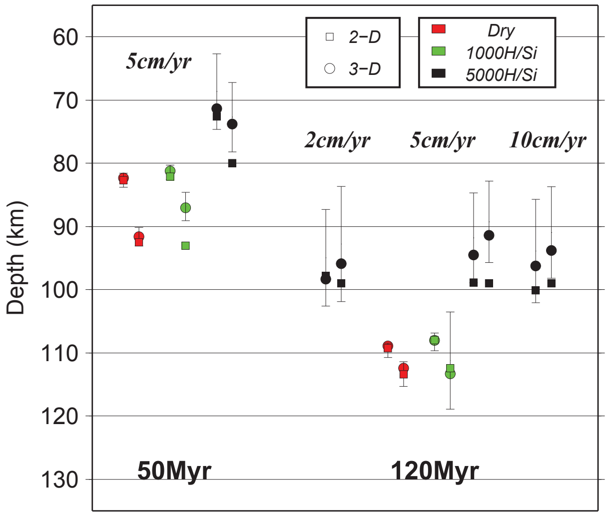

***Figure 5.14:*** *Variations in upper-plate thickness in the (a) sub-arc and (b) sub-back-arc regions, for all the 3-D models cases presented in this chapter. Thicknesses are measured as depth of the 1400K isotherm, averaged along the horizontal span in the transverse direction illustrated by the dotted-dashed line labelled* $PROBE_{ARC}$ *and* $PROBE_{BACK-ARC}$ *in Fig. 5.1 (respectively in the 150-300 km and 350-500 km horizontal distance range from the trench, longitudinally in the central 1200-km). Error bars denote along-strike variability in the 3-D simulations, around the average thickness values (circles). For comparison, we include results for the analogue region in 2-D simulations with corresponding model parameters (squares). Two values are given for each case, spanning 35 Myr of simulation time, in ranges encompassing the same amount of upper plate conductive thickening (t=5 Myr and t=35 Myr for cases with slow subduction; t=20 Myr and t=50 Myr for intermediate; t=25 Myr and t=55 Myr for fast). Thicknesses estimated from the 2-D simulations are systematically larger than for the 3-D cases, especially in the arc region.*

### 5.5.2 Wedge Thermal Structure & Melting

In Fig. 5.15, we illustrate thermal conditions below the arc, by plotting trench-parallel temperature averages and ranges, at 75 and 100 km depth, for 50 and 120 Myr old upper plate cases, respectively, alongside wet and damp solidi from Katz et al. [2003]. Note that at distances beyond 250-300 km, we are plotting temperatures at the base of the thermal lithosphere for the very-wet cases (at all subduction velocities, and for old as well as young upper plates), but within the upper plate for damp and dry cases. This is reflected in the $\sim 50 - 75$K higher average temperatures for the very-wet than for comparable damp and dry cases (Fig. 5.15b/c).

Due to the stronger lithospheric thinning, the 3-D models predict elevated temperatures at shallower depths when compared to 2-D models. As the base of the thermal lithosphere provides the conditions where melting is most likely to occur, such changes directly enlarge the potential melt region. Average temperatures below the volcanic arc are highest, relative to local melting temperatures, for cases with: (i) the fastest subduction velocities, due to stronger 'pinching' in the wedge corner (Fig. 5.15a); and (ii) increased wedge hydration (Fig. 5.15c), due to enhanced lithospheric thinning, through SSC; and (iii) for the younger upper plates. As was predicted in our 2-D models, wedge temperatures are sufficiently high for wet melting to occur, locally, in parts of all except the dry models (this assumes that locally wet conditions may permit melting even if hydration is insufficient in extent to affect wedge rheology), whilst damp melting can occur below the arc region in the most hydrated cases, at subduction velocities of 5 and 10 cm yr$^{-1}$. However, again consistent with our 2-D results, in all cases examined, temperatures are too low for dry melting.

Lateral variations in lithospheric thickness and, thereby, temperature, associated with the 3-D rolls provide conditions for forming melt pockets below the arc (and back-arc) region. This variability increases for cases with decreased subduction velocities (Fig. 5.15b) and increased wedge hydration (Fig. 5.15d). In our reference case with a subduction velocity of 2 cm yr$^{-1}$, the range between maximum and minimum along-strike temperatures exceeds $\sim 150$K. Conversely, for a case with a subduction velocity of 10 cm yr$^{-1}$, the range is $\sim 80$K (Fig. 5.15b). Along strike variations can also exceed $\sim 150$K for very wet cases, regardless of upper plate age (Fig. 5.15d/e), whilst variations of $\sim 120$K are predicted for a 120 Myr old upper plate case, with a damp rheology (Fig. 5.15d). However, they are reduced to $\sim 50$K, at most, for damp cases with a 50 Myr old upper plate, and are insignificant for dry cases regardless of upper plate age, as these models exhibit a stable corner flow regime. We note that along strike variability in back-arc temperatures follows a similar trend to those beneath the arc region. Such along-strike variations in thermal structure and melting may be responsible for the complex seismic velocity structures imaged, for example, beneath the Japanese volcanic arc [Tamura et al., 2002], and have also been related to the local spacing in arc volcanism [Honda and Saito, 2003, Honda and Yoshida, 2005].

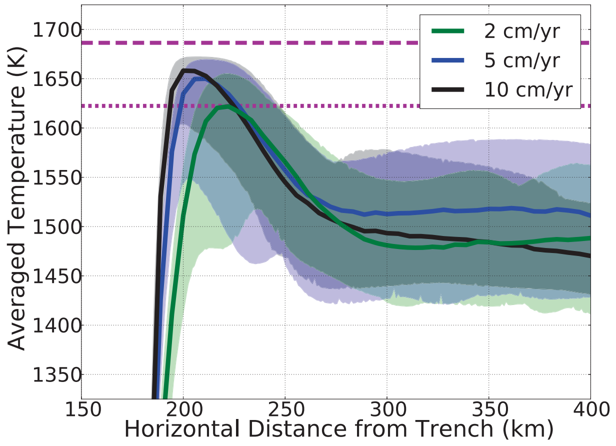

***(a)*** Effect of slab velocity, 120 Myr

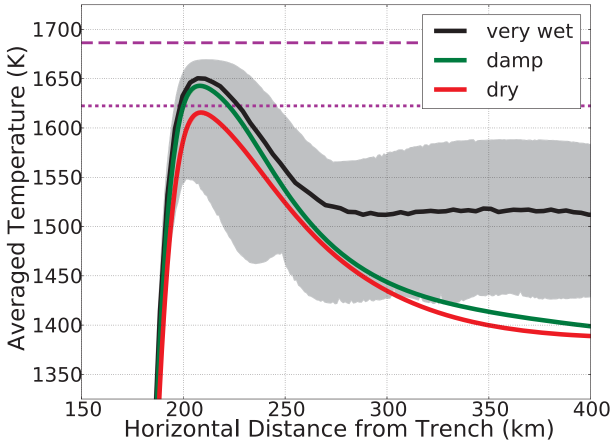

***(b)*** Effect of mantle hydration, 120 Myr

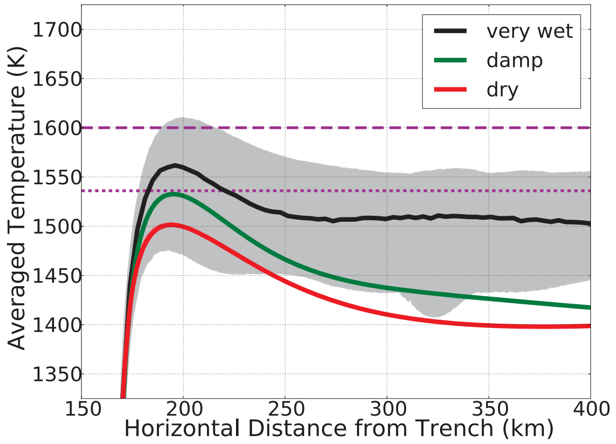

***(c)*** Effect of mantle hydration, 50 Myr

***Figure 5.15:*** *Along-strike variability in temperature at 100 km depth, for models with a 120 Myr-old upper plate and varying: (a) slab velocity; and (b) viscosity, and at 75 km depth for models with 50 Myr-old upper plate varying (c) viscosity. Panels (b,c) are for a model with a subduction velocity of 5 cm* $yr^{-1}$. *All lines represent a snapshot at a cooling time of 35 Myr. Shaded regions represent along-strike maxima and minima at varying horizontal distances from trench. Along-strike variability is negligible for damp and dry cases. Dotted and dashed lines coloured in magenta indicate mantle solidus temperatures, respectively under "damp" and "wet" conditions. The different depths for old and young upper-plate cases are chosen in order to best capture the extent by which mantle solidi are crossed in the wedge corner in each model.*

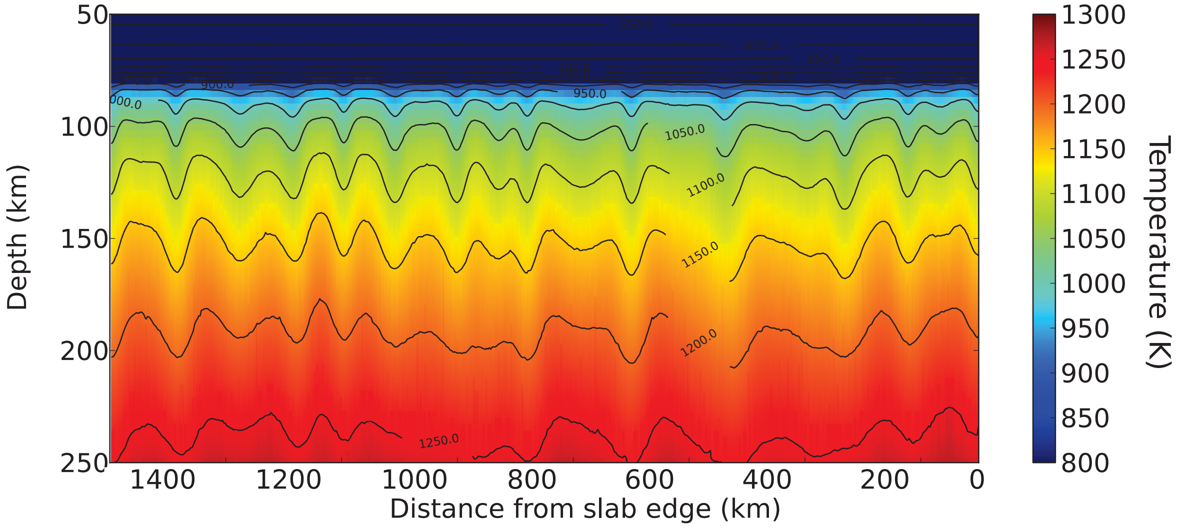

**(a)** SST, 5000 H/$10^6$Si, $V_{SLAB} = 2$ cm yr$^{-1}$

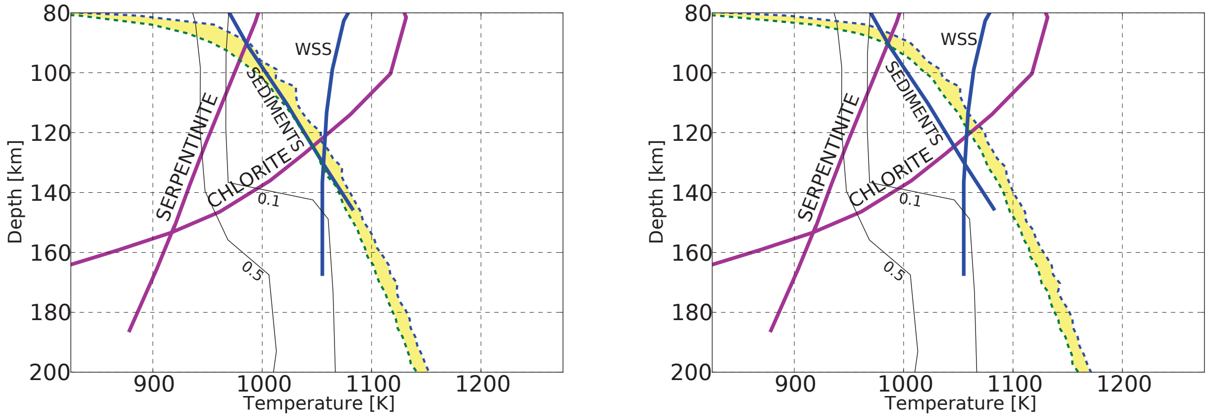

**(b)** SST range, Dry, $V_{SLAB} = 5$ cm yr$^{-1}$

**(c)** SST range, 1000 H/$10^6$Si, $V_{SLAB} = 5$ cm yr$^{-1}$

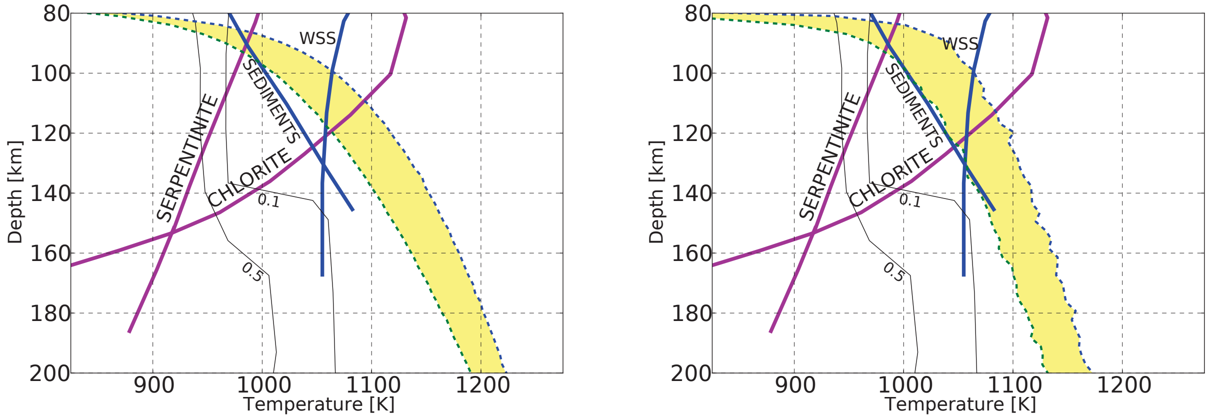

**(d)** SST range, 5000 H/$10^6$Si, $V_{SLAB} = 2$ cm yr$^{-1}$

**(e)** SST range, 5000 H/$10^6$Si, $V_{SLAB} = 10$ cm yr$^{-1}$

***Figure 5.16:*** *Slab surface temperatures (SSTs) observed at 30 Myr, for cases with a 120 Myr-old upper-plate. An example of the along-strike variability of SST is shown on panel (a), for the case with slow subduction. Yellow-shaded regions in (b,c,d,e) represent the range of SSTs for cases with: (b) dry rheology ; (c) damp rheology ; (d) very wet rheology and slow subduction ; (e) very wet rheology and fast subduction. Blue and green dotted lines outlining the yellow regions indicate along-strike temperature maxima and minima at each depth. Pink lines represent the conditions at which common mantle hydrous minerals break down, blue lines are sediment and wet mantle solidi (all from Grove et al. [2012], and thin black lines illustrate where basalt would retain 0.5 and 0.1 wt% of water [Hacker, 2008]. Richter rolls forming below the arc can turn off and on the breakdown of hydrous minerals at different longitudinal locations, in particular for very-wet cases with faster subduction velocities.*

### 5.5.3 Slab Surface Temperatures

Fig. 5.16 illustrates the range of along-strike slab surface temperatures (SSTs), for different cases with a 120 Myr old upper plate, after 30 Myr of model evolution, alongside MORB dehydration boundaries, the stability fields for hydrous mantle minerals, and water-saturated sediment and mantle solidi. As in our 2-D models, we find that higher subduction velocities, higher wedge viscosities and larger upper plate thickness all result in decreased SSTs. Along strike variations in SSTs for the 3-D models are most sensitive to the level of wedge hydration: the maximum range of $\sim 60$K is observed for very wet cases, with the range decreasing to $\sim 20$K for comparable damp cases. Peaks and troughs in SSTs occur at a wavelength that roughly corresponds to that of the Richter rolls in the arc region (Fig. 5.16(a)), implying that 3-D instabilities have a more significant influence on SSTs than those observed in 2-D, where the signature of drips was not apparent at the slab surface.

There are additional, subtle, differences between the predictions of our 2-D and 3-D studies. By virtue of the increased temperatures obtained with respect to 2-D models, in all hydrated 3-D models, SSTs always exceed the hydrous-sediment melting curve above $\sim 90$km depth. Even for the dry wedge case, melting of water-saturated sediments is possible. This higher average temperature also significantly alters the depth at which the water-saturated solidus (labelled WSS in Fig. 5.16b-e) is crossed. For example, in a dry wedge case at intermediate subduction velocity, this boundary is shifted by as much as 50 km, in comparison to the equivalent 2-D case.

The observed along-strike variations in temperature are insufficient to significantly influence the dehydration of crustal material: in all models, the completion of dehydration for MORB material at the slab's surface (taken as the boundary where water content drops below 0.1 wt %) occurs above 90-km depth. As noted in our 2-D study, in addition to controlling crustal dehydration, SSTs can also affect the dehydration of mantle minerals [e.g. Peacock, 1990b, 1996, van Keken et al., 2011], where they are exposed at the slab's surface (e.g. in oceanic core complexes). Furthermore, even large variability in temperature will occur in the wedge just above the slab's surface where released fluids may be first taken up by mantle minerals and released when conditions exceed their stability fields [e.g. Grove et al., 2012]. If mantle minerals are exposed at the slab's surface, the range of predicted model SSTs could shift the depth where serpentinite and chlorite break-down by as much as 20 km. This could yield substantial along strike variations in fluid release from the subducting slab, which likely has significant implications for volcanic spacing [Wilson et al., 2013].

## 5.6 Conclusions

We have presented a detailed analysis of 3-D mantle wedge convection styles taking into account the effect of hydrated rheologies and local thermal buoyancy, and comparison with similar 2-D models from the previous chapter 4. As in our 2-D study, we find that small-scale convection (SSC) is a common occurrence, requiring similar conditions (i.e. wedge viscosities below $5 \cdot 10^{18}$ Pa s), consistent with what has been found in previous 2-D and 3-D studies [e.g. Honda and Saito, 2003, Arcay et al., 2005, Honda et al., 2010, Wirth and Korenaga, 2012]. As in 2-D, the exact form of SSC depends on subduction velocity and wedge viscosity. However, in 3-D, Richter-rolls, with axes aligned perpendicular to the trench (longitudinal rolls), become the dominant mode of instability [Richter, 1973, Wirth and Korenaga, 2012].

In contrast to our 2-D results, two separate, but interacting, SSC systems form, the first below the arc region, where the upper-plate is pinched by the wedge flow, and the second below the back-arc region. The arc rolls are specific to the 3-D system and arise due to the additional degree-of-freedom, which permits the development of small-scale longitudinal rolls, on a wavelength of $\sim$50-200 km, for which the pinch zone that forms in the 2-D system offers insufficient space. In the back-arc system, Rayleigh-Taylor drips, spawned from the base of the overriding plate, are sheared by background corner flow to form long, linear, cold ridges. These ridges, which form the downwelling limbs of larger-scale Richter rolls, extend from the back-arc region into the arc region, and have a larger spacing than instabilities in the arc region, 100-400 km, due to the higher viscosities in the back-arc. Both arc and back-arc rolls are highly time-dependent, migrating, interacting and coalescing with surrounding instabilities. These two systems interact, particularly at higher subduction velocities and for thinner upper plates. We find that the separate arc system is less prominent beneath younger upper plates. However, the two systems may be more distinct also for young plates, if the coupling depth between subducting and overriding plates would shallow with increasing temperature (as was done by Arcay et al. [2005, 2007]). It is interesting to note that the system naturally evolves into arc and back-arc regions even without a limitation on the distance to which the wedge is hydrated by the down-going plate.

Our study demonstrates that 2-D models, in many ways, provide a good approximation to the average of 3-D models. However, in our models, lithospheric thinning is slightly more efficient in 3-D, and the few additional kilometres of lithospheric erosion are sufficient to enlarge the region over which dehydration and melting can occur considerably. In addition, arc-rolls lead to trench parallel temperature variations of $\sim$150K and along-strike variations in lithospheric thickness of 5-10 km. These fluctuations provide a potential mechanism for explaining along-strike variations in heat flow, seismic structure, and magmatism. The wavelength of arc Richter-rolls predicted herein, is larger than the common spacing between volcanic centres [e.g. de Bremond d'Ars et al., 1995]. Nonetheless, as was proposed by de Bremond d'Ars et al. [1995], smaller spacing could result from strong time-dependence of the position of high-temperature regions.

On Earth, wedge thermal structure is likely further affected by a heterogeneous distribution of volatiles, and strong gradients or steps in lithospheric thickness. As we verified in chapter 4, spawning of sub-lithospheric instabilities can be facilitated by the presence of such features. In addition, wedge flow patterns and temperatures may be modified by 3-D slab geometry [Kneller and van Keken, 2008], and the flow around slab edges [Kincaid and Griffiths, 2004]. The addition of such complexities is an important avenue for future work. Accordingly, in the following chapter, we present some preliminary results for finite-width slabs.

# Chapter 6

# Impact of Finite Slab Width, Side Plates and Slab Rollback on 3-D Mantle Wedge Flow and Thermal Structure: A Preliminary Study

## 6.1 Summary

**The subduction mantle wedge is a key region where volatiles are recycled into the solid Earth or channeled towards the upper plate where they affect volcanism, seismicity, mineralisation and crust formation. Numerical modelling of wedge flow and thermal structure is commonly done in 2-D. In this study we investigate some of the effects of a finite-width slab using a kinematically driven 3-D model with dynamic flow below, around and above the slab, for subduction with and without trench retreat. The finite width allows toroidal flow around the slab sides. Although, except in a case with a strongly hydrated wedge corner, this flow is not very efficient at entering the wedge corner, it is sufficient to modify temperatures in such a way that it can locally shut down or enhance wet melting. Flow around the slab draws out a cold anomaly in a hook shape from the sides. The exact shape of this hook will be affected by deformation of the slab (which we do not model), however, this cold anomaly does affect flow into the wedge, and can lead to cold filaments being drawn into it. An important influence is exerted by the plate which overrides the mantle on the side of the subducting slab's edge. Thick (old) side plates block flow into the shallowest wedge corner**

**where conditions are closest to those required for melting. Based on the work presented in the previous chapters on hydrous wedge conditions, such steps in plate thickness would also be expected to form the triggering or pinning points of instabilities. For a hydrated corner limited to a distance of 150 km from the fore-arc corner, along-strike flow into the wedge can be strongly enhanced, modifying the pattern of SSC, and thereby melting and dehydration, and possibly seismic anisotropy.**

## 6.2 Introduction

Because of the key role that the subduction mantle wedge plays in volatile recycling, subduction-zone natural hazards and the concentration of mineral resources, many studies have modelled wedge flow and temperature to try to better understand the controls on the diversity of Earth's subduction zones and their associated surface expressions.

Most mantle wedge modelling has been done in 2-D [e.g. Davies and Stevenson, 1992, Peacock and Wang, 1999, Syracuse et al., 2010], as the dimensions of the wedge system are much smaller in trench-perpendicular than trench-parallel direction. However, the complexity in subduction wedge observations can likely only be explained by 3-D variations. A few studies investigated flow for 3-D plates with an infinite lateral extent [chapter 5 herein, Honda et al., 2010, Wirth and Korenaga, 2012, Hall et al., 2000], including some that evaluated the influence of geometrical complexity [Kneller and van Keken, 2008]. These show that small-scale convection, upper plate shearing and pressure gradients along slab morphology can all complicate wedge flow.

However, it has also been well established that the finite lateral extent of slabs plays a crucial role in large-scale slab dynamics, as it facilitates trench motions by allowing flow around the slab's sides [e.g., Garfunkel et al., 1986, Funiciello et al., 2003, Schellart, 2004, Morra et al., 2006]. Present-day as well as Cenozoic plate motions confirm that most trenches indeed retreat [Garfunkel et al., 1986, Sdrolias and Müller, 2006, Seton et al., 2012]. Furthermore, a number of seismic and geochemical observations are consistent with flow from the subslab region, into the mantle wedge around slab edges [Pearce et al., 2001, Wendt et al., 1997, Trua et al., 2003, Smith et al., 2001, Civello and Margheriti, 2004]. Kincaid and Griffiths [2003, 2004] set up analogue models specifically to investigate the effect of the flow around the slab edge on the mantle wedge, and found that wedge and slab surface temperatures were significantly different for cases without slab rollback, where slab edges were warmer than the slab centreline, and with rollback, where this relative temperature difference between edges and interior was reversed.

In this chapter we perform a preliminary numerical investigation of the morphology of wedge flow resulting from subduction of a finite-width plate. Most of the presented models concentrate on a dry mantle rheology, and we examine the impact of slab rollback and age of the side plate (the plate bordering the subducting and upper plate). For each case we evaluate the effect on sub-arc wedge temperatures in comparison with the thermal structure predicted for an infinite-width plate from the previous chapter.

## 6.3 3-D Model Setup with Slab Edge

As in the previous two chapters we drive the model slab kinematically, while we solve for the resulting dynamic mantle flow. We expand the model described in our previous 3-D study (section 5.3), to include a side plate which extends beyond a now finite-width slab, and overlies a mantle volume. This model setup allows mantle material from below the slab to move around the slab edge beneath the side plate, and into the mantle wedge beneath the overriding plate. In addition, we investigate the effects of a prescribed slab roll-back velocity. Solutions of the Stokes and energy equations assume the mantle is an incompressible, Boussinesq fluid and are obtained using Fluidity [Davies et al., 2011, Kramer et al., 2012]. We again utilize the solution strategies outlined in section 3.4, and described in Davies et al. [2011].

### 6.3.1 Geometry, Boundary & Initial Conditions

The finite-slab 3-D model setup is illustrated in Fig. 6.1. As for the models presented in the previous chapters, the computational domain is 400 km deep (y-)direction. It extends 1000 km in the transverse (x-)direction and 1500 km in the longitudinal (z-)direction. The side plate and subducting plate are both 750 km wide in the z-dimension. The subducting plate travels horizontally at the surface for 350 km, then subducts at the trench following a down-dipping circular arc to a depth of 75 km. Below this depth, it subducts at a constant dip angle of 50°. The width of the upper-plate (in x-direction) is 650 km at the surface, consistent with the domains in chapters 4 and 5. For our boundary conditions, these model dimensions allow sufficient space for the dynamics of flow around slab edge to develop. Mesh resolution varies from a minimum of 2 km at the wedge corner and slab edge, to a maximum of 8 km at the base of the domain and at the front vertical surface of the side plate. Model validation, detailed in chapter 3, proves accurate resolution of large- and small-scale physics in the wedge at these mesh resolutions.

Boundary conditions applied for the downgoing and upper plates mirror those in the 3-D models presented in chapter 5. Surface temperature, $T_s$, is fixed to 273K. Boundary conditions on all vertical sides follow an error function:

$$T(x=0,y) = T_s + (T_0 - T_s)\mathrm{erf}(\frac{y}{2\sqrt{\kappa t_{\mathrm{plate}}}}). \tag{6.1}$$

In this chapter $t_{\mathrm{plate}}$ is either the subducting slab age, $t_{\mathrm{subd}}$, or the overriding plate age, $t_{\mathrm{upper}}$, or the side-plate age, $t_{\mathrm{side}}$. Reference mantle temperature $T_0$ in Eq. 6.1 is again fixed at 1623K, and $\kappa$ is thermal diffusivity. On the domain's front and back faces ($z = 0$ and $z = z_{\mathrm{max}}$), in addition to its base, a zero heat-flux boundary condition is prescribed. Eq. 6.1 defines initial conditions, with $t_{\mathrm{plate}} = t_{\mathrm{upper}}$ imposed where $z <= 0$, and $t_{\mathrm{plate}} = t_{\mathrm{side}}$ elsewhere.

Mechanical boundary conditions at the model's sides are the following: A horizontal velocity equal in magnitude to subduction velocity (5 cm yr$^{-1}$), is applied at the incoming plate surface, at $x = x_{\mathrm{min}}$, in the x-direction. At interfaces with the upper and side plates, at $x = x_{\mathrm{max}}$, no-normal flow boundary conditions are enforced down to a depth where temperature reaches locally a nominal value of 99% of mantle temperature. The remainder of the vertical surfaces at $x = x_{\mathrm{min}}$ and $x = x_{\mathrm{max}}$ is stress-free. Free-slip boundary conditions are prescribed at the domain's front and back faces ($z = 0$ and $z = z_{\mathrm{max}}$). At the bottom of the model, velocity equal to the subduction velocity is prescribed at the base of the wedge, slab and sub-slab regions, while a stress-free boundary condition is specified for other basal surfaces. At the domain's upper surface, velocities are prescribed to subduction velocity above the downgoing plate region, or zero velocity at the top of the overriding and side plates. The latter are free to evolve self-consistently in response to local thermal structures and flow-fields [e.g. Kelemen et al., 2003], aside from at their top surfaces, where a no-slip boundary condition is imposed. In addition, in the upper plate, velocities are fixed to zero to a depth of 80 km in a curved prism-shaped region in the wedge, above the subducting plate. Slab and wedge are fully coupled below this depth, as in the *D80* model of Syracuse et al. [2010]. This setup ensures the presence of the 'cold nose', which we noted is necessary for consistency with observational constraints ([e.g. Kincaid and Sacks, 1997, Rychert et al., 2008]).

To simulate trench retreat, we use a down-going plate centred reference frame, and add a horizontal velocity equal to minus the slab rollback velocity to the mantle velocities at the model's base. In these cases, we start the models from a flow field for an equivalent run without trench retreat, and prescribe as a Dirichlet boundary condition that flow field minus trench retreat at the domain's base. As the domain only comprises the upper 400 km of the mantle this boundary condition is sufficient to mimic the effects of lateral migration of the slab. It does not include potential effects of slab steepening, which may accompany trench retreat [e.g., Griffiths et al., 1995, Bellahsen et al., 2005, Capitanio et al., 2007].

We define as time $t = 0$ the time when the model has initialised to the point where the thermal signature of the downgoing plate has been advected to 400 km depth. The models from the previous chapters showed that the style of wedge flow was relatively stable after $t = 10Myr$. We analyse results in the $t = 10 - 30$ Myr time window.

Material properties are as summarised in Table 5.1 in section 5.3. Exactly the same rheological laws for composite diffusion and dislocation creep are used. Most cases in this chapter feature a dry rheology. Hydrous rheological parameters are only used for a few cases with a hydrated wedge corner. Please refer to sections 4.3.2 and 5.3.2 for more details on the model's material properties.

### 6.3.2 Model Cases

| $\tau_{\mathbf{upper}}$ (Myr) | $\tau_{\mathbf{side}}$ (Myr) | $\mathbf{v}_{\mathbf{rollback}}$ (cm yr$^{-1}$) | $\mathbf{C}_{\mathbf{OH,corner}}$ (H/10$^6$Si) |
|---|---|---|---|
| 50 | 50 | 0 | 0 |
| 50 | 50 | 3 | 0 |
| 50 | 120 | 0 | 0 |
| 50 | 120 | 3 | 0 |
| 50 | 120 | 9 | 0 |
| 50 | 120 | 0 | 5000 |
| 50 | 120 | 9 | 5000 |

***Table 6.1:*** *Summary of models presented herein. For each, upper plate age $\tau_{upper}$, side plate age $\tau_{side}$, rollback velocity $\mathrm{v}_{rollback}$ and hydration of the wedge corner $\mathrm{C}_{OH,corner}$ are given. We note that subduction velocity, $\mathrm{v}_{subd}$, and side-plate surface velocity, $\mathrm{v}_{side}$, are 5 cm yr$^{-1}$ and 0 cm yr$^{-1}$, respectively, for all models.*

To focus the analysis on the impact of a slab of finite width, and trench retreat on the mantle wedge's flow-field and thermal structure, in this chapter we do not vary slab parameters. Slab dip (50° for all models), subduction velocity (5 cm yr$^{-1}$), and slab age (50 Myr at trench), are kept constant to representative values of subduction zones on Earth [e.g. Lallemand et al., 2005, Seton et al., 2012]. Subducting-plate width is fixed at 1500 km (although we only simulate its half-width, with mirror boundary conditions at its mid-plane). We also maintain a young upper-plate age (50 Myr), and rather examine the effect of variations in side-plate age, either equal to upper-plate age (50 Myr), or considerably older (120 Myr), which introduces a step in lithospheric thickness. We study cases without rollback (v$_{rollback}$ = $0$ cm yr$^{-1}$), with intermediate retreat velocities (v$_{rollback}$ = $3$ cm yr$^{-1}$), and with strong retreat velocities (v$_{rollback}$ = $9$ cm yr$^{-1}$) [e.g. Lallemand et al., 2005, Seton et al., 2012].

Although we demonstrated the central role of viscosity in wedge dynamics in the previous chapters, in this preliminary study we keep the mantle dry to concentrate on slab edge effects. For only two cases do we prescribe a 'very-wet' wedge corner ($C_{\mathrm{OH}} = 5000$ H/$10^6$Si, an end-member of subduction zone hydration, [e.g. Karato, 2003, Katz et al., 2003]), out to a horizontal distance of 150 km (in the x-direction) from the leftmost apex of the wedge. Other studies utilized this kind of set-up to approximate localised mantle hydration due to volatiles expelled from the slab [e.g. Honda and Yoshida, 2005]. For these two cases, we start from the 120 Myr old side plate case with no retreat. As the thermal signature of the subducting plate has reached the bottom of the domain, we hydrate the wedge at horizontal distances up to 150 km from its apex at 80 km depth (where slab-wedge coupling is turned on), and continue the model run.

Using this set of seven models (Table 6.1), we investigate the effect of (i) finite slab width, (ii) slab rollback, and (iii) wedge corner hydration on wedge flow fields and temperatures.

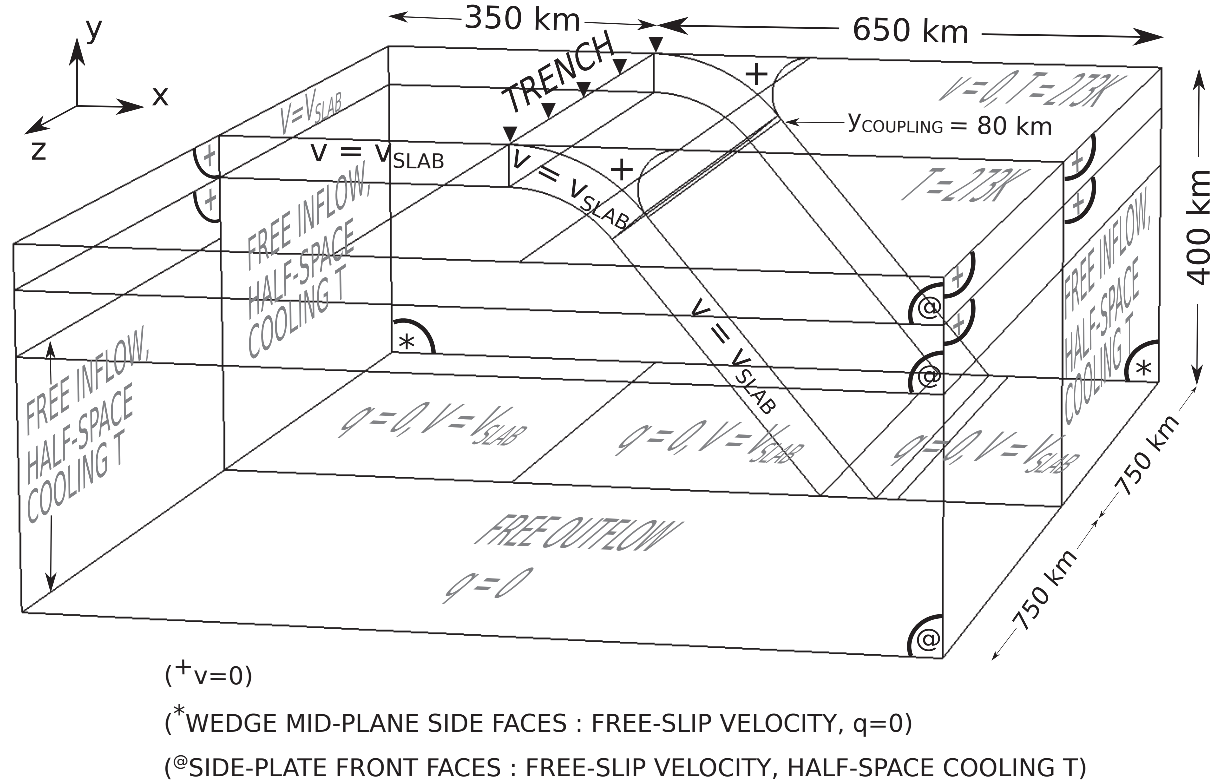

***Figure 6.1:*** *Model set–up to simulate 3-D subduction dynamics: the domain is 400 km deep, 1000 km wide in the transverse (x-)direction, and 1500 km wide in the longitudinal (z-)direction. It is divided into 3 regions: (i) the prescribed down-going plate, where* $V = V_{SLAB}$*; (ii) a prescribed rigid forearc corner, where* $V = 0$*; (iii) a prognostic volume, comprising the sub-slab, wedge and side mantle regions. Temperature is prognostic throughout the computational domain. The subducting slab curves to a constant dip angle of* $50^\circ$ *at 75 km depth, and is fully coupled to wedge flow below 80 km depth. Velocities are fixed along the top and side of the overriding and side plates. Slab velocity is prescribed at the bottom of the wedge and sub-slab volumes. Velocities are free on other boundaries, except the vertical surface in front of the side mantle, where a no-slip condition is enforced. Temperature boundary conditions follow a half-space cooling relationship everywhere, except at the model's base and sides, where a zero heat flux boundary condition,* $q = \frac{dT}{dn} = 0$*, is enforced. Slab rollback is optionally turned on via summation of the current flow at the boundary and a velocity equal and opposite to retreat velocity, as a Dirichlet boundary condition enforced everywhere at the bottom of the domain. This method maintains the reference frame centered on the down-going slab.*

## 6.4 Incorporating a Slab Edge - Effect of Finite Width

In our 2-D models and 3-D models with infinite slab width, cases with a dry rheology yielded a stable corner flow pattern in the wedge below the upper plate. Without any complexities of SSC, this dry case allows us to characterise the basic effect of introducing a slab edge.

### 6.4.1 Impact on Flow-Field

Fig. 6.2 displays horizontal slices of the flow field at 200 km depth, i.e. well below the surface plates, for cases with a 50 Myr old side plate. As expected, flow around the slab edge develops, and this flow is enhanced in magnitude and extent when the slab retreats (Fig. 6.2 *left panels*). To obtain a better view of the flow around the slab edge we display the magnitude of the vertical component of vorticity in (Fig. 6.2 right panels), expressed as:

$$\boldsymbol{\omega}_y = \frac{d\boldsymbol{v_x}}{d\boldsymbol{z}} - \frac{d\boldsymbol{v_z}}{d\boldsymbol{x}}, \tag{6.2}$$

where $\boldsymbol{\omega}_y$ is the vertical vorticity of velocity vector field $\boldsymbol{v}$.

The corner flow induced by subduction of a plate of infinite width (Fig. 6.2a), is fully 'poloidal', i.e. irrotational, with zero vertical vorticity. For a plate of finite width, the flow acquires a 'toroidal' component, where the subducting slab edge acts as a pivot for flow rotation. Toroidal flow is, by definition, characterised by a significant non-null vertical component of vorticity. We obtain values in the order of $10^{-2}$-$10^{-3}$ $\mathrm{s}^{-1}$, a magnitude that is comparable to vorticity found in numerical models of dynamically evolving slabs [Stegman et al., 2006].

The vertical vorticity field allows us to examine the scale of the flow cells around slab edge. For the case without trench retreat, at 200 km depth, the toroidal cell extends up to 250 km around the slab-edge, and additionally for about 650 km into the wedge in z-direction (Fig. 6.2b). Slab rollback of 3 cm/yr increases the radius of influence by an additional ca. 100 km, but does not substantially enlarge the penetration of the flow into the wedge (Fig. 6.2c) (although this extent is possibly affected by model dimensions). The stronger toroidal nature of the flow under the effect of trench retreat thus enhances the volume of mantle which can be fed from the sub-slab and side mantle region to the wedge. The effects of slab retreat will be examined further in Section 6.5.

To further analyse the flow around the slab edge, we show the individual components of velocity in Fig. 6.3, at 100 km and 200 km depth, for the case without retreat and a 50 Myr old

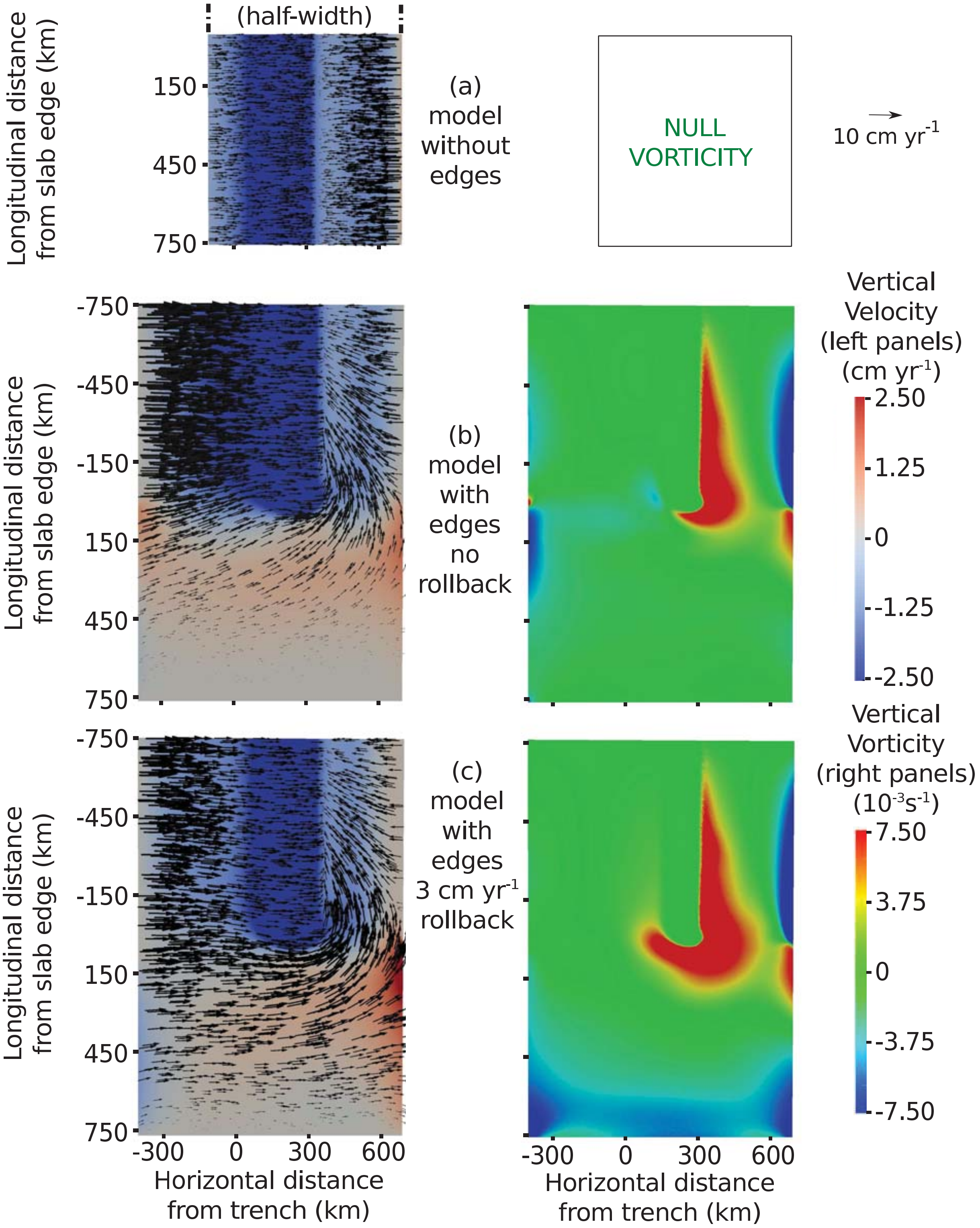

*Figure 6.2: Vertical velocity superimposed by vectors of horizontal velocity, and vertical component of vorticity for young side plate cases, with (a) infinite slab width (as in chapter 5, only half-width displayed), (b) finite slab width and no slab rollback, and (c) finite slab width and 3 cm yr$^{-1}$ retreat, at 200km depth. We omit the null vertical component of vorticity in (a).*

side plate. At 200 km depth, the horizontal velocity components are affected up to 400 km from the slab edge. Note that most flow is brought in from below the side plate, and relatively little from below the slab.

The influence of flow around the edge is much more limited at shallower depths where flow is slowed down by the higher viscosities at the base of the lithosphere. At 100 km depth, the toroidal cell for the case without trench retreat only extends about 100 km around the edge, and the flow into the wedge does not penetrate more than 250 km in the z-direction into the wedge. This is significant as it is at depths of 100 km or less where mantle temperatures approach (wet/damp) melting temperatures most closely, and where small changes in flow could affect melt conditions. It is also noteworthy that there is little vertical component to flow around the slab side, as this is limited by the side and upper plates. Additional vertical flow might further enhance melting by bringing warmer material to shallower depths.

In this context, we note that a noticeable component of flow is observed in the trench-parallel direction, from the side mantle towards the sub-slab volume (Fig. 6.3f). Its presence is a consequence of differential thickness between the conductively thickening side plate and the subducting plate, which in the model instead presents the same age of 50 Myr at the trench throughout model evolution. The positive anomaly in vertical velocity observed close to the left side boundary in Fig. 6.3c,e is likely a boundary effect, related to the change in plate thickness and velocity boundary condition at that edge.

### 6.4.2 Impact on Temperature

Snapshots of the thermal structure in Fig. 6.4 show that, in contrast to the effect of the slab edge on flow, the impact on temperatures manifests itself mostly at shallower depths (Fig. 6.4(a,c)). Notably, toroidal flow around the slab smears the neighbouring mantle cooled by the slab edge, leading to the formation of a cold ’ridge’, or ’hook’. This feature appears as an extension of the slab’s thermal signature beyond the edge, at a sharp angle in the positive x-direction.

The formation of such a cold ’tail’ at the edge of the slab is likely a robust feature of thermal models. In a similar fashion, if the slab could dynamically develop an along-strike curvature [as in models of e.g., Morra et al., 2006, Schellart et al., 2007], the toroidal flow would also act to bend the slab upon subduction, resulting in a convex slab shape, and hence a smoother hook. In our models, at a shallow depth of 100 km, this colder ridge induces a drop of up to 50 K in wedge corner temperatures within the toroidal flow cell at x=250 km (compare with Fig. 6.3c). Consequently, the hook shields a significant volume of the wedge corner closest to the edge from the around-edge flow. The interaction between the toroidal flow cell, and the corner-flow dragged by the slab below the upper plate, results in a locally weaker erosion of the upper plate there where these flows converge. Nevertheless, these effects diminish at larger depths (e.g. 200 km as in Fig. 6.4b,d).

The warmest temperatures observed in Fig. 6.4c are however obtained at the boundary between the subducting and side plates. At the model boundary, this temperature anomaly may be overestimated due to the artificially large Vz component. However, some component of flow from below the conductively thickened side plate and towards the sub-slab region (Fig. 6.3c,e,f) is robust, and result in the locally high temperatures below the edge of the downgoing plate.

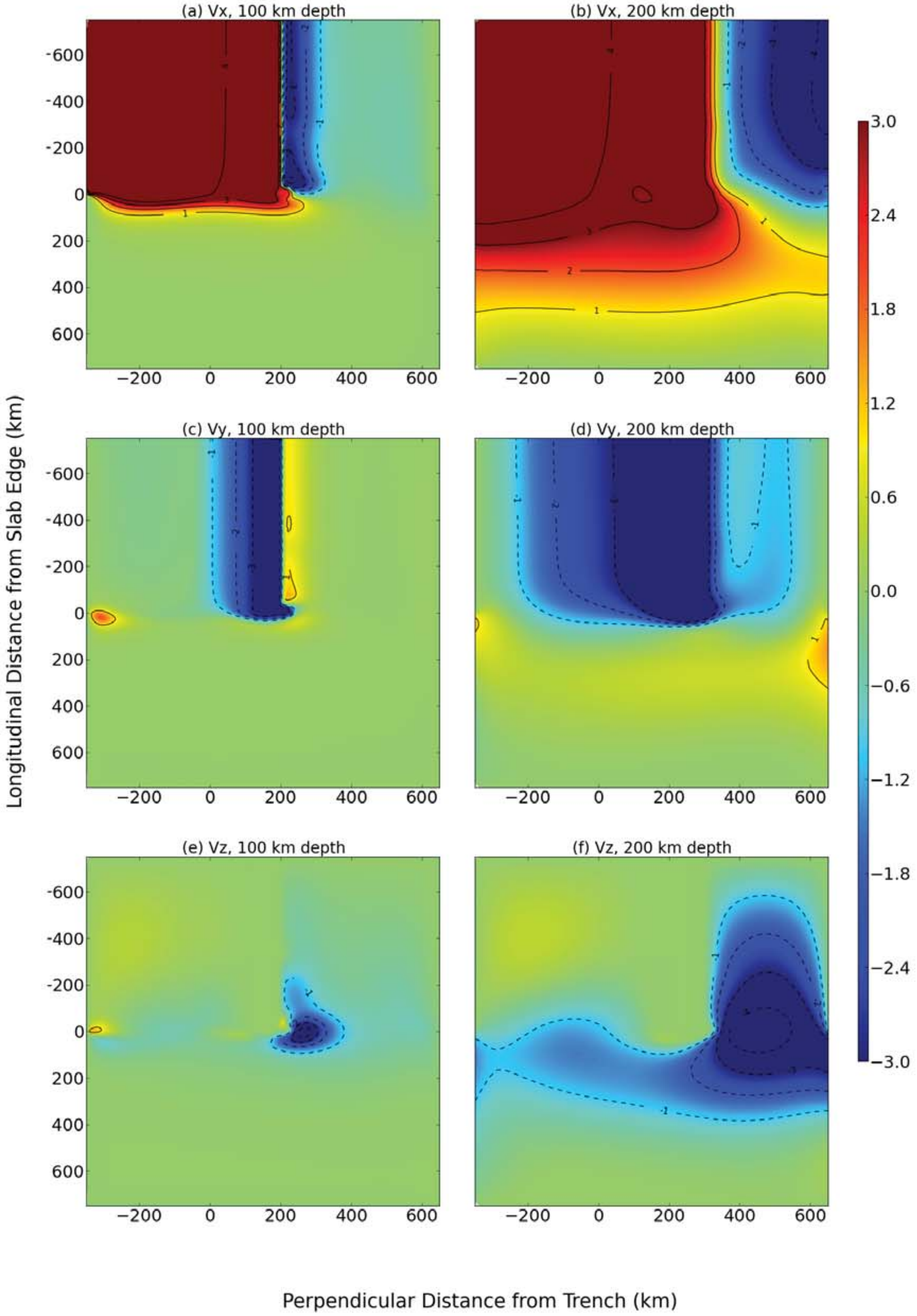

***Figure 6.3:*** *Velocity components at 30 Myr and (a,c,e) 100 km and (b,d,f) 200 km depths, for cases with finite-width subducting plate, 50 Myr old side plate and no trench retreat. Velocity components in the (a-b) transverse (x-)direction; (c-d) vertical (y-)direction; (e-f) longitudinal (z-)direction are shown.*

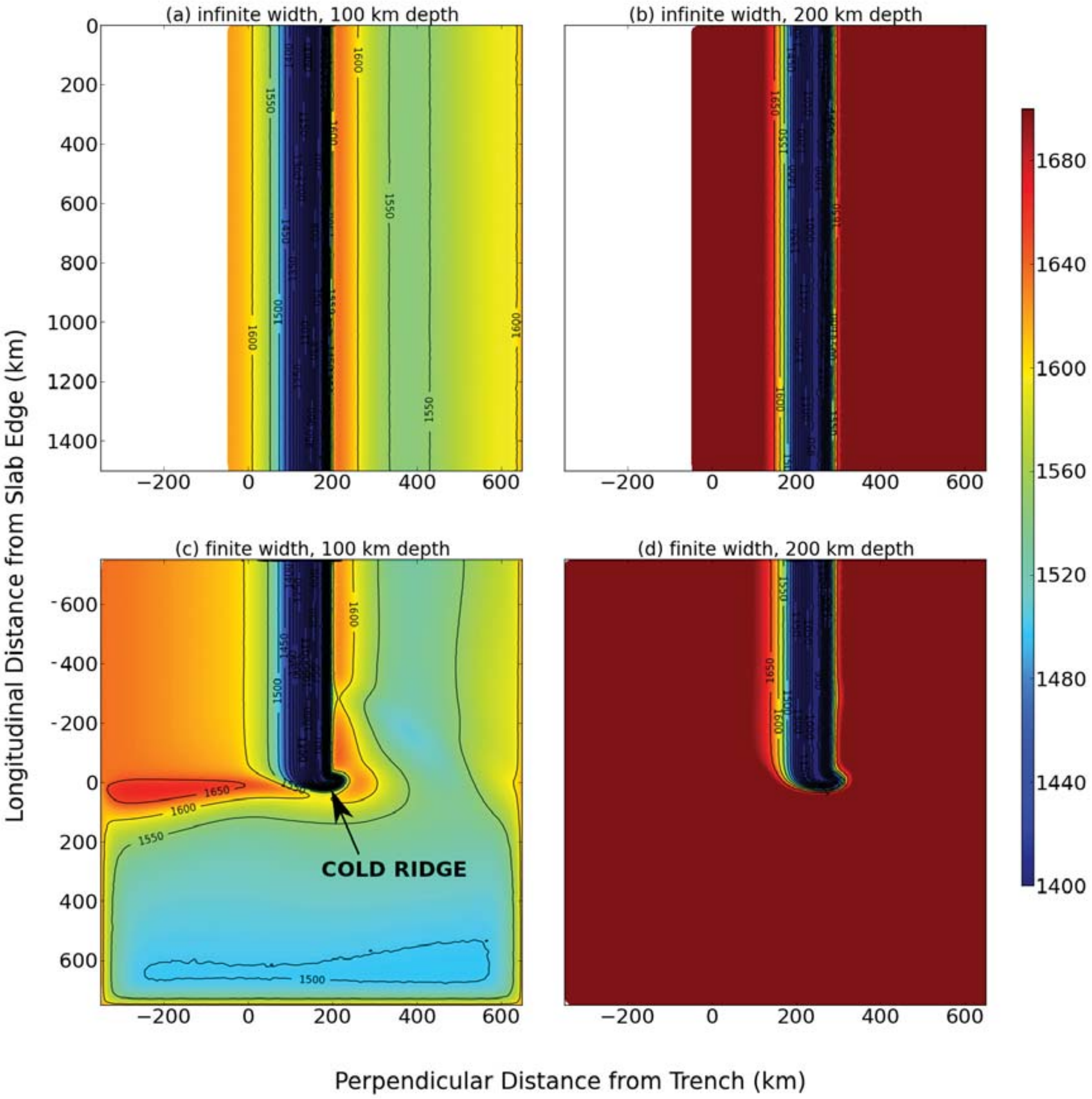

*Figure 6.4: Temperature field at 100 km and 200 km depths, for cases with (a,b) infinite and (c,d) finite slab width, at a simulation time of 30 Myr.*

### 6.4.3 Side-Plate Age

A higher side-plate age than the age of the upper plate introduces a differential thickness between these two plates. We show the effect on flow field and temperature at 100 km depth in Fig. 6.5. At 200 km depth, flow and temperature for cases with an old and with a young side plate are very similar. However, at 100 km depth, for the colder side plate, flow around the slab edge further stretches the 'hook' in the positive x-direction, by ca. 100km. The thicker side plate and longer cold hook largely block flow from below the side plate into the wedge and thereby increase the radius of the toroidal cell. Some back flow (positive Vz in Fig. 6.5b) consequently develops into the wedge corner behind the hook. The result is lower temperatures in the wedge corner next to the slab edge than in the case with a younger side plate, by up to 100K within a 200 km range inside the wedge.

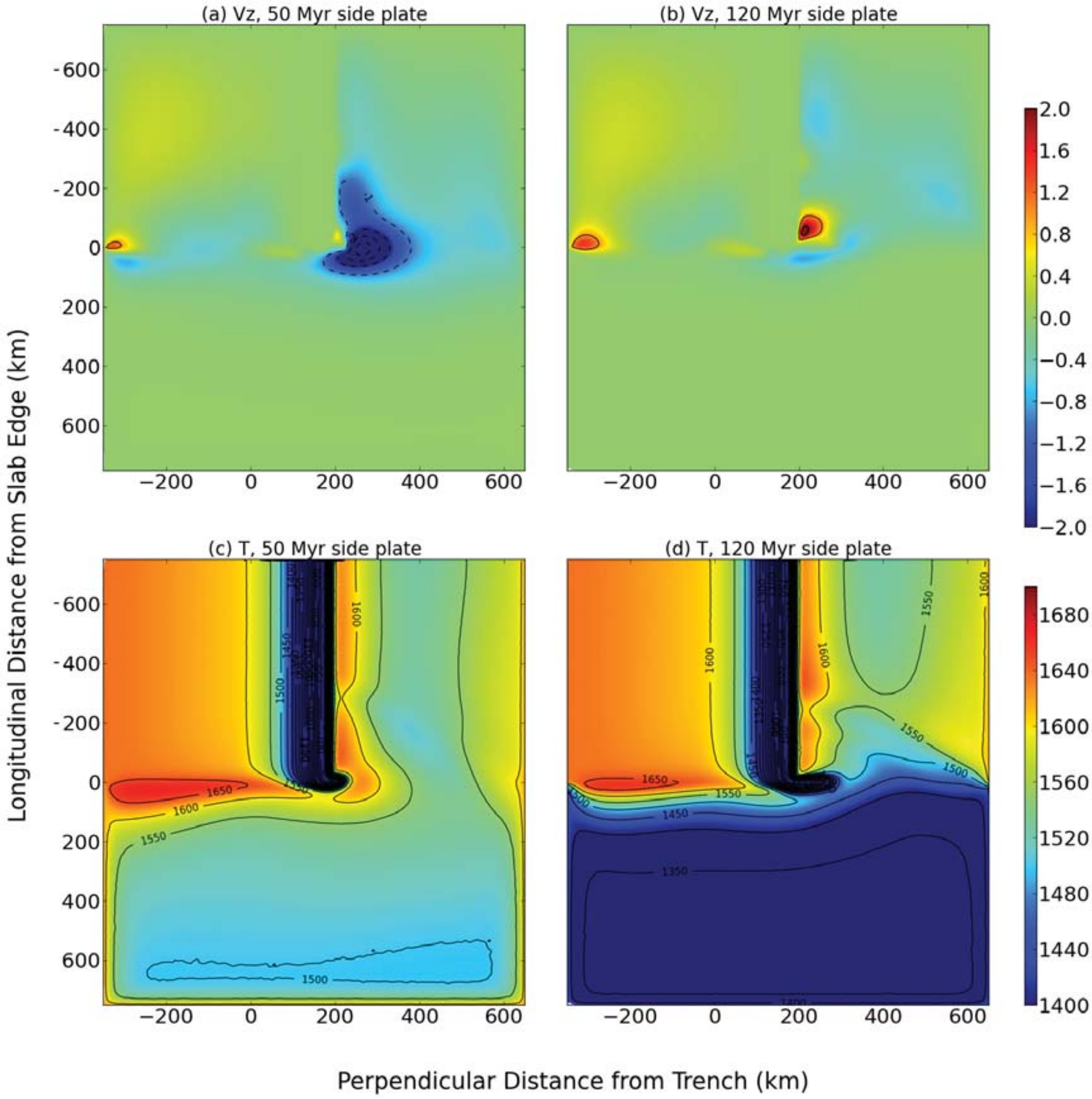

*__Figure 6.5:__ Horizontal, longitudinal (z-)component of flow and thermal structure at a simulation time of 30 Myr, for cases with a (a,c) 50 Myr old, and (b,d) 120 Myr old side plate, at 100 km depth.*

## 6.5 Slab Rollback

We further explore the effect of slab rollback for three cases with a 120 Myr old side plate. Fig. 6.6 shows the longitudinal velocity components; transverse (Vx) and vertical (Vy) velocities are much less affected. Because the effect of retreat velocity on toroidal flow at shallow depths is lower than at deeper levels, a smaller range of the colour scale is used in Fig. 6.6a,b,c than in panels d,e,f. At both 100 and 200 km depth, we now see that the trench-parallel component of sub-slab flow is considerably enhanced in the fast retreat case ($v_{rollback}$ = $9$ cm yr$^{-1}$). At 200 km depth, subslab flow reaches magnitudes comparable to the Vz component into the mantle wedge. At 100 km depth, longitudinal flow into the wedge is barely enhanced by trench retreat and the back flow behind the cold 'hook' remains.

There is an effect of trench retreat on temperature at 100 km as well as at 200 km depth (Fig. 6.7). Note again, the different colour scales for the two depths, chosen to highlight temperature features at the respective depths. Although the change in toroidal flow at 100 km depth with increased retreat velocity is small, it is sufficient to increase the drag of some cold mantle into the wedge region. For the fastest rollback case, this results in a local depression of maximum wedge temperatures by about 50 K at a distance 200 km away from the slab edge. At 200 km depth, a swirl of colder material from the thicker side plate also develops in the fastest retreat case, although here the anomalies are only 10-20K.

Looking at Fig. 6.7, the effect on corner temperatures appears subtle, however, Fig. 6.9(a,c,e) illustrate that the temperature variations are sufficient to affect where wet melting is possible. Although the rheology used is for a dry mantle, the local presence of water might allow wet melting. For an infinite slab, wet melting is possible between about 90 and 100 km depth, when temperatures are higher than ca. 1620 K. The colder ridge that develops due to convergence of flow around the slab edge with wedge corner flow suppresses this wet melt at a distance of about 250 km from the slab edge, irrespective of the age of the side plate. For the cases with the old side plate the changes in flow due to slab retreat move the location where melting is suppressed.

The effect of flow changes due to slab retreat on temperature are not as pronounced when the side plate is younger (Fig. 6.8). The reason is two-fold, as in these models (i) the colder hook does not extend as far as for old side plate cases, and the toroidal flow can more readily enter the wedge corner with less, or no, trench retreat, and (ii) differential thickness between the upper and side plates is null, so that wedge mantle and side mantle have similar temperatures and viscosities. Indeed, Fig. 6.9(b,d) show that there is little shift of the regions where wet melting is possible between the case with and without retreat. However, the presence of a slab retreat enhances toroidal flow sufficiently to somewhat thin the side plate, creating the conditions for wet melting below it, 50-100 km away from the edge, at the same depth as below the overriding plate.

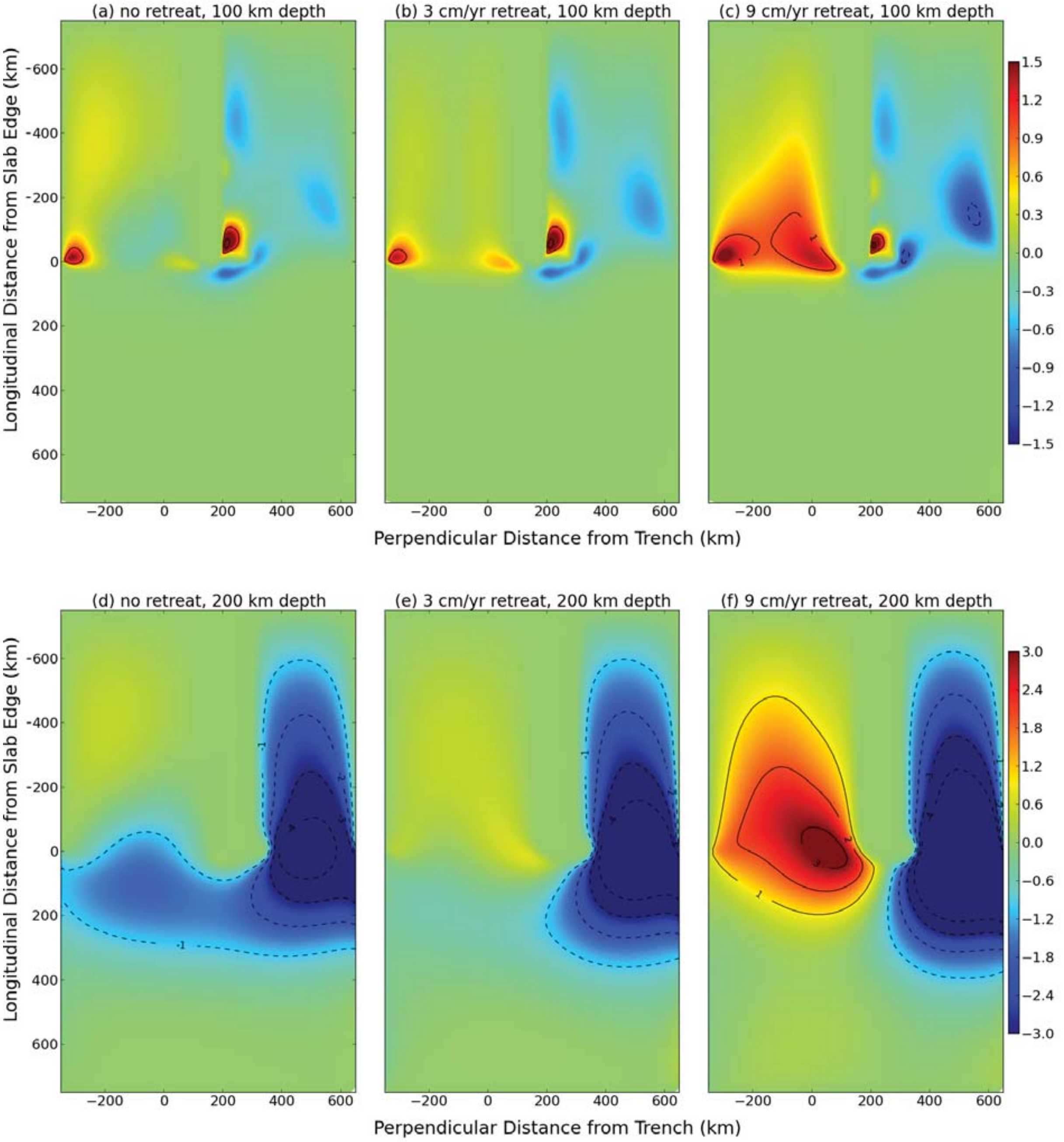

***Figure 6.6:*** *Horizontal, longitudinal (z-)component of velocity at a simulation time of 30 Myr, for cases with (a,d) no slab rollback, (b,e)* $\boldsymbol{v_{rollback}} = 3$ *cm* $yr^{-1}$ *and (c,f)* $\boldsymbol{v_{rollback}} = 9$ *cm* $yr^{-1}$*, and a 120 Myr old side plate. Panels (a-c) are snapshots at 100 km depth, (d-f) at 200 km depth. At shallower depths, the effect of retreat velocity on toroidal flow is lower than at deeper levels. A smaller range of velocities is accordingly used on panels (a-c), in order to capture the increase in magnitude of Vz in the proximity of slab edge when rollback is stronger.*

## 6.6 Wedge Corner Hydration

In chapter 4, we investigated the effect of localized hydration at the wedge corner. We found that edge instabilities were spawned at the intersection between the dry (or damp) mantle and the hydrated section of the corner, which caused small-scale convection in this area. In a 3-D

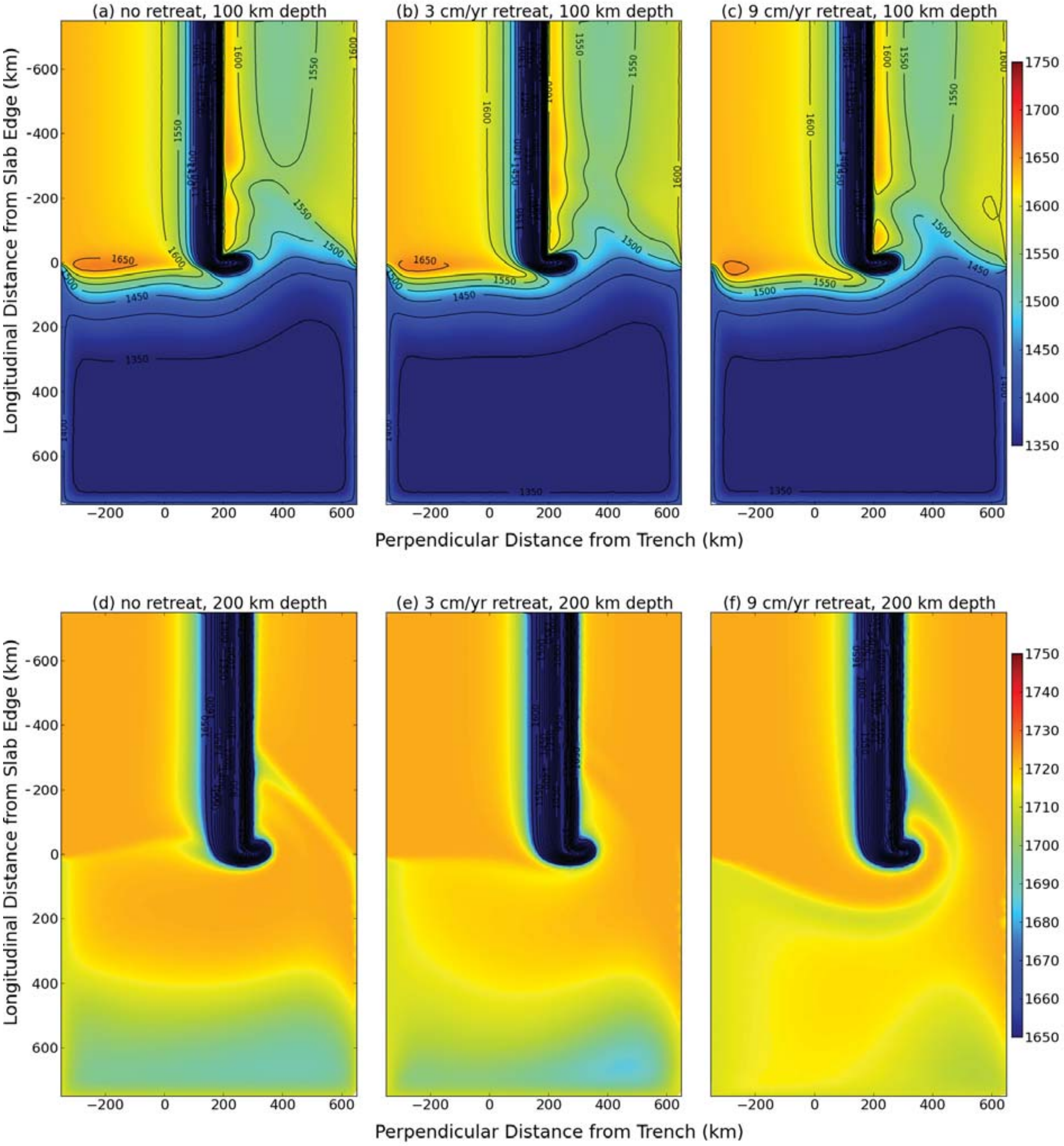

*__Figure 6.7:__ Thermal structure at a simulation time of 30 Myr, for cases with (a,d) no slab rollback, (b,e) $v_{rollback}$ = 3 cm yr$^{-1}$ and (c,f) $v_{rollback}$ = 9 cm yr$^{-1}$, and a 120 Myr old side plate. Panels (a-c) are snapshots at 100 km depth, (d-f) at 200 km depth.*

infinite-width case where the whole wedge was strongly hydrated, SSC rolls formed below the arc region with wavelengths of 50 to 200 km. For a 3-D finite-width slab, with either null or strong slab rollback, we find that the patterns of SSC are significantly affected by flow around the slab's edge.

Fig. 6.10 shows the horizontal flow-fields at 100 km depth, at a simulation time of 30 Myr. A strong pressure gradient develops within the hydrated wedge corner, as the toroidal flow

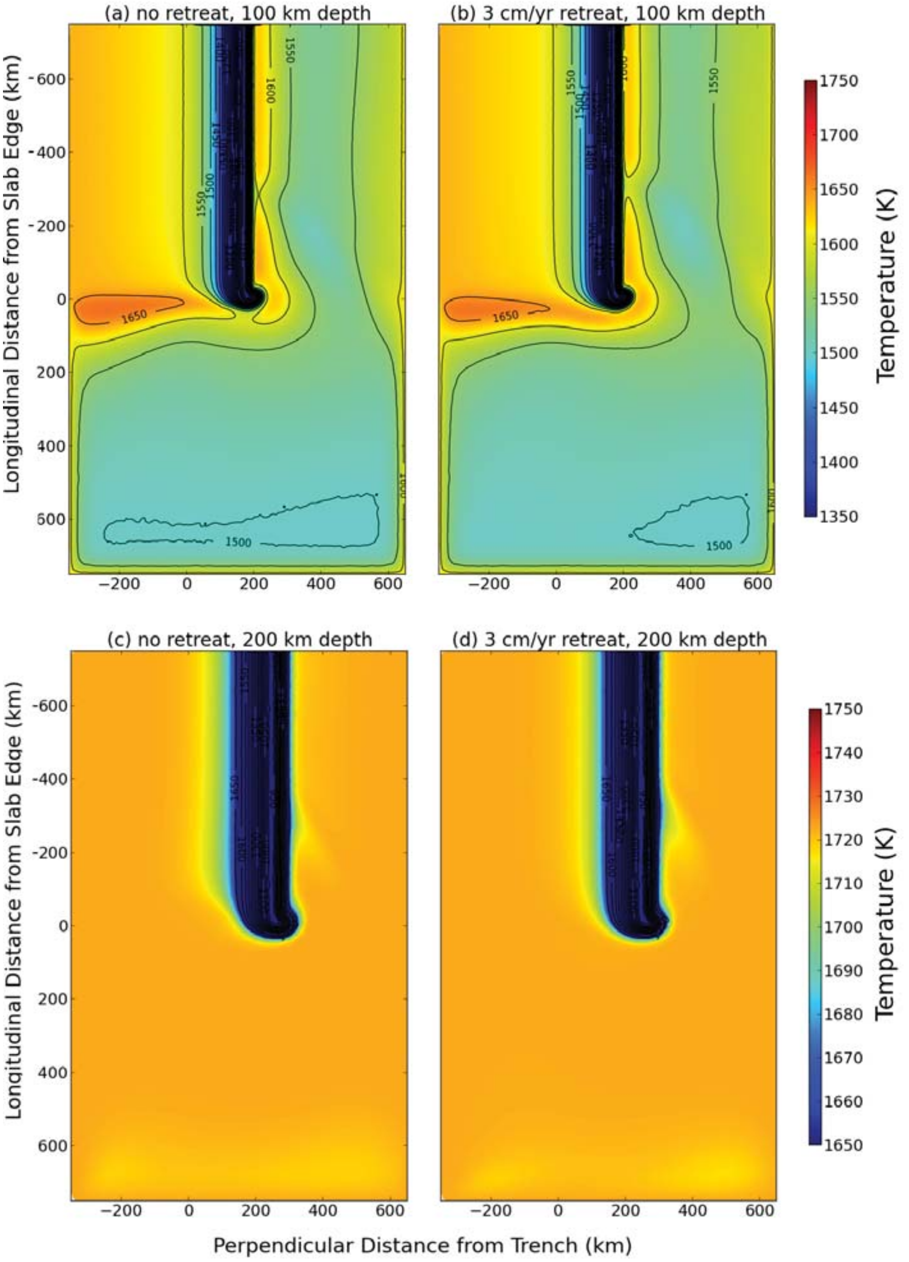

*Figure 6.8:* *Thermal structure at a simulation time of 30 Myr, for cases with (a,c) no slab rollback, or (b,d)* $v_{rollback}$ *= 3 cm* $yr^{-1}$*, and a 50 Myr old side plate. Panels are snapshots at (a-b) 100 km depth, and (c-d) 200 km depth.*

draws the side mantle towards the low-viscosity wedge. This gradient very efficiently channels a trench-parallel flow into the wedge, to the extent that the longitudinal component reaches higher speeds than subduction velocity (see Fig. 6.10(b,d)). Only a small amount of back flow develops, which penetrates the corner behind the cold hook. For the finite-width slab, we find that the strong along-strike flow observed leads to larger-scale Richter rolls with z-dimensions of 200-400 km. However, the patterns of SSC are highly time-dependent, as is the structure and development of edge instabilities, and the positioning of high- and low-temperature areas

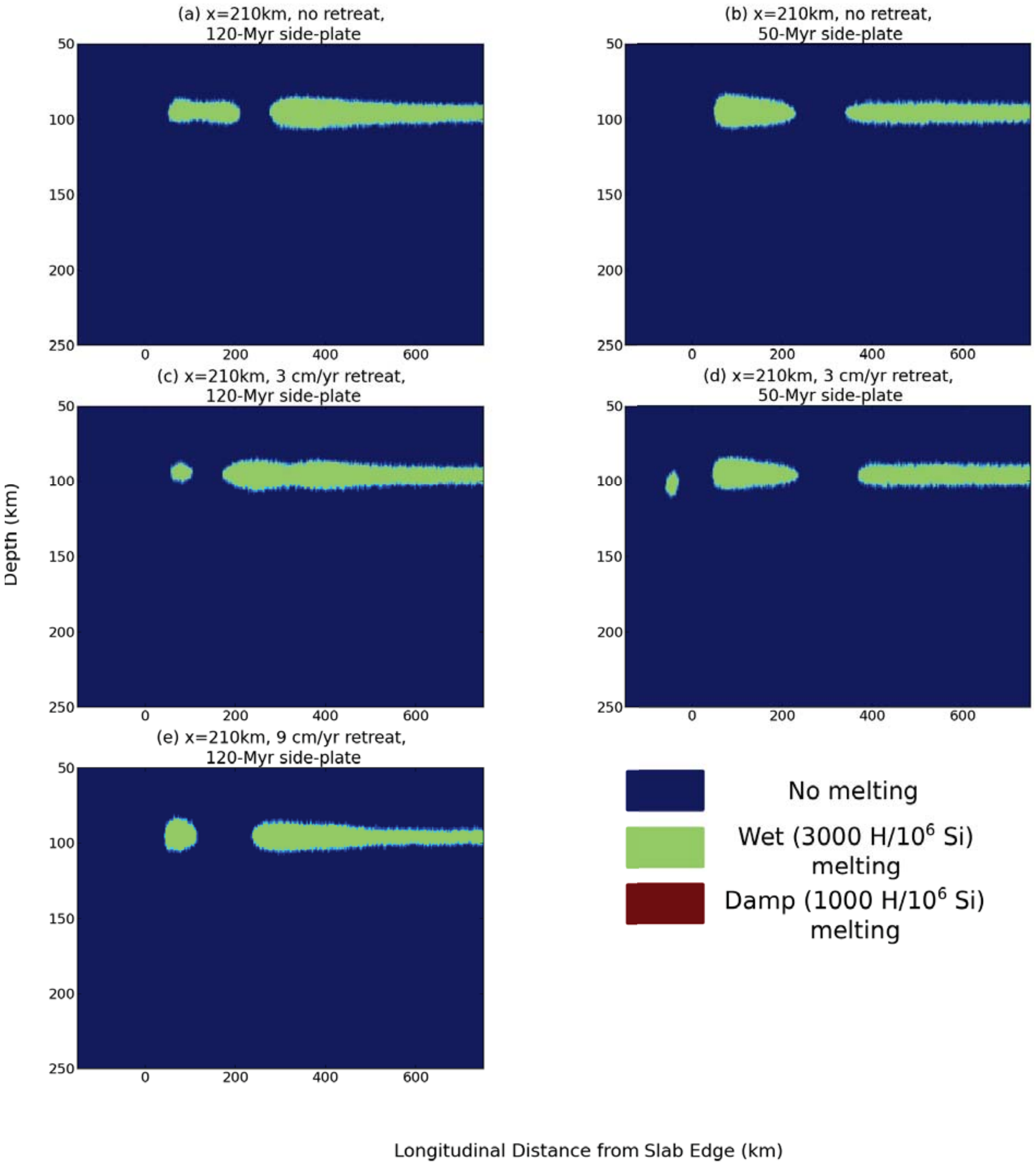

***Figure 6.9:*** *Areas where damp and wet solidi for a mantle of MORB composition are crossed at a horizontal distance of 210 km from trench, for cases with (a,c,e) 120 Myr old and (b,d) 50 Myr old side plates.*

are notably transient, more so than in the wedge of an infinite-width plate (see chapter 5). Just near the slab edge, the flow fixes the position of a SSC cell. As this flow is so strong, it is not significantly affected by trench retreat.

The overall effect of corner hydration on thermal structure is a significant increase in temperatures (by up to 100K, see Fig. 6.10). In the 3-D infinite width models, we also found such increases in wedge corner temperatures, due to stronger erosion of the upper plate. The thinner upper plate significantly enhances the region where melt is possible (Fig. 6.11), now not only under wet but also damp conditions, and one melt region occurs next to the slab edge, while the other melt regions migrate through time and with increasing retreat velocity.

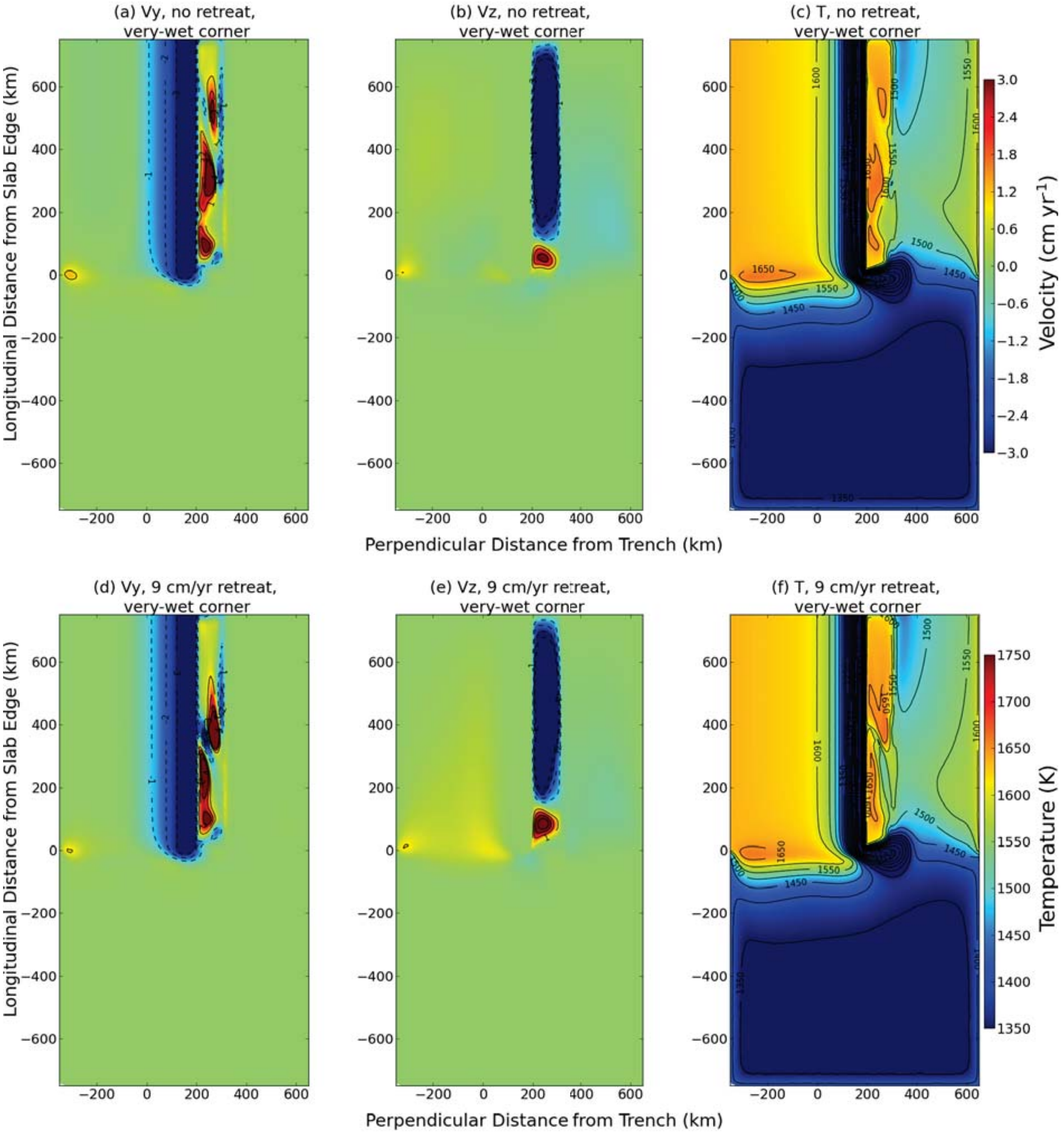

***Figure 6.10:*** *Snapshots at 100 km depth for cases with (a-c) 0 and (d-f) 9 cm/yr rollback velocity, and a dry mantle but very-wet (5000 H/10$^6$Si) hydration inside a 150 km horizontally-wide area sub-arc in the wedge corner. Panels show (a,d) vertical velocity Vy, (b,e) longitudinal velocity Vz and (c,f) temperature for each case. Here shown are snapshots taken 30 Myr after that time.*

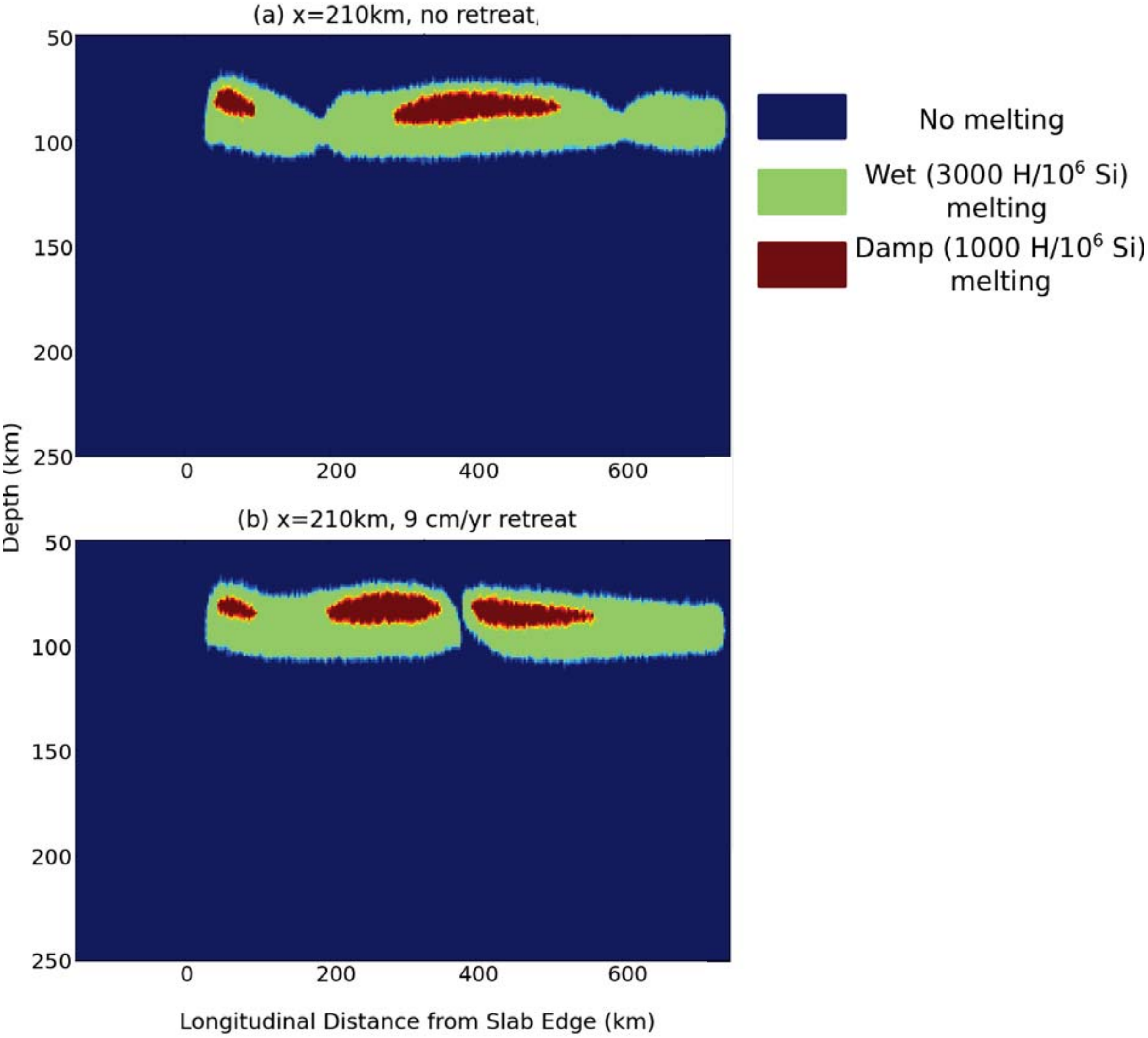

***Figure 6.11:*** *Areas where damp and wet solidi for a mantle of MORB composition are crossed at a horizontal distance of 210 km from trench, for cases with a very-wet corner and a 120 Myr old side plate, (a) with and (b) without, trench retreat.*

## 6.7 Discussion

The models presented only constitute a preliminary investigation into the effect of finite slab width and flow around its edges on mantle wedge velocity and temperature fields. In this section, we discuss some of the models' limitations and suggest avenues for further work, as well as some potential implications of our results.

### 6.7.1 Model Limitations

**Hydrated vs. Dry Wedge Rheology**

The 3-D model cases examined herein simulated wedge flow dynamics and the evolution of the thermal structure under the effect of buoyancy and a dry mantle rheology. However, the upper mantle is likely 'damp' ($C_{OH}$ = 1000 H/$10^6$Si), and at subduction zones, at least locally even wetter [e.g. Hirth and Kohlstedt, 1996]. In chapters 4 and 5, we found that hydration of the mantle wedge exerts a dominant control on flow dynamics, where viscosities below $5 \cdot 10^{18}$ Pa s systematically promote SSC. Given these results, it would be good to model additional cases including some with a damp rather than dry background mantle, and models where wedge hydration extends over larger distances from the wedge corner. Such models will be necessary to investigate what controls the strength of along-strike flow into the wedge that we found in the cases with a strongly hydrated wedge corner, and how the flow around the slab edge interacts with different styles of wedge SSC.

**Influence of Side Plates**

Most previous models that have investigated flow around the slab edge have not included any side plates. Our results above show that it can affect flow into the wedge, in particular in the corner region where melt and dehydration most likely occur. With increased mantle hydration, any steps in thickness between side plate and upper plate would likely nucleate additional instabilities [see results in chapter 4 and Dumoulin et al., 2005] which will affect near-slab-edge wedge flow.

A differential thickness develops in our models below the boundary between the stationary side plate and subducting plate, causing a noticeable upward, trench-parallel component of flow from the side mantle and below the subducting plate. The interaction with the side plate may be somewhat different if it moved with the down-going plate, rather than with the upper plate as modelled here. This alternative scenario is one of the most common configurations for trench retreat on Earth (e.g., Tonga, New Hebrides, South Sandwich, Antilles, Calabria), where a tear develops in the down-going plate as only a segment of that plate subducts [Govers and Wortel, 2005]. In this case, the component of flow which here lead to high temperatures beneath the boundary between the subducting and side plates, would be substantially suppressed. However, we would expect an increase in the strength of toroidal flow around slab edge, as the hot mantle below the side plate would directly be pulled in the positive x-direction, possibly contributing to a significant extension of the areas where suitable conditions for melting are met.

### Kinematic vs. Dynamic Trench Retreat

We modelled only a translational component of trench retreat, and we approximated it by moving the reference frame (i.e., the mantle) rather than the subducting plate. In dynamic models [e.g., Griffiths et al., 1995, Bellahsen et al., 2005, Stegman et al., 2006, Capitanio et al., 2007], slabs do not only translate but may also steepen during trench retreat. Slab steepening adds an upward vertical component to the toroidal flow around the slab edge [Kincaid and Griffiths, 2004, Piromallo et al., 2006], which will enhance wedge temperatures more than occurs in the models we presented above. The choice of changing the reference frame and moving the mantle rather than the plate is one that has been previously used in various model setups (e.g., [van Hunen et al., 2002, Conder et al., 2002]). However, because of the different rheology of plates and mantle, our moving of the mantle reference frame may have a more subdued effect on the toroidal flow than movement of the rigid plate would have.

In addition, we approximated our plates as planar, while in dynamic subduction, slab shape will evolve in response to flow around the edges. Depending on plate strength, plate size and lateral variations in buoyancy, along-strike slab deformation may be more or less pronounced [e.g., Morra et al., 2006, Schellart et al., 2007, Faccenda and Capitanio, 2013]. This will affect the development of the cold 'hook' that occurs in our models. In addition, slab shape has been shown to affect flow around and along it [Capitanio and Faccenda, 2012, Faccenda and Capitanio, 2013, Kneller and van Keken, 2008], and will very likely affect patterns of small-scale convection in the wedge as our along-strike flow does in the cases with a locally hydrated wedge.

#### Scale of Toroidal Flow

Our toroidal cells are 250-400 km in radius. Piromallo et al. [2006] inferred that toroidal flow length scale was not affected by slab width but controlled by model depth, in a model representing the upper mantle, where the base was modelled as zero slip. Their cell length scale was about 1/3 of the model depth. On the other hand, models by Stegman et al. [2006] recovered much larger toroidal flow cells, of scales of about 1500 km, in models which included a high viscosity lower mantle but where slabs were confined to the upper mantle. They propose toroidal flow scale to be controlled by mantle viscosity (which was Newtonian in their models). In models by Faccenda and Capitanio [2013], which use a similar set up to Stegman et al. but include dislocation creep in the mantle, the cell scales are several 100 km. Our models only span the upper 400 km of the mantle, and have a partially free and partially fixed outflow base and composite rheology. Toroidal flow in our models occurs on a scale between that of the two studies mentioned above. Further investigation of the scale controls would be warranted, as it affects the distance from the edge to which the mantle wedge is affected.

### 6.7.2 Model Implications

#### Near Slab-edge Melting With and Without Retreat

Kincaid and Griffiths [2003, 2004], based on thermal laboratory models, inferred that slab surface temperatures near slab edges were warmer than in the centre for subduction zones with minimal trench retreat, whereas under significant trench retreat the centreline was warmer than the edges. They infer that the variations are substantial enough to affect where melting is possible, and that this may explain some anomalous near slab edge volcanism [Yogodzinski et al., 2001, Gvirtzman and Nur, 1999]. Our results do not confirm this. This melt region immediately next to the slab edge is not significantly affected by the slab retreat velocities, but rather melting at a distance of 100-250 km from the slab edge can be suppressed by flow around the slab edge (see Figs. 6.9 and 6.11). Actually, the case of Etna [Gvirtzman and Nur, 1999] is quite enigmatic as this volcano is situated trench-ward of the volcanic arc. Govers and Wortel [2005] attribute this type of volcanism to shearing along, and back flow below, a plate boundary that develops between side and upper plates in response to trench retreat. In our models (where upper and side plate move together), shear near the boundary between downgoing and side plate can lead to local plate thinning which may be sufficient to allow melt (e.g., high T at 100 km in Fig 6.5).

**Wedge Anisotropy**

Seismic anisotropy in the mantle is largely attributed to mineral alignment in the direction of mantle flow. An enigma of seismic anisotropy in the mantle wedge is that the fast axis is commonly found to be oriented in the trench-parallel direction, as expected from trench-parallel flow [e.g. Pozgay et al., 2007, Long and Becker, 2010], while alignment in trench perpendicular direction is predicted for typical corner flow [e.g. Kneller et al., 2005]. For one exhumed arc terrane, structural geology observations also indicate that trench-parallel flow conditions may have dominated its mantle wedge [Mehl et al., 2003]. Under conditions where the mantle is cold, hydrous and at high stress, the seismically fast axis may rotate to a direction perpendicular to the largest finite strain (b-type fabric) [Jung and Karato, 2001]. However, such conditions may only prevail in the forearc corner and thus can not explain anisotropy directions further out from the trench [Kneller et al., 2005].

Many studies have investigated other ways of aligning wedge flow in trench parallel direction. Pressure gradients associated with variable slab geometry [Kneller and van Keken, 2008] and upper-plate shear [Hall et al., 2000] have been shown to be able to locally reorient flow directions towards the along-strike direction. Small-scale convection can cause diverse flow directions including trench-parallel ones [Honda et al., 2010, Behn et al., 2007]. Flow around slab sides associated with slab retreat has previously been shown to generate trench-parallel alignment near the slab edges [Buttles and Olson, 1998, Kincaid and Griffiths, 2004]. In our models with a hydrated wedge however, trench-parallel flow extends substantially further into the wedge, enhanced by non-linear rheological feedback once flow channeling into the low-viscosity corner has been initiated. This is possibly an alternative explanation for the anisotropy observations, however, it would be good to validate these results for a wider range of model parameters.

## 6.8 Conclusions

3-D models with a finite-width slab allow the development of toroidal flow around the slab edge. In our models with a dry mantle, the size of the toroidal cell varies from 200 km to 400 km at 200 km depth, without or with trench retreat, respectively. In cases with locally hydrated wedge corners, trench-parallel flow in the wedge may even extend to the slab centerline. Only in the cases with very strong trench retreat was a significant amount of material drawn into the wedge from below the slab. In other cases, the flow into the wedge was mainly sourced from below the side plate.

In the shallow wedge corner, where melting and dehydration conditions are most likely to be met, thermal structure is affected at distances ranging from 100 to 250 km from the slab edge. At about 100 km depth, toroidal flow is capable of shutting down possible areas of melt production in the wedge corner, either because it drags colder material from a thick upper plate or because at the convergence of the toroidal and wedge corner flow upper plate erosion is less efficient. Contrary to suggestions from past studies [e.g. Kincaid and Griffiths, 2004, 2003], wedge temperatures immediately next to the slab edge and hence melting conditions are not significantly affected by trench retreat. Rather, in all cases we investigated, mantle material that has been cooled by the slab is dragged by the toroidal flow to form a cold tail of material extending 50 km to 150 km in the positive x-direction, below the intersection between the upper plate and side plate, which shields the near-edge wedge corner. For a case with a strongly hydrated wedge corner, wedge SSC was significantly modified as along-strike flow into the wedge lengthened cell scale and made it very time dependent, with the exception of the cell nearest to the slab edge.

The side plate exerts a significant control on how flow around the slab's edge can affect the wedge. Thick side plates somewhat shield the shallow wedge corner from trench-parallel flow, locally forcing a stronger component of up-flow which may encourage melting. In addition, the results from the previous chapters lead us to expect the triggering of additional instabilities when there is a difference in thickness between the upper and side plates (in addition to those that form at the base of the overriding plate). These may further affect temperatures and time dependence of the wedge structure.

Additional complexities, like movement of the upper plate, different amounts and extents of mantle hydration and slab steepening during trench retreat will likely further complicate wedge flow and temperature fields and consequently the distribution of melt and dehydration zones.

# Chapter 7

# Conclusions

In this thesis, we have undertaken systematic 2-D and 3-D numerical investigations of the controls exerted by the effects of hydration on viscosity, by thermal buoyancy and by toroidal flow around slab edges on flow regimes and thermal structure of the mantle wedge. We conducted a wide parameter study which shows how the styles of mantle flow vary with velocity, plate age, and especially viscosity. Flexible resolution enhancement within the Fluidity code (here specifically validated for simulating subduction zones against van Keken et al. [2008]'s established benchmarks) allows accurate modelling of unstable small-scale convection (SSC) flow styles.

While other studies have documented the prime importance of viscosity for SSC (here occurring for viscosities $< 5 \times 10^{18}$ Pa s, consistent with [e.g. Honda and Saito, 2003, Arcay et al., 2005, Honda et al., 2010, Wirth and Korenaga, 2012]), we additionally observe that the spatial extent of hydration exerts a strong control on whether SSC is triggered and how efficient it is at thinning the upper plate. If the wedge is hydrated with an amount of water likely characteristic of the upper mantle ($C_{\mathrm{OH}}$ >=1000 H/$10^6$Si), its viscosity is decreased [Karato and Wu, 1993, Hirth and Kohlstedt, 1996], favouring the development of SSC for a wide range of subduction configurations. If the length of potentially unstable lithosphere is less than the wavelength of instabilities initiating at the base of the lithosphere (> 100–150 km for our minimum hydrously-weakened viscosities of $\sim 1 \cdot 10^{18} Pa \cdot s$), our 2-D models remain stable and feature a corner flow pattern common to many previous studies ([e.g. Davies and Stevenson, 1992, Peacock, 1996, Peacock and Wang, 1999, van Keken et al., 2002, Kelemen et al., 2003]).

Notably, our 3-D systems naturally evolve into two distinct, but interacting, systems of SSC in the arc and back-arc regions even without a limitation on the distance to which the wedge is hydrated by the down-going plate. In the sub-arc region, the additional degree-of-freedom permits the development of 3-D longitudinal Richter rolls (with their axes aligned perpendicular to the trench), predicted by theoretical and numerical studies [e.g. Richter, 1973, van Hunen et al., 2003, Honda et al., 2010, Wirth and Korenaga, 2012] and unable to form in the narrow space available in 2-D, with wavelengths of ~50-200 km. In the back-arc system, long, linear and cold ridges spawned at the overriding plate's base and sheared by background corner flow, constitute the downwelling limbs of larger-scale (100-400 km) Richter rolls. The interaction between the two systems is highly time-dependent, and more prominent for higher subduction velocities and for thinner upper plates.

Although our study with an infinite width 3-D slab demonstrates that 2-D models in many ways provide a good approximation to the average of 3-D models, we observe a stronger impact of SSC in 3-D than in 2-D, in terms of upper-plate erosion and wedge temperatures. Strong lithospheric thinning induced by SSC in cases with wet ($C_{\mathrm{OH}}$ >1000 H/$10^6$Si) wedges is predominantly controlled by the level of mantle hydration (viscosity), and just somewhat enhanced by higher subduction velocity. 3-D flows only cause a few additional kilometres of lithospheric erosion, but that considerably enlarges the region over which dehydration and wet melting can occur below both the arc and back-arc. Stronger upper-plate erosion and more vigorous wedge convection for more hydrated wedges yield overall higher slab-surface temperatures (SSTs). Lithospheric instabilities affect wedge temperatures most strongly in the low-velocity cases, where drips have time to develop fully, leading to transient 50-100K colder pulses being swept towards the mantle wedge corner in 2-D, and temporal and along-strike fluctuations in temperatures amounting to ~100-150K in 3-D. These temperature variations are sufficient to locally suppress melting, and in the 3-D cases to affect the stability of hydrous phases within the thermal boundary layer above the downgoing plate.

Preliminary results from 3-D models with a (1500 km) finite-width slab show that, for a dry mantle, the toroidal flow around the slab edges can affect wedge thermal structure to distances of 100-250 km from the edge and these temperature changes are sufficient to either enhance or shut down areas of melt production in the wedge corner, either because toroidal flow drags significant amounts of colder material from below a thick upper plate (in cases with strong trench retreat) or because at the convergence of the toroidal and wedge corner flow upper plate erosion is less efficient (in other cases). In cases with a locally hydrated wedge corner, substantial trench-parallel flow in the wedge can even extend to the slab centerline, lengthening SSC cell scales. Our 2-D models showed that steps or strong gradients in lithospheric strength or thickness provide nucleation points for instabilities. A difference in thickness between upper and side plates overlying a wetter mantle would also favour the formation of such edge instabilities, thereby further affecting temperatures and time dependence of the wedge structure. In contrast to previous models without side plates [Kincaid and Griffiths, 2004, 2003], we find that wedge temperatures right next to the corner are not significantly enhanced by trench retreat as the near-edge wedge corner is shielded by a cold tail of material dragged by toroidal flow for 50 to 150 km below the intersection between the upper plate and side plate.

Several observations indicate that the styles of wedge flow predicted by our models may play a role in Earth's subduction mantle wedges. Alternating high and low seismic velocity anomalies below the Honshu arc [Tamura et al., 2002] and time-dependent volcanic activity already lead Honda and coworkers [2008, 2010] to relate volcanic arc spacing to transient instabilities in their locally hydrated wedge corner models. Although the wavelength of arc Richter-rolls predicted in our 3-D models is larger than the common spacing between volcanic centres, smaller spacing could result from strong time-dependence of the position of high-temperature regions, as proposed by de Bremond d'Ars et al. [1995]. Variable, absent, or trench-parallel anisotropy has also been invoked as an argument for SSC [Behn et al., 2011] or complex flow [e.g., Pozgay et al., 2007, Smith et al., 2001, Di Leo et al., 2012, Hicks et al., 2012]. Although, variable slab geometry [Kneller and van Keken, 2007] and along-strike variations in slab properties (e.g., hydration) [Rychert et al., 2008] likely also contribute, as may variable buoyancy due to the subduction of sediments, local hydration, and the formation of melt [Gerya et al., 2006, Zhu et al., 2009, Behn et al., 2011], our models show that considerable complexity is expected even without such factors, if hydration is pervasive enough and lowers wedge viscosity. Additional evidence for low wedge viscosities over large distances, extending below the back arc, come from observations of back-arc geoid and bathymetry [Billen and Gurnis, 2001], high heat flow and thin back-arc lithosphere [Currie and Hyndman, 2006], and slow and attenuating seismic signatures of the mantle wedge [e.g. Wiens et al., 2008, Hwang et al., 2011]. Such conditions would favour the SSC flow styles obtained in models studied in this thesis.

Further insights could likely be gained by expanding our systematic studies. Cases with an infinitely wide subducting plate featured two distinct systems of SSC below old upper plates. We suggest testing whether the same behaviour could apply more evidently also to young upper plates, if the coupling depth between subducting and overriding plates was free to evolve and become shallower with increasing temperature [Arcay et al., 2005, 2007]. A dynamic (temperature- and hydration-controlled) coupling depth would strengthen corner erosion, resulting in lower wedge-corner viscosities, increased instability and a stronger influence on slab-surface temperatures. It would also be interesting to investigate the interaction between small-scale thermo-chemical plumes forming due to the presence of low-density sediments and melt-fluid mixtures [Gerya et al., 2006, Zhu et al., 2009, Behn et al., 2011] and the SSC mode of flow driven by lithospheric instability explored herein. We foresee easily-manageable improvements of our models which include the incorporation of realistic 3-D slab geometry [Kneller and van Keken, 2008], movement of the upper plate, different amounts and extents of mantle hydration (possibly governed by pressure, temperature and flow conditions) and slab steepening during trench retreat. In addition, a dynamic treatment of the slab would be something to further investigate [e.g., Arcay et al., 2005, 2008]. All these factors will likely complicate wedge flow and temperature fields and consequently further impact the distribution of melt and dehydration zones.

# Chapter 8

# Acknowledgements

While this accomplishment bears the signature of a Sardinian soul, it would not have been feasible without the support of many colleagues, friends and family. Above all, my Welsh Guide, and primary supervisor of this study, D. Rhodri Davies. I have a plethora (some "Italian poetry", as you would put it) of reasons to thank you, Rhodri. In primis, thank you for believing in the success of this research, from our first meeting to the final "click". Thank you in particular for the positivity you transmitted me during each and every of our $n^{th}$ meetings at godly and ungodly hours... for tirelessly pushing me to the limits and beyond. In this context, I have to subsequently undoubtedly thank Saskia Goes. Thank you, Saskia, for being an example of professionality and determination in reaching the goals and objectives which seemed so far beyond the horizon when you came into the project, but are now met as we reach the mountain's summit together. It is thanks to you both, Rhodri and Saskia, that my PhD has been as enriching as possible, both from the academic and human point of view. I will always be grateful to you and bring dear with me the memories of this research path undertaken together. I dearly thank other members of the enlarged "Team Geodynamics", Huw Davies for precious help at improving my models, particularly during our time at Berlin. Loic Fourel, *merci beaucoup* for your friendship and also logistical support, I look forward to meeting you at another conference soon, or elsewhere. Thanks also to Fanny Garel for her support while sharing her post-doc knowledge. I can not define how grateful I am to Stephan Kramer, who has been so kind and patient whenever I dropped by his office with questions of any kind. The same applies to Cian Wilson who has been extremely helpful at various times in the past years. In this context, I would like to greatly thank Gareth Collins and Jeroen van Hunen for agreeing examining this thesis, particularly as they fostered discussion on further improvements and future avenues of study for this work.

I would then like to move on to thank the whole of the Applied Modelling and Computation Group - AMCG - who have been supporting me throughout my four years at Imperial College. I therefore would like to first mention and thank my third supervisor Matthew Piggott for his mathematical input, especially during the first part of my PhD. Thanks to Tim Greaves, Surinder Singh Dio, and Zacharias Ioannis Zachariadis, for their vital and efficient technical support provided throughout the course of my PhD. A big thank you goes to Elinor Styles, Simon Funke, Hannah Hiester who have proof-read my transfer report, allowing me to get past. I also thank in this context the examiners Chris Pain and Mike Warner, for providing me very good feedback during the transfer exam. Patrick Farrell and Ben Martin helped me a good deal in the first months of PhD: thanks to them. At a Departmental level, I thank the Director of Postgraduate Studies Robert Zimmermann, for his support during the period of my transfer exam, and my very appreciated involvement in his classes at that stage. I am also grateful to Samantha Delamaine and all other Administrators who have smoothed bureaucracy for the continuation of my project throughout. In this context, I definitely am indebted to Simon Burbidge, who enabled my final project simulations to yield so interesting results by providing me with sufficient - and especially fast and efficient - access to the College's supercomputer facilities cx1 and cx2. Thanks also to the organisms funding most of this project, EPSRC and NERC, and HECToR's support staff.

Thank you to Simon Leo Mouradian and Nikolaos Mikhail (and enlarged families) for the help throughout, superb friendship and always present support, and of course unforgettable chess games. Thanks Sam Parkinson for some nice running together in the park, and together with Daniel Collins for your energy and proof-reading my paper prior to submission. *Efcharisto para poli* to Alexandros Avdis for giving me some access to his invaluable knowledge of mesh programming and various amusements at the coffee table. Thanks also to my great podmate Alistair McVicar for common unforgettable times shouting at the screen when the code hopelessly kept misbehaving. Thank you also to my 4th floor podmates Qinghua Lei and Liwei Guo, to Ting Zhang, Liping Cai and Dunhui Xiao for inputting some of their Chinese flavour during long neverending evenings at College. Thanks Jon Hill, for your support and helping me at any time. Thanks Alexandros Adam and Dave Robinson for your friendship, support and smiles. Thank you Frank Milthaler for everything, coming at my desk offering help at various times: you are the best and you know it. And you, Christian Jacobs: you (rock and) roll. Thanks to the "coffEEE" staff, Laura Niceforo and Barbara Perini in primis: let's face it, I would not have managed to get here without your coffees... but also and above all without your kindness and long-lasting presence and support. Thanks also to my great friends Sandro Valentini, Claire "Clairinha" Sena and Nuno "Nuninho" Miguel for their continued special support. Thank you Letizia Riccardi, Alessandra Mulas, Alessandro Collu, Erika Murgia, "Alahay", Jamie Lee Gunn, and all my friends from Italy, Sardinia, Bruxelles, Bloomington and elsewhere, who have been close to me and I am not mentioning here. Thanks to Francesca Galassi, Edgar and my other Clayponds friends for support and friendship at many times during this PhD. *Efcharisto paraparapara poli* podmates Nikos Karantzoulis and Elena Anastasaki, for your outstanding support, laughs, sharing emotions and life moments while helping me get through this at times painful, but rewarding experience. A big hug and huge thanks to you, and also to Vasilis Avgerinos, the "Florographics" and all others in the "Greek Team" who supported me in this period. Grazie Maria "Zogla" Aivazoglou for being awesome in your support, friendship, encouragement and precious advices. I could not cross the finish line without you.

Thank you George Dobre, tutor in my Undergraduate and Master at University of Kent, but especially a beautiful person to whom I will always owe my gratitude at a professional, as at a personal level. A Super Grazie to you, Immacolata Bortone "Tona" for your Napolitan flare and being such an amazing friend, always there for me. Thank you to Chiara Civiero for the support and chats over coffees and more: I will miss you and your "enlarged family". Merciiii Marina Micalo Aumedes, for always pushing the Velociraptor on. Grazieeee "Nikita" Maria Stefania Vecchio: our Fantasia will always take over the "nulla". Thanks Thanks Thanks Jake Jake Jake Solomon and Alexia Parsaye Ghomi, for your support in so many moments before and during my PhD, which helped me making it here. Thanks Davide Longoni and Joanna Stawikowska, for the long runs together both discovering London and taking out all the stress from our tough routine and work. Thank youuuuuu Maria "Momouli" Solomou and family, and Graziella Rossi, for sharing many moments, reloading my batteries in times of need with their energy. Grazie mille Edoardo Dalmonte, Giacomo Arata, Marco Barattini e Andrea Ferraro for life-long friendships worth a treasure. Thanks also to Gianluca Lauritano and his Napolitan para-para-paradise, Kana and Mantaro Tomita, Stefania Cossu and all other Callan friends who have been there for me at so many stages of my last years at Imperial College. I miss you and hug you all. Gracias y un abrazo muy fuerte para Damaris Elena Rey Alvarez, for being my inspiration both in work and life at so many stages of my last years of PhD.. I keep our many beautiful moments together in a special place in my heart. Thanks so much to my "sister" Monika Bartz, who has been there for me since early stages of this path, until the last day of this PhD. You have been always there and pushing me to make it and I can not thank you enough. Fratello Cumpariello Ivano Assenza... If I made it, I reached the goal, I crossed here the line of the longest marathon of my life yet, if I found the energies to reach the goal here, it is mostly thanks to the invaluable support and infinite energy with which you have always encouraged me. I can climb many more mountains like this one with a Brother like you. Finally, besides thanking all those who I forgot here and were close to me, the biggest Thanks of course goes to my family, indistinctly Nonna Iolinda Piliu e Zione Franco Bruno, Sorellotta Alessandra Le Voci, Papa’ Vincenzo Le Voci e Mamma Maria Bruno, e mio Nonno Giuseppe Le Voci assieme al mio Amico Marcin Makowski nelle verdi praterie lassu’... I dedicate this achievement especially to you, in this moment when, as put by the most famous of the Italian poets...

***"...il naufragar m’e’ dolce in questo mare."***

# List of Figures

# List of Tables

# Chapter 9

# Bibliography

G. A. Abers, P. E. van Keken, E. A. Kneller, A. Ferris, and J. C. Stachnik. The thermal structure of subduction zones constrained by seismic imaging: Implications for slab dehydration and wedge flow. *Earth Planet. Sci. Lett.*, 241:387–397, 2006. doi: 10.1016/j.epsl.2005.11.055.

D. J. Andrews and N. H. Sleep. Numerical modelling of tectonic flow behind island arcs. *Geophys. J. Int.*, 38(2):237–251, 1974. doi: 10.1111/j.1365-246X.1974.tb04118.x.

D. Arcay, M. P. Doin, and E. Tric. Numerical simulations of subduction zones: Effect of slab dehydration on the mantle wedge dynamics. *Phys. Earth Planet. Inter.*, 149:133–153, 2005. doi: 10.1016/j.pepi.2004.08.020.

D. Arcay, M. P. Doin, E. Tric, R. Bousquet, and C. de Capitani. Overriding plate thinning in subduction zones: Localized convection induced by slab dehydration. *Geochem. Geophys. Geosyst.*, 7(2):1–26, 2006. doi: 10.1029/2005GC001061.

D. Arcay, E. Tric, and M. P. Doin. Slab surface temperature in subduction zones: Influence of the interplate decoupling depth and upper plate thinning process. *Earth Planet. Sci. Lett.*, 255: 324–338, 2007. doi: 10.1016/j.epsl.2006.12.027.

D. Arcay, S. Lallemand, and M. P. Doin. Back-arc strain in subduction zones: Statistical observations versus numerical modeling. *Geochem. Geophys. Geosyst.*, 9, 2008. doi: 10.1029/2007GC001875.

S. Balay, W. D. Gropp, L. C. McInnes, and B. F. Smith. Efficient management of parallelism in object-oriented numerical software libraries. *Modern Software Tools for Scientific Computing*, pages 163–202, 1997.

E. Bali, A. Audetat, and H. Keppler. Water and hydrogen are immiscible in Earth's mantle. *Nature*, 495:220–222, 2013. doi: 10.1038/nature11908.

G. K. Batchelor. *An introduction to fluid dynamics*. Cambridge University Press, New York, 1967.

M. D. Behn, G. Hirth, and P. B. Kelemen. Trench-parallel anisotropy produced by foundering of arc lower crust. *Science*, 317(5834):108–111, 2007. doi: 10.1126/science.1141269.

M. D. Behn, P. B. Kelemen, G. Hirth, B. R. Hacker, and H.-J. Massonne. Diapirs as the source of the sediment signature in arc lavas. *Nature Geosci.*, 4:641–646, 2011.

N. Bellahsen, F. Funiciello, and C. Faccenna. Dynamics of subduction and plate motion in laboratory experiments: Insights into the âĂIJplate tectonicsâĂİ behavior of the Earth. *J. Geophys. Res.: Solid Earth*, 110(B1), 2005. doi: 10.1029/2004JB002999.

M. Benzi, G. H. Golub, and J. Liesen. Numerical solution of saddle point problems. *Acta Numer.*, 14:1–137, 2005.

M. I. Billen and M. Gurnis. A low viscosity wedge in subduction zones. *Earth Planet. Sci. Lett.*, 193(1 - 2):227–236, 2001. doi: 10.1016/S0012-821X(01)00482-4.

J. Buttles and P. Olson. A laboratory model of subduction zone anisotropy. *Earth Planet. Sci. Lett.*, 164:245–262, 1998.

A. M. Cagnioncle, E. M. Parmentier, and L. T. Elkins-Tanton. Effect of solid flow above a subducting slab on water distribution and melting at convergent plate boundaries. *J. Geophys. Res.*, 112(B9), 2007. doi: 10.1029/2007JB004934.

F. A. Capitanio and M. Faccenda. Complex mantle flow around heterogeneous subducting oceanic plates. *Earth Planet. Sci. Lett.*, 353-354:29–37, 2012. doi: 10.1016/j.epsl.2012.07.042.

F. A. Capitanio, G. Morra, and S. Goes. Dynamic models of downgoing plate-buoyancy driven subduction: Subduction motions and energy dissipation. *Earth Planet. Sci. Lett.*, 262:284–297, 2007. doi: 10.1016/j.epsl.2007.07.039.

S. Civello and L. Margheriti. Toroidal mantle flow around the Calabrian slab (Italy) from SKS splitting. *Geophys. Res. Lett.*, 31(L10601), 2004. doi: 10.1029/2004GL019607.

J. A. Conder. A case for hot slab surface temperatures in numerical viscous flow models of subduction zones with an improved fault zone parameterization. *Phys. Earth Planet. Inter.*, 149(1-2), 2005. doi: 10.1016/j.pepi.2004.08.018.

J. A. Conder and D. A. Wiens. Rapid mantle flow beneath the tonga volcanic arc. *Earth Planet. Sci. Lett.*, 264:299–307, 2007. doi: 10.16/j.epsl.2007.10.014.

J. A. Conder, D. W. Forsyth, and E. M. Parmentier. Asthenospheric flow and asymmetry of the east pacific rise, melt area. *J. Geophys. Res: Solid Earth*, 107(B12):ETG 8–1–ETG 8–13, 2002. doi: 10.1029/2001JB000807.

C. A. Currie and R. D. Hyndman. The thermal structure of subduction zone back arcs. *J. Geophys. Res.*, 111(B08404), 2006. doi: 10.1029/2005JB004024.

C. A. Currie, K. Wang, R. D. Hyndman, and J. He. The thermal effects of steady-state slab-driven mantle flow above a subducting plate: the cascadia subduction zone and backarc. *Earth Planet. Sci. Lett.*, 223(1-2):35–48, 2004. doi: 10.1016/j.epsl.2004.04.020.

C. A. Currie, R. S. Huismans, and C. Beaumont. Thinning of continental backarc lithosphere by flow-induced gravitational instability. *Earth Planet. Sci. Lett.*, 269:436–447, 2008. doi: 10.1016/j.epsl.2008.02.037.

A. Davaille and C. Jaupart. Onset of thermal convection in fluids with temperature-dependent viscosity: Application to the oceanic mantle. *J. Geophys. Res.*, 99:19853–19866, 1994. doi: 10.1029/94JB01405.

D. R. Davies, J. H. Davies, O. Hassan, K. Morgan, and P. Nithiarasu. Adaptive finite element methods in geodynamics - convection dominated mid-ocean ridge and subduction zone simulations. *Int. J. Numer. Method. H.*, 18(7-8):1015–1035, 2008. doi: 10.1108/09615530810899079.

D. R. Davies, C. R. Wilson, and S. C. Kramer. Fluidity: A fully unstructured anisotropic adaptive mesh computational modeling framework for geodynamics. *Geochem. Geophys. Geosyst.*, 12(6):Q06001, 2011. doi: 10.1029/2011GC003551.

G. F. Davies. *Dynamic Earth: Plates, Plumes and Mantle Convection*. 1999. ISBN 0-521-59933-4.

J. H. Davies and D. J. Stevenson. Physical model of source region of subduction zone volcanics. *J. Geophys. Res.*, 97(B2):2037–2070, 1992. doi: 10.1029/91JB02571.

J. de Bremond d'Ars, C. Jaupart, R. Sparks, and Stephen J. Distribution of volcanoes in active margins. *J. Geophys. Res.*, 100:20421–20432, 1995. doi: 10.1029/95JB02153.

J. F. Di Leo, J. Wookey, J. O. S. Hammond, J. M. Kendall, S. Kaneshima, H. Inoue, T. Yamashina, and P. Harjadi. Deformation and mantle flow beneath the Sangihe subduction zone from seismic anisotropy. *Phys. Earth Planet. Inter.*, 194-195:38–54, 2012.

C. Dumoulin, Doin. M. P. , D. Arcay, and L. Fleitout. Onset of small-scale instabilities at the base of the lithosphere: scaling laws and role of pre-existing lithospheric structures. *Geophys. J. Int.*, 160:344–356, 2005. doi: 10.1111/j.1365-246X.2004.02475.x.

H. Elman, D. Silvester, and A. Wathen. *Finite Elements and Fast Iterative Solvers with applications in incompressible fluid dynamics*. Numerical mathematics and scientific computation. Oxford Science Publications, 2005. ISBN 978-0-19-852868-5.

P. England and R. F. Katz. Melting above the anhydrous solidus controls the location of volcanic arcs. *Nature*, 467:700–704, 2010. doi: 10.1038/nature09417.

P. England and C. Wilkins. A simple analytical approximation to the temperature structure in subduction zones. *Geophys. J. Int.*, 159:1138–1154, 2004. doi: 10.1111/j.1365-246X.2004.02419.x.

P. England, R. Engdahl, and W. Thatcher. Systematic variation in the depths of slabs beneath arc volcanoes. *Geophys. J. Int.*, 156:377–408, 2004. doi: 10.1111/j.1365-246X.2003.02132.x.

M. Faccenda and F. A. Capitanio. Seismic anisotropy around subduction zones: Insights from three-dimensional modeling of upper mantle deformation and SKS splitting calculations. *Geochem. Geophys. Geosyst.*, 14, 2013. doi: 10.1029/2012GC004451.

D. Forsyth and S. Uyeda. On the relative importance of the driving forces of plate motion. *Geophys. J. Int.*, 43(1):163–200, 1975. doi: 10.1111/j.1365-246X.1975.tb00631.x.

F. Funiciello, C. Faccenna, D. Giardini, and K. Regenauer-Lieb. Dynamics of retreating slabs: 2. insights from three-dimensional laboratory experiments. *J. Geophys. Res.*, 108(B4), 2003. doi: 10.1029/2001JB000896.

Y. Furukawa and S. Uyeda. Thermal state under the Tohoko arc with consideration of crustal heat-generation. *Tectonophysics*, 164(2 - 4):175–187, 1989.

Z. Garfunkel, C. A. Anderson, and G. Schubert. Mantle circulation and the lateral migration of subducted slabs. *J. Geophys. Res.*, 91(B7):7205–7223, 1986. doi: 0148-0227/86/005B-5480.

T. V. Gerya and D. A. Yuen. Rayleigh-Taylor instabilities from hydration and melting propel 'cold plumes' at subduction zones. *Earth Planet. Sci. Lett.*, 212:47–62, 2003. doi: 10.1016/S0012-821X(03)00265-6.

T. V. Gerya, J. A. D. Connolly, D. A. Yuen, W. Gorczyk, and A. M. Capel. Seismic implications of mantle wedge plumes. *Phys. Earth Planet. Inter.*, 156:59–74, 2006. doi: 10.1016/j.pepi.2006.02.005.

W. Gorczyk, T. V. Gerya, J. A. D. Connolly, and D. A. Yuen. Growth and mixing dynamics of mantle wedge plumes. *Geology*, 35(7):587–590, 2007. doi: 10.1130/G23485A.1.

R. Govers and M. J. R. Wortel. Lithosphere tearing at STEP faults: response to edges of subduction zones. *Earth Planet. Sci. Lett.*, 236(1-2):505–523, 2005. doi: 10.1016/j.epsl.2005.03.022.

R. W. Griffiths, R. I. Hackney, and R. D. van der Hilst. A laboratory investigation of effects of trench migration on the descent of subducted slabs. *Earth Planet. Sci. Lett.*, 133(1-2):1–17, 1995. doi: 10.1016/0012-821X(95)00027-A.

T. L. Grove, C. B. Till, E. Lev, N. Chatterjee, and E. Medard. Kinematic variables and water transport control the formation and location of arc volcanoes. *Nature*, 459:694–697, 2009. doi: 10.1038/nature08044.

T. L. Grove, C. B. Till, and M. J. Krawczynski. The role of H20 in subduction zone magmatism. *Annu. Rev. Earth Planet. Sci.*, 40:413–439, 2012. doi: 10.1146/annurev-earth-042711-105310.

Z. Gvirtzman and A. Nur. The formation of Mount Etna as the consequence of slab rollback. *Nature*, 401:782–785, 1999. doi: 10.1038/44555.

B. R. Hacker. $H_2o$ subduction beyond arcs. *Geochem. Geophys. Geosys.*, 9:Q03001, 2008. doi: 10.1029/2007GC001707.

B. R. Hacker and G. A. Abers. Subduction factory 3: An excel worksheet and macro for calculating the densities, seismic wave speeds, and H2O contents of minerals and rocks at pressure and temperature. *Geochem. Geophys. Geosyst.*, 5:Q01005, 2004. doi: 10.1029/2003GC000614.

C. E. Hall, K. M. Fischer, E. M. Parmentier, and D. K. Blackman. The influence of plate motions on three-dimensional back arc mantle flow and shear wave splitting. *Geochem. Geophys. Geosyst.*, 105:28009–28033, 2000.

N. J. Hardebol, R. N. Pysklywec, and R. Stephenson. Small-scale convection at a continental back-arc to craton transition: application to the southern Canadian Cordillera. *J. Geophys. Res.*, 117:B01408, 2012. doi: 10.1029/2011JB008431.

N. Harmon and D. K. Blackman. Effects of plate boundary geometry and kinematics on mantle melting beneath the back-arc spreading centers along the Lau Basin. *Earth Planet. Sci. Lett.*, 298:334–346, 2010. doi: 10.1016/j.epsl.2010.08.004.

J. Hasenclever, J. P. Morgan, M. Hort, and L. H. Rüpke. 2D and 3D numerical models on compositionally buoyant diapirs in the mantle wedge. *Earth Planet. Sci. Lett.*, 311:53–68, 2011. doi: 10.1016/j.epsl.2011.08.043.

C. J. Hawkesworth, B. Dhuime, A. B. Pietranik, P. A. Cawood, A. I. S. Kemp, and C. D. Storey. The generation and evolution of the continental crust. *J. Geol. Soc.*, 167:229–248, 2010. doi: 10.1144/0016-76492009-072.

L. B. Hebert and M. Gurnis. Geophysical implications of Izu-Bonin mantle wedge hydration from chemical geodynamic modelling. *Isl. Arc*, 19:134–150, 2010.

L. B. Hebert, P. Antoshechkina, P. Asimow, and M. Gurnis. Emergence of a low-viscosity channel in subduction zones through the coupling of mantle flow and thermodynamics. *Earth Planet. Sci. Lett.*, 278(3):243–256, 2009. doi: 10.1016/j.epsl.2008.12.013.

S. P. Hicks, S. E. J. Nippress, and A. Rietbrock. Sub-slab mantle anisotropy beneath south-central Chile. *Earth Planet. Sci. Lett.*, 357-358:203 – 213, 2012.

G. Hirth and D. Kohlstedt. Rheology of the upper mantle and mantle wedge: A view from the experimentalists. *Geophysical Monograph American Geophysical Union*, 138, 2003. doi: 10.1029/138GM06.

G. Hirth and D. L. Kohlstedt. Water in the oceanic upper mantle: Implications for rheology, melt extraction and the evolution of the lithosphere. *Earth Planet. Sci. Lett.*, 144(1-2):93–108, 1996. doi: 10.1016/OO12-821X(96)00154-9.

S. Honda. A simple semi-dynamic model of the subduction zone: Effects of a moving plate boundary on the small-scale convection under the island arc. *Geophys. J. Int.*, 173:1095–1105, 2008. doi: 10.1111/j.1365-246X.2008.03766.x.

S. Honda and M. Saito. Small-scale convection under the back-arc occurring in the low viscosity wedge. *Earth Planet. Sci. Lett.*, 216:703–715, 2003. doi: 10.1016/S0012-821X(03)00537-5.

S. Honda and T. Yoshida. Application of the model of small-scale convection under the island arc to the NE Honshu subduction zone. *Geochem. Geophys. Geosyst.*, 6:Q01002, 2005. doi: 10.1029/2004GC000785.

S. Honda, T. Gerya, and G. Zhu. A simple three-dimensional model of thermo–chemical convection in the mantle wedge. *Earth Planet. Sci. Lett.*, 290:311–318, 2010. doi: 10.1016/j.epsl.2009.12.027.

J. Huang, S. Zhong, and J. van Hunen. Controls on sublithospheric small-scale convection. *J. Geophys. Res.*, 108(2405 - 2417), 2003. doi: 10.1029/2003JB002456.

Y. K. Hwang, J. Ritsema, and S. Goes. Global variation of body-wave attenuation in the upper mantle from teleseismic P wave and S wave spectra. *Geophys. Res. Lett.*, 38:L08311, 2011. doi: 10.1029/2011GL046812.

M. A. Jadamec and M. I. Billen. Reconciling surface plate motions with rapid three-dimensional mantle flow around a slab edge. *Nature*, 465:338–341, 2010. doi: 10.1038/nature09053.

H. Jung and S. Karato. Water-induced fabric transitions in olivine. *Science*, 293:1460–1463, 2001. doi: 10.1126/science.1062235.

S. Karato. Mapping water content in the upper mantle. *AGU Geophys. Monogr. Ser.*, 138:135–152, 2003. doi: 10.1029/138GM08.

S. Karato and P. Wu. Rheology of the upper mantle: A synthesis. *Science*, 260, 1993.

R. F. Katz, M. Spiegelman, and C. H. Langmuir. A new parameterization of hydrous mantle melting. *Geochem. Geophys. Geosyst.*, 4(9):1073, 2003. doi: 10.1029/2002GC000433.

P. B. Kelemen, J. L. Rilling, E. M. Parmentier, L. Mehl, and B. R. Hacker. Thermal structure due to solid-state flow in the mantle wedge beneath arcs. *Geophysical Monograph American Geophysical Union*, 138:293–311, 2003. doi: 10.1029/138GM13.

C. Kincaid and R. Griffiths. Laboratory models of the thermal evolution of the mantle during rollback subduction. *Nature*, 425:58–62, 2003.

C. Kincaid and R. W. Griffiths. Variability in flow and temperatures within mantle subduction zones. *Geochem. Geophys. Geosyst.*, 5(6):1–20, 2004. doi: 10.1029/2003GC000666.

C. Kincaid and I. S. Sacks. Thermal and dynamical evolution of the upper mantle in subduction zones. *J. Geophys. Res.*, 102:12295–12315, 1997.

S. D. King and D. L. Anderson. Edge-driven convection. *Earth Planet. Sci. Lett.*, 160:289–296, 1998.

E. A. Kneller and P. E. van Keken. Trench-parallel flow and seismic anisotropy in the Mariana and Andean subduction systems. *Nature*, 450:1222–1225, 2007. doi: 10.1038/nature06429.

E. A. Kneller and P. E. van Keken. Effect of three-dimensional slab geometry on deformation in the mantle wedge: Implications for shear wave anisotropy. *Geochem. Geophys. Geosyst.*, 9(1), 2008. doi: 10.1029/2007GC001677.

E. A. Kneller, P. E. van Keken, S. Karato, and J. Park. B-type olivine fabric in the mantle wedge: Insights from high-resolution non-Newtonian subduction zone models. *Earth Planet. Sci. Lett.*, 237:781–797, 2005. doi: 10.1016/j.epsl.2005.06.049.

E. A. Kneller, P. E. van Keken, I. Katayama, and S. Karato. Stress, strain, and b-type olivine fabric in the fore-arc mantle: Sensitivity tests using high-resolution steady-state subduction zone models. *J. Geophys. Res.*, 112:1–17, 2007. doi: 10.1029/2006JB004544.

T. Korenaga and J. Korenaga. Subsidence of normal oceanic lithosphere, apparent thermal expansivity, and seafloor flattening. *Earth Planet. Sci. Lett.*, 268:41–51, 2008. doi: 10.1016/j.epsl.2007.12.022.

S. C. Kramer, C. J. Cotter, and C. C. Pain. Solving the poisson equation on small aspect ratio domains using unstructured meshes. *Ocean Modell.*, 35:253–263, 2010.

S. C. Kramer, C. R. Wilson, and D. R. Davies. An implicit free surface algorithm for geodynamical simulations. *Phys. Earth Planet. Inter.*, 194-195:25–37, 2012. doi: 10.1016/j.pepi.2012.01.001.

S. Lallemand, A. Heuret, and D. Boutelier. On the relationships between slab dip, back-arc stress, upper plate absolute motion, and crustal nature in subduction zones. *Geochem. Geophys. Geosyst.*, 6(9), 2005. doi: 10.1029/2005GC000917.

C. Lee and S. D. King. Effect of mantle compressibility on the thermal and flow structures of the subduction zones. *Geochem. Geophys. Geosyst.*, 10:Q01006, 2009. doi: 10.1029/2008GC002151.

M. D. Long and T. W. Becker. Mantle dynamics and seismic anisotropy. *Earth Planet. Sci. Lett.*, 297:341–354, 2010. doi: 10.1016/j.epsl.2010.06.036.

V. Manea and M. Gurnis. Subduction zone evolution and low viscosity wedges and channels. *Earth Planet. Sci. Lett.*, 264:22–45, 2007. doi: 10.1016/j.epsl.2007.08.030.

M. Manga, M.J. Hornbach, A. LeFriant, et al. Heat flow in the Lesser Antilles island arc and adjacent back-arc Grenada basin. *Geochem. Geophys. Geosys.*, 13:Q08007, 2012. doi: 10.1029/2012GC004260.

C. E. Manning. The chemistry of subduction-zone fluids. *Earth Planet. Sci. Lett.*, 223:1–16, 2004. doi: 10.1016/j.epsl.2004.04.030.

D. A. May and L. Moresi. Preconditioned iterative methods for stokes flow problems arising in computational geodynamics. *Phys. Earth Planet. Inter.*, 171:33–47, 2008. doi: 10.1016/j.pepi.2008.07.036.

M. T. McCulloch and V. C. Bennett. Progressive growth of the Earth's continental crust and depleted mantle: geochemical constraints. *Geochim. Cosmochim. Ac.*, 58:4717–4738, 1994. doi: 10.1016/0016-7037(94)90203-8.

D. McKenzie, J. M. Roberts, and N. O. Weiss. Convection in the earth's mantle: towards a numerical simulation. *J. Fluid Mech.*, 62(3):465–538, 1974.

L. Mehl, B. R. Hacker, G. Hirth, and P. B. Kelemen. Arc-parallel flow within the mantle wedge: Evidence from the accreted Talkeetna arc, South Central Alaska. *J. Geophys. Res.*, 108(B8):2375–2392, 2003. doi: 10.1029/2002JB002233.

G. Morra, K. Regenauer-Lieb, and Giardini D. Curvature of oceanic arcs. *Geology*, 34:877–880, 2006. doi: 10.1130/G22462.1.

S. M. Peacock. Fluid processes in subduction zones. *Science*, 248(4953):329–337, 1990a. doi: 10.1126/science.248.4953.329.

S. M. Peacock. Numerical simulation of metamorphic pressure-temperature paths and fluid production in subducting slabs. *Tect.*, 9(5):1197–1211, 1990b. doi: 10.1029/TC009i005p01197.

S. M. Peacock. Thermal and petrologic structure of subduction zones. *AGU Monographs: Subduction Top to Bottom*, 96:119–133, 1996. doi: 10.1029/GM096p0119.

S. M. Peacock and K. Wang. Seismic consequences of warm versus cool subduction metamorphism: Examples from Southwest and Northeast Japan. *Science*, 286:937–939, 1999. doi: 10.1126/science.286.5441.937.

J. A. Pearce, P. T. Leat, P. F. Barker, and I. L. Millar. Geochemical tracing of Pacific-to-Atlantic upper-mantle flow through the Drake Passage. *Nature*, 410:457–461, 2001. doi: 10.1038/35068542.

M. D. Piggott, G. J. Gorman, C. C. Pain, P. A. Allison, A. S. Candy, B. T. Martin, and M. R. Wells. A new computational framework for multi-scale ocean modelling based on adapting unstructured meshes. *Int. J. Numer. Meth. Fl.*, 56:1003–1015, 2008. doi: 10.1002/fld.1663.

C. Piromallo, T. W. Becker, F. Funiciello, and C. Faccenna. Three-dimensional instantaneous mantle flow induced by subduction. *Geophys. Res. Lett.*, 33(L08304), 2006. doi: 10.1029/2005GL025390.

T. Plank, L. B. Cooper, and C. E. Manning. Emerging geothermometers for estimating slab surface temperatures. *Nature Geosci.*, 2:611–615, 2009. doi: 10.1038/ngeo614.

S. Poli and M. W. Schmidt. Petrology of subducted slabs. *Annu. Rev. Earth Planet. Sci.*, 30:207–235, 2002. doi: 10.1146/annurev.earth.30.091201.140550.

S. H. Pozgay, D. A. Wiens, J. A. Conder, H. Shiobara, and H. Sugioka. Complex mantle flow in the mariana subduction system: evidence from shear wave splitting. *Geophys. J. Int.*, 170(1):371–386, 2007. doi: 10.1111/j.1365-246X.2007.03433.x.

F. M. Richter. Convection and the large-scale circulation of the mantle. *J. Geophys. Res.*, 78(35):8735–8745, 1973. doi: 10.1029/JB078i035p08735.

C. Rychert, Fischer K. M., G. A. Abers, T. Plank, E. M. Syracuse, J. M. Protti, V. Gonzalez, and W. Strauch. Strong along-arc variation in attenuation in the mantle wedge beneath Costa Rica and Nicaragua. *Geochem. Geophys. Geosyst.*, 9(10), 2008. doi: 10.1029/2008GC002040.

Y. Saad. A flexible inner-outer preconditioned gmres algorithm. *SIAM J. Sci. Comput.*, 14(2):461–469, 1993.

W. P. Schellart. Kinematics of subduction and subduction-induced flow in the upper mantle. *J. Geophys. Res.*, 109(B07401), 2004. doi: 10.1029/2004JB002970.

W. P. Schellart, J. Freeman, D. R. Stegman, L. Moresi, and D. May. Evolution and diversity of subduction zones controlled by slab width. *Nature*, 446:308–311, 2007. doi: 10.1038/nature05615.

M. W. Schmidt and S. Poli. Experimentally based water budgets for dehydrating slabs and consequences for arc magma generation. *Earth Planet. Sci. Lett.*, 163:361–379, 1998.

B. Schurr, G. Asch, A. Rietbrock, R. Trumbull, and C. Haberland. Complex patterns of fluid and melt transport in the central Andean subduction zone revealed by attenuation tomography. *Earth Planet. Sci. Lett.*, 215:105–119, 2003.

M. Sdrolias and R. D. Müller. Controls on back-arc basin formation. *Geochem. Geophys. Geosyst.*, 7(4):1–40, 2006. doi: 10.1029/2005GC001090.

M. Seton, R. D. Muller, S. Zahirovic, C. Gaina, T. H. Torsvik, G. Shephard, A. Talsma, M. Gurnis, M. Turner, S. Maus, and M. Chandler. Global continental and ocean basin reconstructions since 200 Ma. *Earth-Sci. Rev.*, 113:212–270, 2012. doi: 10.1016/j.earscirev.2012.03.002.

G. P. Smith, D. A. Wiens, K. M. Fischer, L. M. Dorman, S. C. Webb, and J. A. Hildebrand. A complex pattern of mantle flow in the Lau back-arc. *Science*, 292(5517):713–716, 2001. doi: 10.1126/science.1058763.

D. R. Stegman, J. Freeman, W. P. Schellart, L. Moresi, and D. May. Influence of trench width on subduction hinge retreat rates in 3-D models of slab rollback. *Geochem. Geophys. Geosyst.*, 7 (3), 2006. doi: 10.1029/2005GC001056.

E. M. Syracuse and G. A. Abers. Global compilation of variations in slab depth beneath arc volcanoes and implications. *Geochem. Geophys. Geosyst.*, 7(5):73–90, 2006. doi: 10.1029/2005GC001045.

E. M. Syracuse, P. E. van Keken, and G. A. Abers. The global range of subduction zone thermal models. *Phys. Earth Planet. Inter.*, 183:73–90, 2010. doi: 10.1016/j.pepi.2010.02.004.

Y. Tamura, Y. Tatsumi, D. Zhao, Y. Kido, and H. Shukuno. Hot fingers in the mantle wedge: new insights into magma genesis in subduction zones. *Earth Planet. Sci. Lett.*, 197:105–116, 2002.

Y. Tatsumi. Migration of fluid phases and genesis of basalt magmas in subduction zones. *J. Geophys. Res.*, 94:4687–4707, 1989. doi: 10.1029/JB094iB04p04697.

T. Trua, G. Serri, and M. P. Marani. Lateral flow of African mantle below the nearby Tyrrhenian plate: geochemical evidence. *Terra Nova*, 15(6):433–440, 2003. doi: 10.1046/j.1365-3121.2003.00509.x.

J. van Hunen, A. P. van den Berg, and N. J. Vlaar. On the role of subducting oceanic plateaus in the development of shallow flat subduction. *Tectonophysics*, 352(3-4):317–333, 2002. doi: 10.1016/S0040-1951(02)00263-9.

J. van Hunen, J. Huang, and S. Zhong. The effect of shearing on the onset and vigor of small-scale convection in a Newtonian rheology. *Geophys. Res. Lett.*, 30(19):1991, 2003. doi: 10.1029/2003GL018101.

P. E. van Keken. The structure and dynamics of the mantle wedge. *Earth Planet. Sci. Lett.*, 215: 323–338, 2003. doi: 10.1016/S0012-821X(03)00460-6.

P. E. van Keken, B. Kiefer, and S. M. Peacock. High-resolution models of subduction zones: Implications for mineral dehydration reactions and the transport of water into the deep mantle. *Geochem. Geophys. Geosyst.*, 3(10):1056, 2002. doi: 10.1029/2001GC000256.

P. E. van Keken, C. Currie, S. D. King, M. D. Behn, A. Cagnioncle, J. He, R. F. Katz, S. C. Lin, E. M. Parmentier, M. Spiegelman, and K. Wang. A community benchmark for subduction zone modeling. *Phys. Earth Planet. Inter.*, 171(1-4):187–197, 2008. doi: 10.1016/j.pepi.2008.04.015.

P. E. van Keken, B. R. Hacker, E. M. Syracuse, and G. A. Abers. Subduction factory 4: Depth-dependent flux of H2O from slabs worldwide. *J. Geophys. Res.*, 116, 2011. doi: 10.1029/2010JB007922.

P. Vanek, J. Mandel, and M. Brezina. Algebraic multigrid by smoothed aggregation for second and fourth order elliptic problems. *Computing*, 56(3):179–196, 1996. doi: 10.1007/BF02238511.

R. Verfurth. A combined conjugate gradient-multigrid algorithm for the numerical solution of the stokes problem. *IMA J. Numer. Anal.*, 4(4):441–455, 1984. doi: 10.1093/imanum/4.4.441.

I. Wada and K. Wang. Common depth of slab-mantle decoupling: Reconciling diversity and uniformity of subduction zones. *Geochem. Geophys. Geosyst.*, 10:Q10009, 2009. doi: 10.1029/2009GC002570.

J. I. Wendt, M. Regelous, K. D. Collerson, and A. Ewart. Evidence for a contribution from two mantle plumes to the island-arc lavas from northern Tonga. *Geology*, 25(7):611–614, 1997. doi: 10.1130/0091-7613(1997)âĂŃ025.

D. A. Wiens, J. A. Conder, and U.H. Faul. The seismic structure and dynamics of the mantle wedge. *Annu. Rev. Earth Planet. Sci.*, 36:421–455, 2008.

C. R. Wilson. Modelling multiple-material flows on adaptive unstructured meshes. *PhD thesis, AMCG group, Department of Earth Sciences and Engineering, Imperial College London*, 2009.

C. R. Wilson, M. Spiegelman, and P. E. van Keken. On the physics of fluid flow in subduction zones. *Earth Planet. Sci. Lett.*, pages In Press,, 2013.

E. A. Wirth and J. Korenaga. Small-scale convection in the subduction zone mantle wedge. *Earth Planet. Sci. Lett.*, 357-358:111–118, 2012. doi: 10.1029/2012JB009524.

G. M. Yogodzinski, J. M. Lees, T. G. Churikova, F. Dorendorf, G. WÃűerner, and O. N. Volynets. Geochemical evidence for the melting of subducting oceanic lithosphere at plate edges. *Nature*, 409:500–504, 2001. doi: 10.1038/35054039.

G. Zhu, T. V. Gerya, D. A. Yuen, S. Honda, T. Yoshida, and J. A. D. Connolly. Three-dimensional dynamics of hydrous thermal-chemical plumes in oceanic subduction zones. *Geochem. Geophys. Geosyst.*, 10(11):1–20, 2009. doi: 10.1029/2009GC002625.

G. Zhu, T. V. Gerya, S. Honda, P. J. Tackley, and D. A. Yuen. Influences of the buoyancy of partially molten rock on 3-D plume patterns and melt productivity above retreating slabs. *Phys. Earth Planet. Inter.*, 185:112–121, 2011. doi: 10.1016/j.pepi.2011.02.005.